High resolution microwave and infrared spectroscopy of four-membered heterocyclic compounds

by

Ziqiu Chen

A Thesis submitted to the Faculty of Graduate Studies of the University of Manitoba in partial fulfillment of the requirements of the degree of

Doctor of Philosophy

Department of Chemistry

University of Manitoba

Winnipeg, Canada

Abstract

High resolution molecular spectroscopic techniques are useful tools to accurately probe energy differences between quantum states of molecules. These energy levels are inherently dependent on the underlying potential functions, which ultimately govern the structures and dynamics of molecules. Thus, the detailed characterization of potential energy profiles through molecular spectroscopy provides important information about molecular properties. Given the increased structural and dynamic complexity of large molecules, small compounds serve as excellent prototypes to establish quantum mechanical models that accurately characterize quantum states and ultimately potential energy functions of various molecular classes. This thesis describes the use of rotational and rovibrational spectroscopy to probe one such class: four-membered heterocycles.

Rotationally-resolved vibrational spectra of four-membered rings including β-propiolactone (c-$C_3H_4O_2$), 3-oxetanone (c-$C_3H_4O_2$), azetidine (c-C_3H_6N) and silacyclobutane (c-C_3H_8Si) were recorded below 1200 cm^{-1} using a Fourier transform infrared spectrometer (FTIR) with synchrotron light at the far infrared beamline of the Canadian Light Source (CLS). Additionally, Fourier transform microwave (FTMW) spectroscopy was used to study the pure rotational spectra of β-propiolactone and silacyclobutane for the first time. This allowed the accurate characterization of the ground vibrational state and molecular structure in support of the rovibrational analysis.

The far infrared vibrational modes of these four molecules were analyzed individually initially and followed by a global fit of all observed transitions of each molecule. Unique spectroscopic signatures arising from Coriolis coupling

(β-propiolactone, 3-oxetanone), tunneling motions (azetidine, silacyclobutane) and the large amplitude ring puckering vibration (3-oxetanone, azetidine, silacyclobutane) were revealed and treated. The resultant Hamiltonian models used for each molecule account for the observed spectra as the spectroscopic constants are consistent across the ground state and all vibrationally excited states studied. Collectively, these studies have provided a highly effective working protocol for the treatment of high resolution rovibrational data to model the dynamic behaviour of real molecules.

Acknowledgements

The present and past members of the van Wijngaarden group, especially two postdoctoral researchers: Dr. Galen Sedo and Dr. Ming Sun who were very helpful during the initial stage of my time in the group.

My parents, Zhuohua and Tingsi Chen, thank you for the support and understanding when it was needed and the sacrifices you have made to provide me the opportunities of education along the way.

All colleagues and fellow graduate students in the Chemistry Department for your support.

Table of Contents

List of Figures

List of Tables

Chapter 1

Introduction

The dynamic behavior of molecules that allows for conformational changes has been the subject of studies for many decades because of the important role such motions play in chemical reactions. This is particularly true in the case of large molecules (including polymers and biomolecules) because they have more degrees of freedom and are usually quite flexible. In an effort to characterize the physical and chemical properties (reactivity, inter- and intramolecular interactions, etc.) of individual molecules, both chemists and biochemists are interested in conformational analysis to gain vital information pertaining to the properties of conformers such as structures and energies. It is found that conformational changes in molecules often follow low energy vibrational pathways, which are governed by potential energy surfaces.[1, 2] This makes spectroscopy a powerful experimental tool to unravel complex molecular dynamics.

Vibrational spectroscopic techniques, for example, including infrared and Raman spectroscopy have been extensively used in probing protein structures.[3, 4] However, as the size of a molecule increases, its vibrational spectra become more complicated, causing difficulties for interpretation. On the other hand, the vibrational spectra of simpler systems, such as small rings, provide precise information about the potential energy surface. The methods developed during their analyses can be applied to understand the dynamics of larger molecules in the future.

It is possible for small molecules such as four-membered heterocycles to have two or more stable conformers (corresponding to minima on the potential energy surface) that

differ in energy. The observation of distinctive spectroscopic signatures as the energy levels of conformationally dependent vibrational modes (out-of-plane ring motions, ring inversions, etc.) are probed allows the nature of the surface to be examined. In this respect, four-membered rings have undergone numerous theoretical and experimental investigations as prototype systems owing to their relatively simple structures compared to complex biomolecules as reviewed by Legon[2] and Carreira *et al*.[5] The far infrared region of the spectrum is of particular importance as conformational changes in molecules are often related to low frequency, large amplitude vibrations that have little interaction with higher frequency bands.[6]

Another key reason that these rings have been interrogated for many years is due to inherent difficulties in modelling low frequency vibrations,[1, 2, 7, 8, 9] which often arise from anharmonic potential energy profiles. Thus, experimental results are needed to test the validity of models that describe the potential energy functions of far infrared modes. In order to do a complete vibrational characterization of a polyatomic molecule, multi-dimensional analysis is often required to account for geometric changes during vibrations in all coordinates. Even for "simple" four-membered heterocyclic molecules, this is not realistic currently. Therefore, vibrational modes that can be separated from other motions and represented in a one-dimensional mathematical expression would be ideal candidates to model at the start. In the past, spectroscopic investigations have demonstrated that unique vibrations in molecules including ring-puckering in cyclobutane,[10, 11] inversion in ammonia[12] and internal rotation in ethane[13, 14] can be characterized experimentally and treated in this fashion.

In an effort to establish a quantitative model of low frequency, large amplitude vibrations in small rings, Bell proposed that certain out-of-plane vibrations should have their potential energy functions in the form of a one-dimensional oscillator that involves a fourth-order term. [15] Later, pioneering spectroscopic work in the microwave and infrared regions carried out by Chan *et al*. on oxetane (a four-membered ring, C_3H_6O) revealed that the potential energy function for the ring puckering motion is indeed related to the ring-displacement coordinate through a power of four. The resulting function has a double-well shape with a shallow barrier to planarity of 35 cm^{-1}.[16,17,18,19] In their studies, distinctive spectral features arising from the existence of this small barrier offered direct evidence of the nature of the surface and eventually led to the determination of the equilibrium conformation of this molecule. This study provides an excellent example of understanding the connection between a unique spectroscopic signature and the underlying potential energy profile using experimental means and quantum mechanical models.

Out of several low frequency vibrations that involve the heavy atoms of the ring moiety, the ring puckering mode is one of the most characteristic large amplitude modes in four-membered heterocyclic molecules because it is the only out-of-plane vibration of the ring skeleton (as for an n-membered ring skeleton, there are n-3 out-of-plane modes[2]). Figure 1.1 depicts the ring puckering motion of a planar molecule 3-oxetanone as an example. This unique mode has a much lower frequency and is often separated from the remaining 3n-7 higher frequency modes. Thus, this motion is commonly characterized using a one-dimensional potential function and attracts special interest.[2] In contrast, the similar out-of-plane mode in five-membered rings appears in a way that the phase of the

puckering rotates around the ring (called pseudo-rotation) and its potential function typically requires approximation in two dimensions (n=5, two out-of-plane modes).[20, 21] Classically, the ring skeleton in four-membered heterocycles is highly strained and its planarity depends on a dynamic balance between two opposing features: 1) the steric hindrance of neighbouring CH_2 groups which is minimized by the torsional forces exerted along the bonds and favours a puckered ring; and 2) the ring strain, which is minimized in the planar structure.

From a practical point of view, the ring puckering vibration is spectrally separated from other modes and it can be described using a potential function in a relatively simple form of $V=ax^4+bx^2$ where x is the one-dimensional ring puckering coordinate, a is a positive constant and b is a constant that can be either positive or negative. Figure 1.2 illustrates the definition of the ring puckering angle θ in relation to the ring puckering coordinate x. The shape of this potential function, which is determined by the sign of the quadratic coefficient b, gives rise to molecular dependent spectroscopic features. The characterization of the potential energy function of the puckering vibration can thus provide direct information pertaining to the configuration of the ring backbone. Figure 1.3 shows the ring puckering potential functions for azetidine,[22] silacyclobutane[23] and oxetane,[19] which have completely different equilibrium structures despite the fact that the main difference among them is the heteroatom in the ring skeleton. Therefore, spectroscopic studies of four-membered rings provide the opportunity to deduce the influence of different functional groups on the potential energy profile and energy levels of the ring molecules.

Figure 1.1: A schematic to show the ring puckering motion in 3-oxetanone. (a) and (c) display the molecular structure at the maximum vibrational displacement value whereas (c) shows the equilibrium structure.
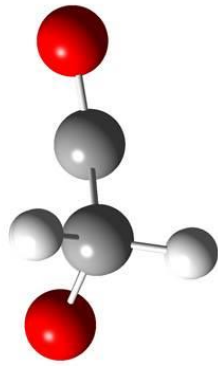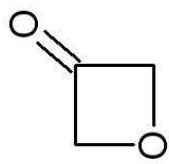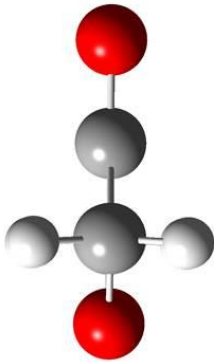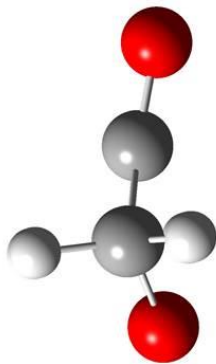
Figure 1.2: Definition of the ring puckering coordinate (x) and angle (θ) in four membered rings. Solid lines represent actual chemical bonds whereas dashed lines are auxiliary lines drawn to illustrate x and θ.
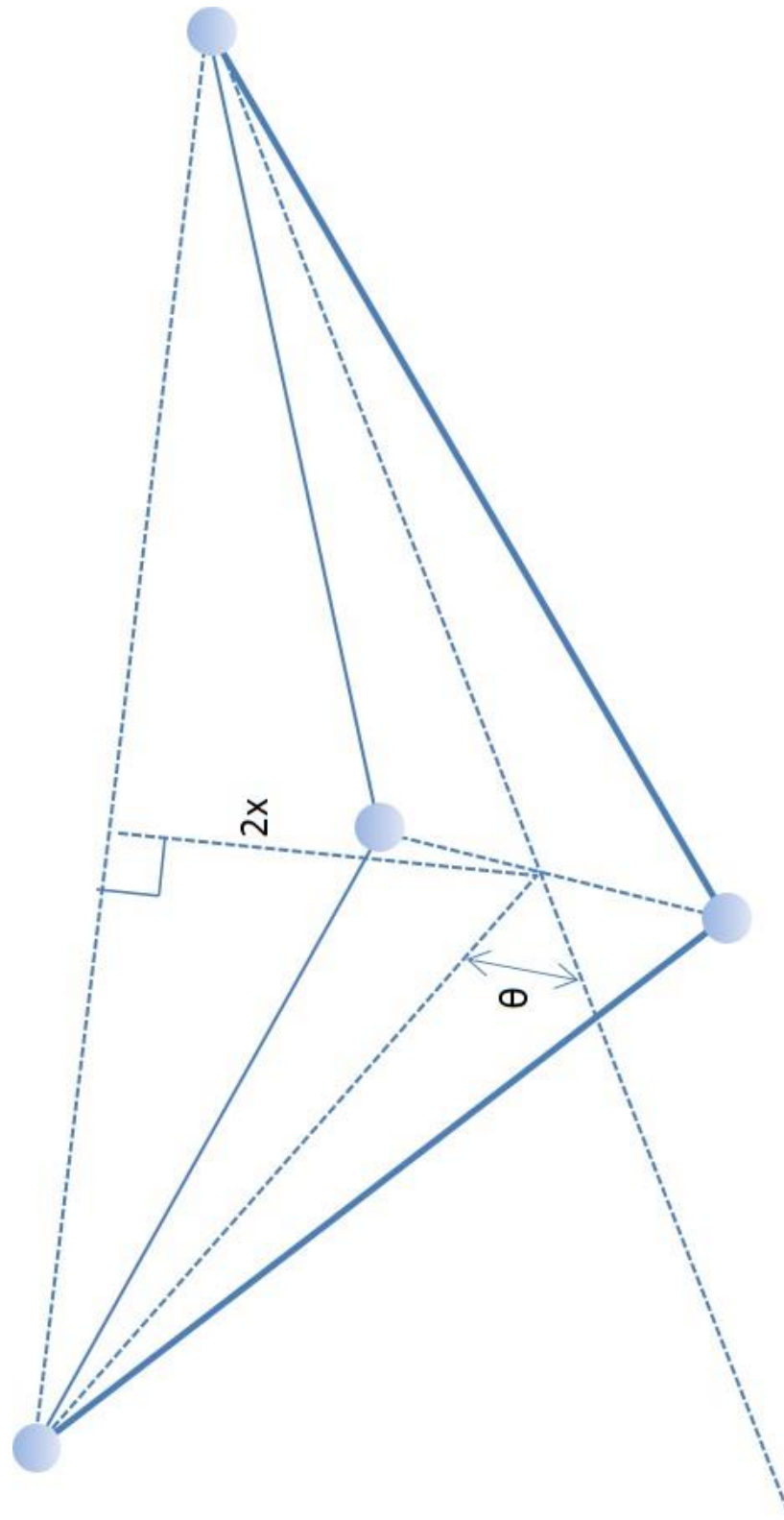
Figure 1.3: The ring puckering potential functions for azetidine (a, single-well asymmetric potential[22]), oxetane (b, double-well symmetric potential with a shallow barrier[19]) and silacyclobutane (c, double-well symmetric potential with a high barrier[23]). Note that the energy scales of the three potential functions are different. The arrows indicate the energy differences between different vibrational levels (v), which are given in cm^{-1}.
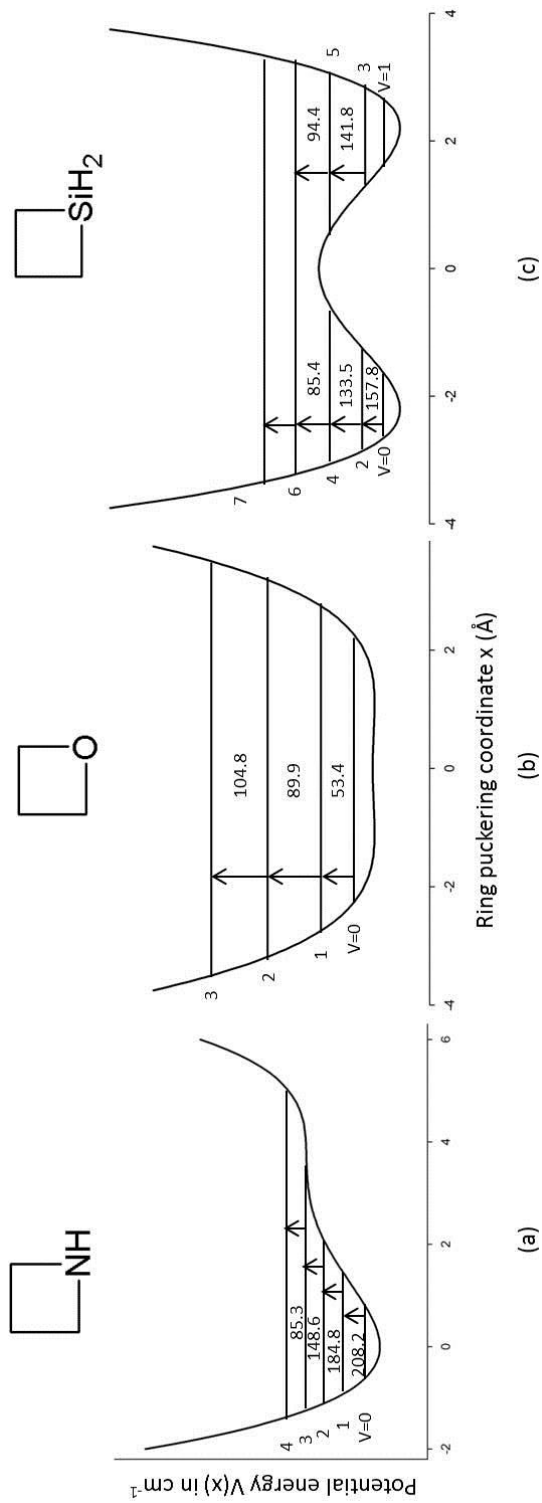
On a fundamental level, greater understanding of the potential energy profile may have chemical implications as it identifies alternate pathways to interconvert between different conformers or between two equivalent conformers (as shown in Figure 1.3 for oxetane and silacyclobutane) without having to overcome a classical barrier. This so-called *tunnelling effect* is a quantum mechanical phenomenon and can affect the rate of a reaction substantially.[24] Recent work on methylhydroxycarbene[25] and the reaction of OH + CO[26] shows the importance of tunnelling in kinetic control and reaction dynamics, respectively.

The characterization of potential energy surfaces is generally achieved via 1) computational methods (including semi-empirical, density functional theory and *ab initio* calculations); 2) experimental measurements using spectroscopy. Generally, the accuracy of standard calculations is limited as a result of the anharmonic nature of low frequency, large amplitude modes and this leaves spectroscopic means as one of the most powerful tools to obtain accurate information about the potential energy functions. Rotational and vibrational spectroscopies allow the determination of the spacing between rotational energy states (within the same vibrational state) and between different vibrational states, respectively. For instance, the potential energy functions shown in Figure 1.3 were constructed based on the measured vibrational spacing (indicated as arrows) by far infrared spectroscopy whereas information about rotational energy levels (too small to show on these scales) was obtained by microwave experiments. However, the resulting knowledge of the potential energy function was somewhat limited by the resolution of the experimental methods available in the 1950s through the 1980s. The vibrational band centers determined from far infrared measurements were based on their Q branch maxima

which were typically accurate to 0.1 cm^{-1} [2] while the low resolution (~100 kHz) of microwave measurements at the time prevented the study of key spectral features such as tunneling motions and nuclear quadrupole hyperfine structure which can require resolution of a few kHz to observe. Hence, the derived potential functions from earlier studies provided a "coarse" description of the energy which can be improved using modern experimental techniques with better resolution.

Historically, pure rotational molecular transitions were measured in static cells (waveguide) at room temperature until supersonic jet expansion was first introduced into cavity-based microwave experiments in 1979 by Balle and Flygare.[27,28,29] The most prominent advantage of this custom-built Fourier transform microwave (FTMW) spectroscopy technique is the high resolution (up to 7 kHz) it offers compared to that of older methods (~100 kHz) as a result of the jet. This benefit is manifested in studies of small molecules where distinctive features are separated on the order of a few kHz. For example, a microwave study of silacyclobutane conducted in the 1970s was not able to resolve the doubling in the ground state arising from ring inversion tunnelling.[30] The low rotational temperature (a few Kelvin) produced in molecular beams makes the observation of transitions with low quantum numbers possible which are crucial in mapping the potential energy profile as the determination of its shape depends on knowledge of the region around the minimum. For vibrational measurements, the resolution of Fourier transform infrared (FTIR) spectroscopy using conventional light sources was limited to ~0.04 cm^{-1} due to technical difficulties until the 1980s, [31] and this prevented the fine energy gaps between rotation-vibration levels from being accurately probed. The recent coupling of synchrotron radiation (which offers highly collimated and

bright light) to a FTIR spectrometer allows the combination of high resolution and high sensitivity in the infrared region for the first time,[32] and hence permits accurate mapping of the potential energy surfaces through probing a wide range of rovibrational energy levels. Although several dedicated far infrared beamlines at synchrotron facilities worldwide have been commissioned since 2007, there have been relatively few cases of rovibrational studies on small molecules to date as this technique is still a very new method.[33, 34, 35, 36, 37, 38, 39]

With such technical limits reduced by instrument advances, the next challenge lies in interpreting and analyzing complex spectral data to set benchmarks. Generally, the rotation-vibration spectra of even simple molecules are complicated by the sheer number of transitions observed at room temperature, the overlapping of adjacent vibrational modes and often, by minor perturbations that lead to departure from the well-known models such as the harmonic oscillator and rigid-rotor Hamiltonians. For instance, several regions of the infrared spectra of methane remain untouched due to spectral congestion and severe interactions between energy levels despite the fact that this molecule has been the subject of extensive investigation because of its importance in remote sensing. [40 , 41] Therefore, strategies to systematically assign the observed rovibrational transitions, apply quantum mechanical tools and derive the underlying potential energy functions are highly desired.

The general methodology for spectral assignment may be common for a range of molecules while distinctive spectral features encountered in the analysis are often molecule-specific. Therefore, studying molecules with structural similarities provides key experimental evidence that allows us to model these features correctly. For example,

Coriolis-type perturbations, which originate from interactions between rotation-vibration levels, are common in low frequency modes of small molecules. As a result of this interaction, affected transitions are typically shifted and have different intensities than predicted from the unperturbed model. This effect has been discussed theoretically in detail[42, 43, 44, 45] and its treatment is considered to be an important factor in establishing a general theory of the rotation-vibration Hamiltonian. [46, 47] The treatment of such perturbations has the following spectroscopic implications according to Mills:[48] 1) it allows the determination of interaction parameters which in turn provide precise, physically meaningful values to other constants such as rotational and centrifugal distortion constants; 2) it can often offer information about dark (inactive) states which are involved in the interaction and 3) it provides indication of the relative signs of transition moments through the observed intensities. However, the implementation of a generalized theory can be tricky when it comes to dealing with dense rotation-vibration spectra. This is one of main reasons that there are still many unassigned spectral regions for molecules like methane that have been under study for decades. The analysis of Coriolis perturbations will contribute to the establishment of accurate Hamiltonian models that account for molecular properties.

The work presented in this thesis has two main goals: 1) to characterize the lowest energy states and potential energy functions of the chosen four-membered heterocyclic molecules via combined high resolution microwave and infrared spectroscopic studies; 2) to develop strategies for the analysis of high resolution data, in particular rovibrational transitions (as this type of analysis is still new in the field) such that the protocols developed can be applied to other molecules in the longer term. The selected heterocyles

for this study are silacyclobutane (C_3H_8Si), azetidine (C_3H_7N), 3-oxetanone ($C_3H_4O_2$) and β-propiolactone ($C_3H_4O_2$) none of which has been the subject of prior rotationally resolved vibrational studies. The heavy atom ring skeletons of the first two molecules are nonplanar while the latter two have planar backbones. Silacyclobutane was among the first few four-membered rings that were spectroscopically investigated following the pioneering work on oxetane in the 1960s.[16, 17, 18, 19] As the silicon version of oxetane, silacyclobutane has a double-well ring puckering potential function with a high barrier of 440 cm^{-1} between the two equivalent minima[23] which should give rise to tunnelling splittings in the first three vibrational states. Due to the limited resolution at the time of the earlier studies, no direct observation of tunnelling was made.[30] Therefore, a high resolution examination of silacyclobutane is expected to exhibit new spectral features that will reveal details of the tunnelling dynamics of this molecule. In contrast, azetidine is estimated to have a very high barrier to ring inversion of 1900-2600 cm^{-1} and a possible –NH inversion tunnelling motion and the form of its ring puckering potential has been debated between single-well and double-well shapes.[49, 50, 51, 52] Measurements of energy levels between rotation-vibration states can shed light on both motions. Unlike the former two molecules, 3-oxetanone and β-propiolactone, which are structural isomers, have planar ring backbones with symmetries of C_{2v} and C_s, respectively. The coupling of the carbonyl in-plane and out-of-plane ring deformation modes should provide an opportunity to study Coriolis interactions in molecules of different symmetry as they are close in energy.

The remainder of this thesis is divided into seven chapters. Chapter 2 and Chapter 3 give descriptions of the two experimental techniques used in this study, namely Fourier

transform microwave (FTMW) spectroscopy and Fourier transform infrared (FTIR) spectroscopy. Technical details as well as general experimental schemes are detailed in these chapters. Chapter 4 describes the spectroscopic study of β-propiolactone via pure rotational measurements using both FTMW and rovibrational FTIR experiments. Out of the five low frequency vibrational bands analyzed, the ν_{13} and ν_{20} bands were found to interact through an a-type Coriolis coupling mechanism. This highlights the importance of analyzing low frequency bands as a group as vibrational modes often interact. In Chapter 5, the rovibrational analysis of 3-oxetanone shows a similar Coriolis perturbation between the ν_{16} and ν_{20} modes. Following the assignment of the dense ring puckering mode (ν_{21}) of 3-oxetanone, the accurately determined band centers of the fundamental and first three excited states of this mode allowed the determination of its ring puckering potential energy function, which turned out to be more anharmonic than previously thought. Chapter 6 is devoted to the analysis of the lowest three vibrational bands of azetidine. For the ν_{14} and ν_{15} modes, c-type rotation-vibration transitions were found in addition to the a-type rotation-vibration-inversion ones, indicating the presence of the coupling of these vibrations with –NH inversion in this molecule. In Chapter 7, ring inversion tunnelling in the ground vibrational state of silacyclobutane is reported for the first time and the analysis of resultant complex rovibrational spectra are detailed as well. The ground state of silacyclobutane (SCB) was found to be split into two levels from pure rotational measurements as a result of tunnelling between two minima on the symmetric double-well ring puckering potential function. The resultant rotational constants determined from the microwave study of the ^{12}C, ^{13}C, ^{28}Si, ^{29}Si and ^{30}Si isotopologues allowed accurate structural determination of SCB in the ground vibrational

13

state. Tunnelling doubling was also observed in the rotational structure of the ν_{29} SiH_2 rocking and ν_{30} ring puckering vibrations of SCB. This study highlights the importance of using molecular symmetry groups to describe fluxional molecules as the spectral selection rules must account for transitions that cross tunneling states. Chapter 8 gives the general conclusions of this thesis and describes some future work that can be built on the results of the current study.

References

[1] J. Lanne, *Annu. Rev. Phys. Chem*. 45 (1994) 179-211.

[2] A. C. Legon, *Chem. Rev*. 80 (1980) 231-262.

[3] A. Barth and C. Zscherp, *Q. Rev. Biophy,* 35 (2002) 369–430.

[4] A. Barth, *Biochemica et Biophysica Acta*, 1767 (2007) 1073-1101.

[5] L. A. Carreira, R. C. Lord and T. B. Malloy, *Large Amplitude Motions in Molecules*, Springer, Berlin Heidelberg, Vol.82 (1979) 1-95.

[6] J. Lanne, *J. Phys. Chem. A* 104 (2000) 7715-7733.

[7] T. B. Malloy, *J. Mol. Spectrosc*. 44 (1972) 505-535.

[8] J. Laane, *Pure Appl. Chem*. 59 (1987) 1307-1326.

[9] J. Laane and R. C. Loard, *J. Phys. Chem.* 48 (1968) 1508-1513.

[10] T. Ueda and T. Shimanouchi, *J. Chem. Phys.* 49 (1968) 470-471.

[11] F. A. Miller and R. J. Capwell, *Spectrochimica Acta*, 27 (1971) 947-956.

[12] C. E. Cleeton and N. H. Williams, *Phys. Rev*. 45 (1934) 234-237.

[13] S. Weiss and G. E. Leroi, *J. Chem. Phys.* 48 (1968) 962-967.

[14] J. R. Durig, S. M. Craven and J. Bragin, *J. Chem. Phys.* 53 (1970) 38-50.

[15] R. P. Bell, *Proc. R. Soc. London.* 183A (1945) 328-337.

[16] S. I. Chan, J. Zinn and W. D. Gwinn, *J. Chem. Phys.* 33 (1960) 295-296.

[17] S. I. Chan, J. Zinn, J. Fernandez and W. D. Gwinn, *J. Chem. Phys.* 33 (1960) 1643-1655.

[18] S. I. Chan, J. Zinn andW. D. Gwinn, *J. Chem. Phys.* 34 (1961) 1319-1329.

[19] S. I. Chan, T. R. Borgers, J. W. Russell, H. L. Strauss, J. Zinn and W. D. Gwinn, *J. Chem. Phys.* 44 (1966) 1103-1111.

[20] D. O. Harris, G. G. Engerholm, C. A. Tolman, A. C. Lunts, R. A. Keller, H. Kim and W. D. Gwinn, *J. Chem. Phys*. 50 (1969) 2438-2445.

[21] G. G. Engerholm, A. C. Lunts, W. D. Gwinn and D. O. Harris, *J. Chem. Phys*. 50 (1969) 2446-2457.

[22] A. G. Robiette, T. R. Borgers and H. L. Strauss, *Mol. Phys.* 42 (1981) 1519-1524.

[23] J. Laane and R. C. Lord, *J. Chem. Phys*. 48 (1968) 1508-1513.

[24] R. P. Bell, *Tunnel Effect in Chemistry*, Chapman and Hall, London (1980).

[25] P. R. Schreiner, H. R. Reisenauer, D. Ley, D. Derbig, C. –H. Wu and W. D. Allen, *Science* 332 (2011) 1300-1303.

[26] T. L. Nguyen, B. C. Xue, R. E. Weston, J. R. Barker and J. F. Stanton, *J. Phys. Chem. Lett.* 3 (2012) 1549-1553.

[27] T. J. Balle, E. J. Campbell, M. R. Keenan and W. H. Flygare, *J. Chem. Phys.* 71 (1979) 2723-2724.

[28] T. J. Balle and W. H. Flygare, *Rev. Sci. Instrum.* 52 (1981) 33-45.

[29] T. J. Balle, E. J. Campbell, M. R. Keenan and W. H. Flygare, *J. Chem. Phys.* (1980) 922-932.

[30] W. C. Pringle, *J. Chem. Phys*. 54 (1971) 4979-4988.

[31] S. Albert, K. K. Albert and M. Quack, *High-Resolution Fourier Transform Infrared Spectroscopy. Handbook of High-Resolution Spectroscopy*, John Wiley & Sons (2011).

[32] A. R. W. McKellar, *J. Mol. Spectrosc*. 262 (2010) 1-10.

[33] A. R. W. McKellar, D. W. Tokaryk, L.-H. Xu, D. R. T. Appadoo and T. May, *J. Mol. Spectrosc*. 242 (2007) 31-38.

[34] R. M. Lees, R. -J. Murphy, G. Moruzzi, A. Predoi-Cross, L. -H. Xu, D. R. T. Appadoo, B. Billinghurst, R. R. J. Goulding and S. Zhao, *J. Mol. Spectrosc*. 256 (2009) 91–98.

[35] F. K. Tchana, J. -M. Flaud, W. J. Lafferty, L. Manceron and P. Roy, *J. Quant. Spectrosc. Radiat. Transfer.* 111 (2010) 1277–1281.

[36] M. K. Bane, C. D. Thompson, D. R. T. Appadoo and D. McNaughton, *J. Chem.Phys*. 136 (2012) 084306 1-6.

[37] O. Pirali, V. Boudon, J. Oomens and M. Vervloet, *J. Chem.Phys*. 136 (2012) 024310 1-12.

[38] D. Herberth, O. Baum, O. Pirali, P. Roy, S. Thorwirth, K. M. T.Yamada, S. Schlemmer and T. F. Giesen, *J. Quant. Spectrosc. Radiat. Transfer.*113 (2012) 1127-1133.

[39] S. Albert, P. Lerch, R. Prentner and Martin Quack, *Angew. Chem. Int. Edit.*, 52 (2013) 346-349.

[40] J. -C. Hilico, O. Robert, M. Loëte, S. Toumi, A. S. Pine and L. R. Brown, *J. Mol. Spectrosc*. 208 (2001) 1-13.

[41] S. Albert, S. Bauerecker, V. Boudon, L. R. Brown, J. -P. Champion, M. Loëte, A. Nikitin and M. Quack, *Chem. Phys.* 356 (2009) 131-146.

[42] M. Johnston and D. M. Dennison, *Phys.Rev.* 48 (1935) 863-883.

[43] H. A. Jahn, *Proc. Roy. Soc. (London)* A168 (1938) 469-495.

[44] H. A. Jahn, *Proc. Roy. Soc. (London)* A171 (1939) 450-468.

[45] D. R. J. Boyd and H. C. Longuet-Higgins, *Proc. Roy. Soc. (London)* A213 (1952) 55-73.

[46] H. H. Nielsen, *Rev. Mod. Phys*. 23 (1951) 90-136.

[47] T. Oka and Y. Morino, *J. Mol. Spectrosc*. 6 (1951) 472-482.

[48] I. M. Mills, *Pure Appl. Chem*. 11 (1965) 325-344.

[49] L. A. Carreira and R. C. Lord, *J. Chem.Phys*. 51 (1969) 2735-2744.

[50] A. G. Robiette, T. R. Borgers and H. L. Strauss, *Mol. Phys.* 42 (1981) 1519-1524.

[51] D. Cremer, O. V. Dorofeeva and V. S. Mastryukov, *J. Mol. Struct.* 75 (1981) 225-240.

[52] J. C. López, S. Blanco, A. Lessari and J. L. Alonso, *J. Chem. Phys.* 114 (2001) 2237-2350.

Chapter 2

Fourier transform microwave spectroscopy

Fourier transform microwave (FTMW) spectroscopy was employed to investigate the pure rotational energy levels of the four-membered heterocyclic molecules presented in this thesis. The basic design, operating principles and theoretical background of FTMW spectroscopy are briefly discussed in this chapter, as well as the general schemes to observe and assign pure rotational transitions.

2.1 Brief overview of FTMW spectroscopy

Compared to the traditional way of obtaining microwave spectra which measures the microwave absorbance of a static, low pressure gas sample in an evacuated waveguide cell, FTMW spectroscopy takes a different approach. This technique is described in detail by Grabow and Caminati.[1] Figure 2.1 shows a schematic of the FTMW spectrometer used in this study. Briefly, the vapour pressure of a sample of the molecule of interest is mixed with a noble gas as the carrier gas (pressure 2-10 atm) and the mixture is expanded into an evacuated microwave (Fabry-Perot) cavity (initially at a pressure of ~10^{-6} Torr) that consists of two concave mirrors inside a vacuum chamber. As a result of this process, a pulsed molecular beam is produced via supersonic expansion. The rotational temperature of the beam is effectively cooled to a few Kelvin such that the molecules occupy only the lowest rotational energy levels. A short microwave pulse at a fixed frequency is coupled to the molecular beam. If the subject molecules have a rotational transition within the cavity's bandwidth at the incident microwave frequency,

Figure 2.1: A schematic of the Fourier transform microwave spectrometer.

stationary mirror

Servo motor to adjust the separation of two mirrors

Gas sample manifold

antenna

nozzle

movable mirror

Free induction decay in time domain

Fourier transform

Spectrum in frequency domain
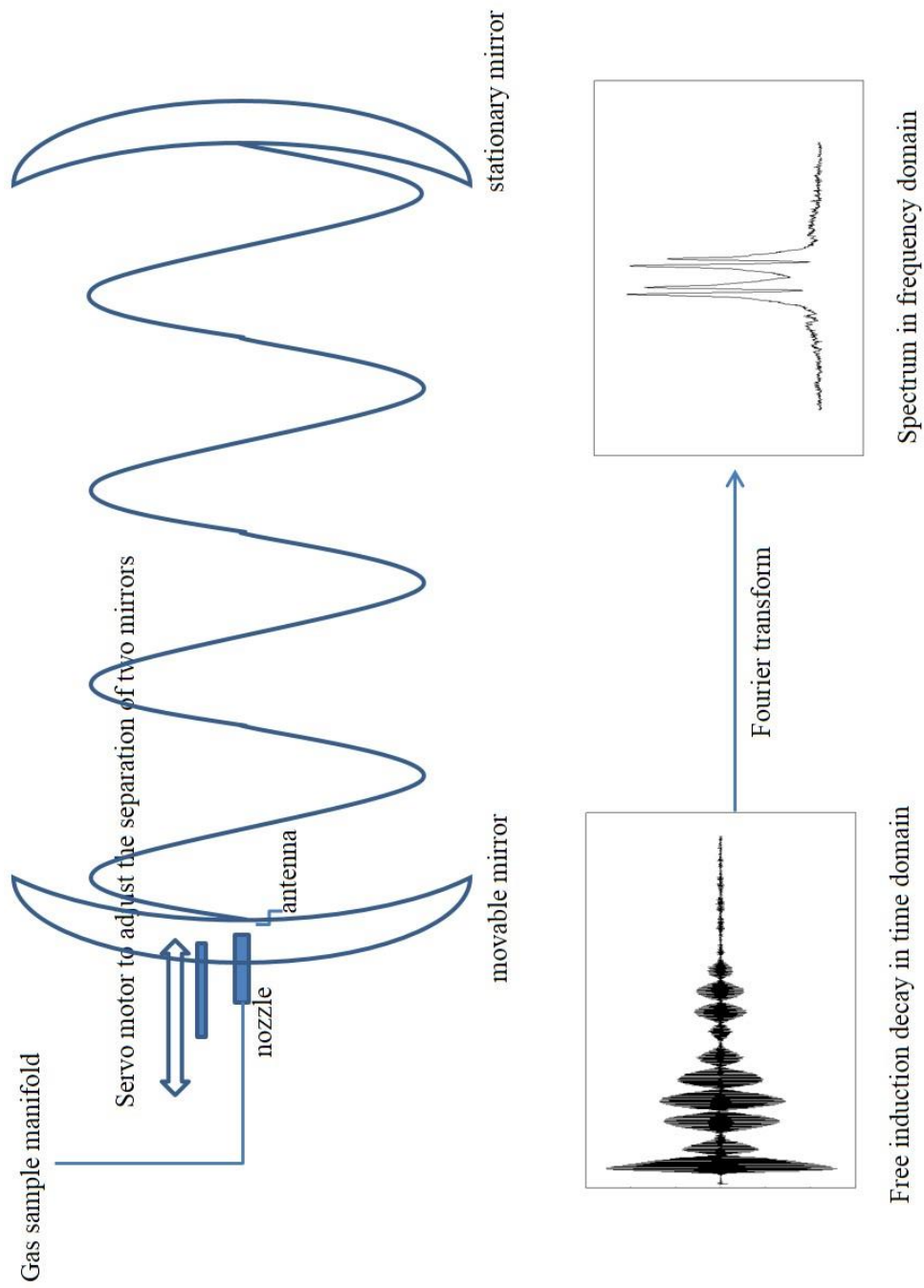
the interaction leads to the alignment of the dipole moments of individual molecules in the electromagnetic field and the molecules rotate in phase. Thus, a macroscopic polarization of the molecular ensemble is created. As the molecular beam moves along the length of the microwave cavity and the molecules collide at the cavity wall, the recorded transient emission signal decays as a function of time. This decay (Free induction decay, FID) is Fourier transformed to yield a spectrum in the frequency domain.

2.2 Design of the FTMW spectrometer

The pure rotational spectra discussed in this thesis were obtained using a pulsed-nozzle Fourier transform microwave spectrometer in the van Wijngaarden group. This spectrometer is based on the Balle-Flygare design.[2, 3, 4] A FTMW spectrometer consists of three main components: a microwave cavity, a pulsed nozzle to create molecular beam and the microwave generation and detection electronics to yield the frequency domain spectrum. The details of this FTMW instrument have been given elsewhere,[5] and they are briefly described here.

A microwave cavity consisting of two concave spherical aluminum mirrors (35.6 cm in diameter with a radius of curvature of 84 cm and approximately 65 cm apart) is installed in a stainless steel vacuum chamber, which is evacuated by a diffusion pump (Varian VHS-10, 3650 L s^{-1}) to a background pressure of $\sim 10^{-6}$ Torr. The distance between the two mirrors is fine-tuned into resonance with the chosen microwave frequency by a computer-controlled servo motor. The gaseous sample, prepared by mixing a few per cent of the molecule of interest with a rare gas (Ar, Ne, He) at a total pressure of a few atmospheres, is introduced into the cavity via supersonic expansion

from a pulsed valve nozzle (General Valve, Series 9, orifice diameter of 1.0 mm) mounted near the center of one mirror.

2.2.1 Fabry-Perot cavity

Historically, a Fabry-Perot cavity was used in laser resonators. [6,7,8,9] A comprehensive review on the cavity was given by Kogelnik and Li.[10] The purpose of having a microwave Fabry-Perot cavity is to store the electromagnetic field amplitude in resonator modes with a narrow frequency width. The field distribution for a transverse electromagnetic mode (TEM_{mnq}) inside a cavity has a Gaussian-beam shape and can be given as:

$$E\ (r,t)\ =\ 2\hat{z}\ \xi(r)\ \cos\omega t\ , \tag{2.1}$$

$$\xi(r) = \xi_0 H_m \left(\sqrt{2}\ \frac{x}{w(y)}\right) H_n \left(\sqrt{2}\ \frac{z}{w(y)}\right) \frac{w_0}{w(y)}\ e^{-\frac{\rho^2}{w^2(y)}} \cdot x \cdot \cos(ky + \frac{k\rho^2}{2R} - \phi - \frac{\pi q}{2}) \tag{2.2}$$

where

$$\rho^2 = x^2 + z^2$$

$$w(y) = w_0 \left[1 + \left(\frac{\lambda y}{\pi w_0{}^2}\right)^2\right]^{\frac{1}{2}}$$

$$w_0 = \left(\frac{\lambda}{2\pi}\ [d(2R - d)]^{\frac{1}{2}}\right)^{\frac{1}{2}}$$

$$\Phi = \ \tan^{-1} \left(\frac{\lambda y}{\pi w_0{}^2}\right)$$

$$k = \ \frac{\omega_c}{c} \tag{2.3}$$

The x, y, z are the coordinates with the origin being at the center of the cavity as shown in Figure 2.2, the terms H_m and H_n are polynomials of order m and n, respectively,

Figure 2.2: The coordinate system used in a Fabry-Perot cavity; *d* is the separation between the two mirrors and R is the radius of
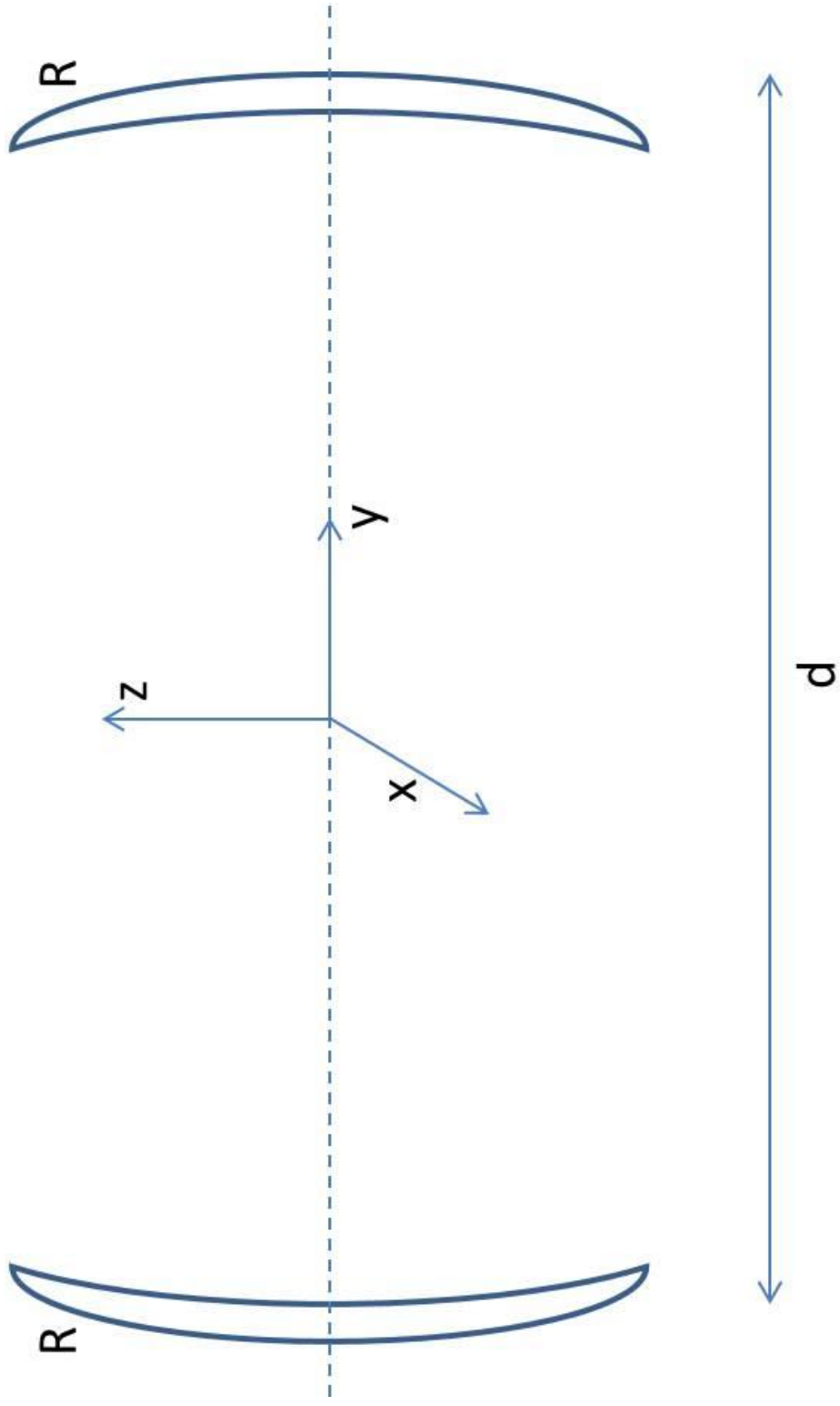
which are unity for a fundamental mode, λ is the radiation wavelength in free space, c is the speed of light, w(y) is the distance between a point on the y-axis and the point where the field amplitude is $\frac{1}{e}$ of its value as shown in Figure 2.3. The term $w_0 = w(y = 0)$ is known as the *beam waist* which is also the minimum value of w(y). For the instrument in van Wijngaarden's group, the beam waist at 10 GHz can be calculated using the radius of curvature of mirror, 84 cm and mirror separation of 65 cm and is 6.2 cm. As seen in Figure 2.3, the phase front of the cavity modes is planar only at y = 0; the curvature elsewhere along the y-axis caused by the curved mirrors are taken into account by the term $\frac{k\rho^2}{2R}$ in Equation 2.2. The parameter R is the curvature of both mirrors in the cavity, d is the separation between them and ω_c is the central angular frequency inside the cavity. The number of half wavelengths between the two mirrors is given by q + 1.

When the resonant frequency ν_c is obtained, one must satisfy the following condition:

$$\nu_c = \nu_0 \left[(q + 1) + \frac{1}{\pi}(m + n + 1)\cos^{-1}(1 - \tfrac{d}{R}) \right] \tag{2.4}$$

For a fundamental mode, m = n = 0, then Equation 2.4 becomes:

$$\nu_c = \nu_0 \left[(q + 1) + \frac{1}{\pi}\cos^{-1}(1 - \tfrac{d}{R}) \right] \tag{2.5}$$

where $\nu_0 = \frac{c}{2d}$ is often referred as the *free spectral range* of the resonator (FSR) and it represents the distance between two adjacent modes inside the cavity which are often well separated. For example, for the cavity used in this study with d = 65 cm, adjacent modes are separated by $\nu_0 = 231$ MHz.

Figure 2.3: Phase fronts (a) and intensity distribution (b) of the TEM$_{00q}$ fundamental mode inside a Fabry-Perot cavity. The beam waist w_0 is the distance between the origin and the point where the field strength is $\frac{1}{e}$
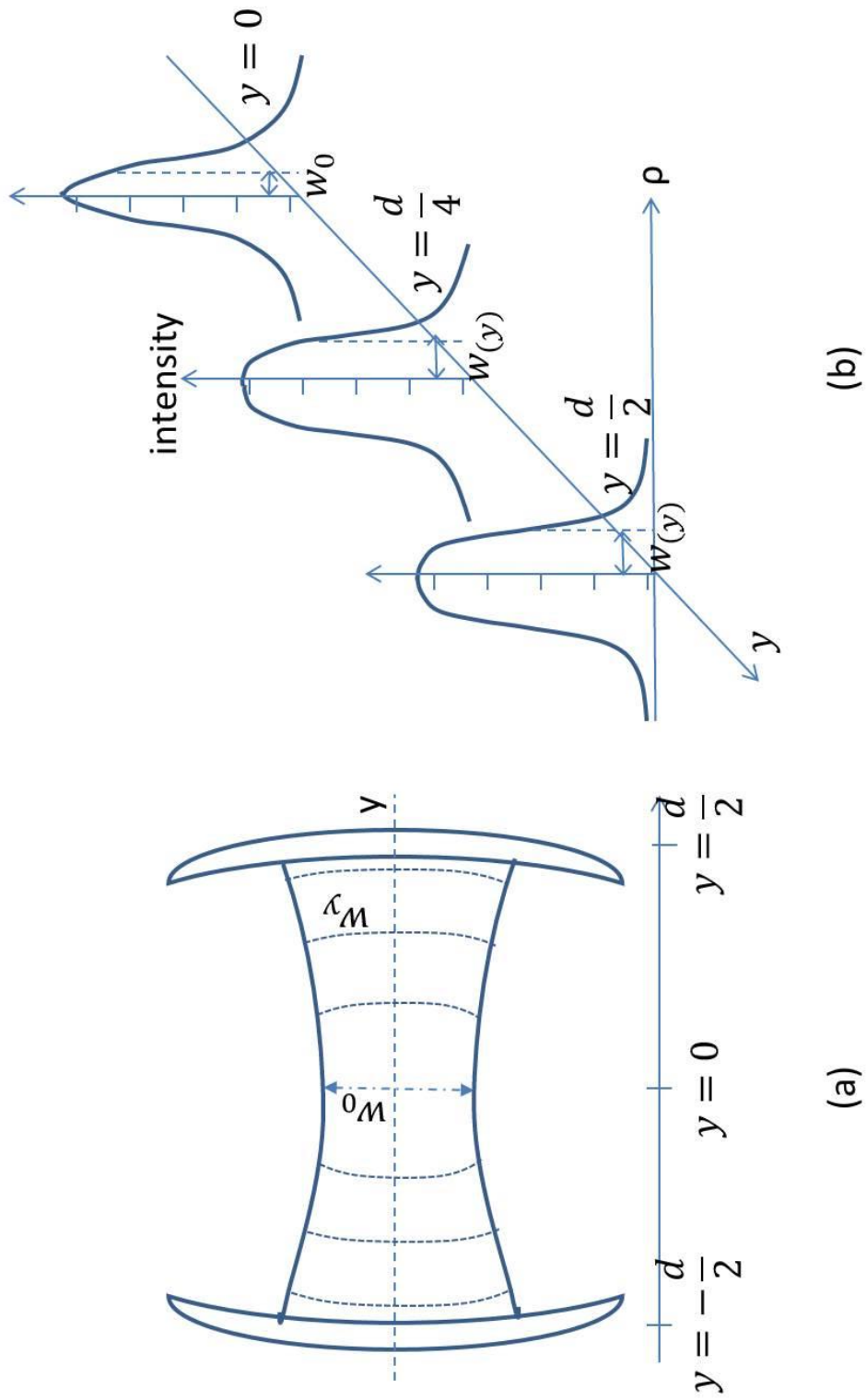
2.2.2 The Q factor

The quality factor (Q factor) of a resonator is a measure of how much energy can be stored in a cavity and for how long. It is thus an important property. The definition of Q can be given as:

$$Q = \omega_c \frac{W}{P} \tag{2.6}$$

where ω_c is the angular frequency of radiation and W is the total (electromagnetic) energy stored in the cavity. The power dissipation P can be expressed as:

$$P = -\frac{dW}{dt} = \frac{W}{\tau_c} \tag{2.7}$$

where τ_c is the time it takes for the field amplitude to decay to $\frac{1}{e}$ of its initial value (often referred as decay constant). Substitution of Equation 2.7 into Equation 2.6 gives:

$$Q = \omega_c \tau_c \tag{2.8}$$

The power loss is mainly due to the finite conductivity of the metal of the mirror. Assuming that this is the only source of energy dissipation, the Q factor can be calculated by:

$$Q = \frac{d}{2\delta} \tag{2.9}$$

where δ is the skin depth of the mirror at which the initial radiation strength drops to $\frac{1}{e}$ and has a value of 8.5×10^{-5} cm at 10 GHz for aluminum. The Q factor of the microwave cavity used in this study with d = 65 cm at 10 GHz is thus $\sim 3.8 \times 10^5$. It should be noted that with such a high Q factor, the decay constant τ_c is on the order of microseconds (or fractions of microseconds) in the microwave region. For example, for a cavity with a Q of 4×10^4 at 10 GHz, τ_c=0.16 μs.[3] That is to say, the radiation has already travelled more

than 70 passes between the mirrors before the intensity has decreased to $\frac{1}{e}$ of its initial value.

2.2.3 The microwave excitation and detection scheme.

The excitation microwave pulse is introduced into the cavity through a wire hook antenna located at the center of the moving mirror. The emission signal from the sample is received by the same antenna. The microwave detection and excitation circuits are shown in Figure 2.4 and the numbering used here follows that in this schematic. A short (0.1-4 µs) microwave pulse at an excitation frequency of v_0 which is 30 MHz below the anticipated molecular transition frequency is generated by using an Agilent microwave synthesizer (4) and two single pole, double throw (SPDT) *p-i-n*-diode switches (6a, 6b). As the emission signal is maximized if the molecular ensemble is fully polarized, the pulse length should be optimized to ensure the highest achievable sensitivity. The tripled output of the 10 MHz reference generated by the radiofrequency (RF) synthesizer (1) and a single sideband mixer (3) are used to produce the upper sideband of 30 MHz + v_0. The doubled output of the same 10 MHz reference (2) provides the system clock for all pulses and delays during the experiment. The power of the microwave excitation pulse can be adjusted by the use of an amplifier (9) and a variable attenuator (10). Should there be molecular transitions within the bandwidth of the cavity (~1 MHz), a macroscopic polarization occurs under proper excitation conditions (duration and delay of the gas and microwave pulses). The subsequent weak molecular rotation signal occurs at a frequency of v_0 + 30 MHz +Δ (where Δ is the small frequency difference between the molecular rotational frequency and the incident excitation frequency) and is amplified by a low

27

Figure 2.4: The microwave excitation and detection circuit. (1) RF synthesizer. (2) Doubler and amplifier. (3) Tripler. (4) Microwave synthesizer. (5) SPDT GaAs rf switch. (6) 2 SPDT *p-i-n*-diode MW switch. (7) Single sideband mixer. (8) Coaxial transfer switch. (9) Microwave power amplifier. (10) Variable attenuator. (11) Fabry-Perot cavity. (12) Diode detector. (13) Low noise microwave amplifier. (14) Image rejection mixer. (15) RF amplifier. (16) Bandpass filter. (17) RF demodulator. (18) Lowpass filter. (19) Transient recorder card.
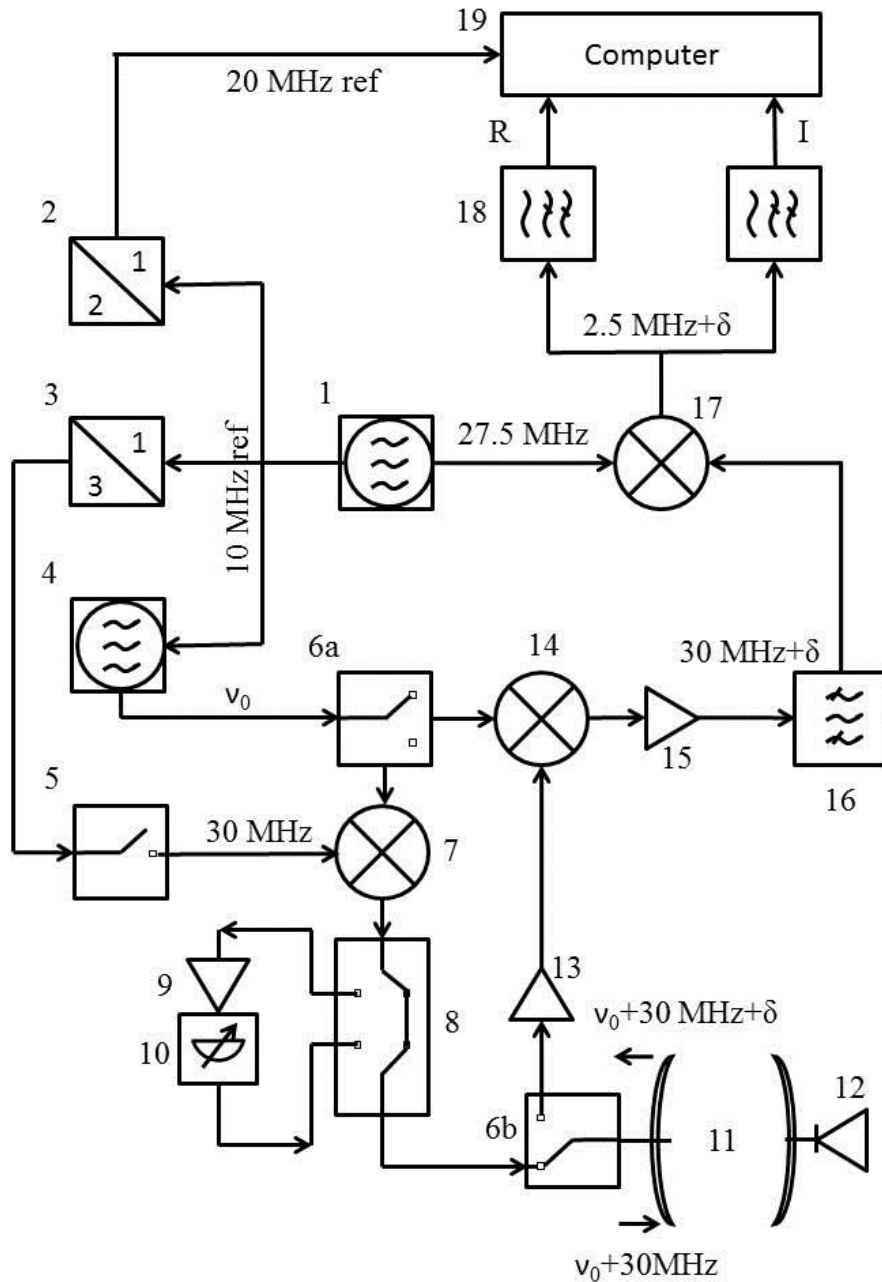
noise amplifier (13). The microwave emission signal is then mixed down to the RF range (30 MHz +Δ) using an image rejection mixer (14) and the initial frequency ν_0 from the microwave synthesizer (4) through the SPDT diode switch (6a) that generates the excitation pulse. The resulting RF signal is further amplified (15) to compensate for losses due to mixing, followed by a second down conversion to yield 2.5 MHz + Δ using the 27.5 MHz output of the RF synthesizer (1). The quadrature detection of both the real and imaginary emission signal is achieved by the RF demodulator (17). Finally the FID signal is digitized using a two-channel transient recorder card (19) in a personal computer and Fourier transformed to yield the spectrum in the frequency domain which is displayed as a power spectrum. The whole pulse sequence is repeated and the signal is averaged to improve the signal-to-noise ratio (S/N) of the spectrum. As the molecular beam and the microwave pulses run in a parallel arrangement and the antenna is stationary during the process, a Doppler splitting appears in the observed spectra but the transition frequency is taken as the average of the two Doppler components. The spectrometer is controlled by the FTMW++ software program[11] which allows automated measurements with pre-set experimental parameters.

2.3 Molecular beams

The concept of molecular beams as they apply to spectroscopy is explained in detail by Havenith.[12] When a pressurized (P_0) gas sample enters an evacuated system (P_1), the molecules are expanded by the pressure difference $P_1 - P_0$. The supersonic expansion (when gas flow velocity exceeds the speed of sound) occurs when the ratio $\frac{P_1}{P_0}$ is greater than two.[12] This expansion is an adiabatic process as no heat exchange takes place

between the nozzle walls and the molecules.[13] As a consequence of conservation of energy before/after the expansion, the following equation holds:

$$U_0 + P_0 V_0 + \frac{1}{2} M v_0^2 = U_1 + P_1 V_1 + \frac{1}{2} M v_1^2 \tag{2.10}$$

where $U = U_{translational} + U_{vibrational} + U_{rotational}$ represents the total internal energy in its three components, PV is the potential energy and $\frac{1}{2} M v_1^2$ is the kinetic energy of the expanding gas. The superscripts 0 and 1 denote the gas sample before and after the expansion, respectively. As the mass flow of the gas during the expansion is very small compared to the total mass available, $v_0 \approx 0$ and the fact that the pressure after expansion P_1 is very small compared to the initial pressure P_0 implies $P_1 \approx 0$. Equation 2.10 becomes:

$$U_0 + P_0 V_0 \approx U_1 + \frac{1}{2} M v_1^2 \tag{2.11}$$

Equation 2.11 implies that after the supersonic expansion (a large v_1), most of the internal energy and potential energy of the gas sample in the reservoir are converted into the kinetic energy ($\frac{1}{2} M v_1^2$) in the jet, resulting in a cold beam (U_1 much smaller than U_0).

The translational temperature $T_{translational}$, which is a measure of the translational velocity distribution of the molecules, is effectively cooled in the initial stage of the expansion via collisions among the molecules. This can be interpreted on the microscopic level as the faster moving molecules catching up with slower moving ones due to exchanging kinetic energy during collision. The consequence is that instead of moving randomly as at equilibrium, molecules in a jet move at almost the same velocity with each other along the expansion axis and thus a narrow width of velocity distribution is achieved.

The rotational energy is also reduced in collisions during the adiabatic expansion where $U_{rotational}$ is converted to $U_{translational}$. As a result, the rotational temperature $T_{rotational}$ decreases after expansion and molecules are repopulated towards the lower energy rotational states in a jet. However, the rotational energy cannot be completely transferred into translational energy in the adiabatic expansion as the cross section $\sigma_{rotational \to translational}$ is generally smaller than $\sigma_{translational \to translational}$, but rotational cooling is efficient such that $T_{rotational}$ is only a few Kelvin higher than $T_{translational}$.

The vibrational temperature is cooled in a similar manner but with smaller cooling cross section $\sigma_{vibrational \to translational}$ compared to $\sigma_{rotational \to translational}$. As a result, a general trend of $T_{translational} < T_{rotational} < T_{vibrational}$ is observed due to the effectiveness in the cooling processes of all three temperatures mentioned above.

Compared to waveguide-type microwave measurements, the FTMW technique offers increased sensitivity and resolution for the following reasons:

1) As a result of rotational cooling in the supersonic jet, only a few rotational states are populated compared to a room temperature sample in a waveguide instrument. Therefore, the sensitivity of detecting transitions involving these low lying states is enhanced, albeit transitions between high energy states are reduced in intensity.

2) The collision-free environment of the jet after the expansion removes pressure broadening, while Doppler broadening is reduced by the fact that molecules now travel in one direction (one translational degree of freedom). The spectral resolution is also influenced by the length of the emission signal recorded in the

time domain, which approaches ~7 kHz at Full-Width-at-Half-Maximum (FWHM) when the FID is recorded for 400 μs. Compared to that of a few hundred kHz in waveguide measurements, the reduced line width allows studies of unique spectral features (such as tunnelling splitting and hyperfine structures) that are on the order of several kHz.

2.4 General procedures to observe and assign molecular rotational transitions

2.4.1 Theoretical considerations

The quantum mechanical assignment and prediction of microwave transitions based on the rotational Hamiltonian was comprehensively discussed by Gordy and Cook.[14] This Hamiltonian may be implemented using the SPFIT and SPCAT programs written by Pickett.[15] This section provides a basic description of the theoretical background of molecular rotation.

2.4.1.1 Rotational Hamiltonian for asymmetric tops

The rotational (rigid rotor) Hamiltonian operator can be expressed as:

$$\hat{H} = \frac{\hat{J}_a^2}{2I_a} + \frac{\hat{J}_b^2}{2I_b} + \frac{\hat{J}_c^2}{2I_c} \tag{2.12}$$

where $\hat{J}_a$, $\hat{J}_b$ and $\hat{J}_c$ are the rotational angular momentum operators along the a-, b- and c-axes, respectively, in the principal axis system and I_a, I_b and I_c are the moments of inertia in the same axis system. For asymmetric tops, the rotational constants $A = \frac{\hbar^2}{2I_a}$,

$B = \frac{\hbar^2}{2I_b}$ and $C = \frac{\hbar^2}{2I_c}$ have different values. If one substitutes the expressions of the rotational constants into Equation 2.12, the following expressions are obtained:

$$\hbar^2 \hat{H} = A \hat{j}_a^2 + B \hat{j}_b^2 + C \hat{j}_c^2$$

$$= \left(\frac{A+B}{2}\right)(\hat{j}_a^2 + \hat{j}_b^2) + C\hat{j}_c^2 + \left(\frac{A-B}{2}\right)(\hat{j}_a^2 + \hat{j}_b^2)$$

$$= \left(\frac{A+B}{2}\right)\hat{j}^2 + \left(C - \frac{A+B}{2}\right)\hat{j}_c^2 + \left(\frac{A-B}{4}\right)((\hat{j}^+)^2 + (\hat{j}^-)^2) \qquad (2.13)$$

where $\hat{j}^+$ and $\hat{j}^-$ are raising and lowering operators, respectively. The following angular momentum matrix elements for symmetric tops expressed in bra-ket notation[16] are needed for evaluating Equation 2.13:

$$\langle J\,K|\hat{j}^2|JK\rangle = \hbar^2\,J(J+1)$$

$$\langle J\,K|\,\hat{j}_c^2|JK\rangle = \hbar^2\,K^2$$

$$\langle J\,K-2|\hat{j}^+|J\,K\rangle = \hbar^2\,\sqrt{(J+K)(J-K+1)(J+K-1)(J-K+2)}$$

$$\langle J\,K+2|\hat{j}^-|J\,K\rangle = \hbar^2\,\sqrt{(J-K)(J+K+1)(J-K-1)(J+K+2)} \qquad (2.14)$$

where J is the rotational angular momentum quantum number and K is the projection of $\hat{j}$ onto the symmetry axis (z-axis in molecular system) of a symmetric top. For a given J value, the Hamiltonian in the matrix form has a dimension of $(2J+1) \times (2J+1)$. The eigenvalues can be obtained by diagonalization of the Hamiltonian matrix. For instance, a 3×3 matrix can be set for the J=1 level with K= -1, 0 and 1 and the solutions can be solved straightforwardly as A+B, B+C and A+C. Although the case above provides an example that an exact solution can be reached for certain quantum numbers, it should be noted that there is *no analytical solution to the Schrödinger equation* for asymmetric tops and numerical solutions are obtained by a computer; in this thesis, the SPFIT/SPCAT program was used for this purpose.[15]

2.4.1.2 Centrifugal distortion

A rigid rotor is an ideal model while in reality, a molecule experiences a "fictitious" centrifugal force in the rotational reference frame. As a result, the bonds are distorted and the moments of inertia are changed during rotation. From a spectroscopic point of view, the observed frequencies of transitions are shifted from these idealized values based on a molecule that is "rigid". This departure is small compared to the transition frequencies themselves and has dependence on the J and K values. Two reduced representations, known as asymmetric (A) and symmetric (S) forms, were developed by Watson. [17, 18, 19] Pickett incorporated Watson's representations into the SPFIT/SPCAT program.[15] For the work in this thesis, the fitting was performed using only the A-reduced Hamiltonian.

2.4.1.3 Rotational selection rules in asymmetric tops

A permanent electric dipole moment (μ) is required for observation of rotational transitions. If the dipole component(s) along the *a*-, *b*- and *c*- axis is (are) non-zero, transitions with different selection rules are expected.

1) *a*-type selection rules.

   If $\mu_a \neq 0$, transitions with $\Delta K_a = 0 \, (\pm 2, \pm 4, ...)$ and $\Delta K_c = 1 \, (\pm 3, \pm 5, ...)$ are allowed, i.e. *eo↔ee* and *oe↔oo* (e(o) for even (odd) for $K_a(K_c)$).

2) *b*-type selection rules.

   If $\mu_b \neq 0$, transitions with $\Delta K_a = \pm 1 \, (\pm 3, \pm 5, ...)$ and $\Delta K_c = \pm 1 \, (\pm 3, \pm 5, ...)$ are allowed, i.e. *eo↔oe* and *ee↔oo*.

3) *c*-type selection rules.

If $\mu_c \neq 0$, transitions with $\Delta K_a = \pm 1 \, (\pm 3, \pm 5, ...)$ and $\Delta K_c = 0 \, (\pm 2, \pm 4, ...)$ are allowed, i.e. *oe↔ee* and *eo↔oo*.

$\Delta J = \pm 1, 0$ is required for all three types

The K_a and K_c labels are quantum numbers for asymmetric rotors that arise from the fact that K is no longer a valid label as it is not necessary for asymmetric tops to have a symmetry axis. They are labels to correlate energy levels between asymmetric tops and the two symmetric top limits (K_a for prolate and K_c for oblate types) rather than "good" quantum numbers with physical meaning.

2.4.2 Spectrum collection and analysis scheme

Since the bandwidth of the microwave cavity is very narrow (only ~1 MHz of the instrument's spectral range of 4-26 GHz), choosing a proper frequency range to search for molecular rotational transitions is a very important factor in planning an experiment. To start, an estimated structure of the molecule of interest is obtained by performing *ab initio* calculations using the Gaussian 03W software package.[20] Once the structure is optimized, the predicted permanent dipole moment components along the three principal inertial axes provide information about the selection rules of the anticipated rotational transitions. Using the calculated rotational constants (A, B and C), a list of microwave lines with their predicted transition frequencies and intensities within the spectral range of the FTMW spectrometer is generated using a Hamiltonian model in the SPCAT program.

The next stage is to scan for the first transition. Based on the prediction of molecular lines, the strongest transitions are considered the best candidates to begin the search. An automated spectral survey consisting of multi-step measurements should be undertaken to cover the vicinity of the predicted transition frequency. For example, if one strong transition is predicted at 12000 MHz, the FTMW spectrometer may be set to start measuring at 11950 MHz with 500 steps (separated by 200 kHz). In total, a search range of ± 50 MHz about 12000 MHz is typically examined. Depending on how close the predicted structure is to the real ground state molecular structure, the actual search range may vary. Once the target line is located during the scan, a detailed measurement is made to scrutinize the precise frequency of the transition.

The experimental conditions and instrumental settings are also optimized to achieve the best S/N ratio in a given spectral range to increase the efficiency of searching for other transitions. After several lines (N>3 for asymmetric rotors) are observed and assigned to the rotational quantum numbers, a preliminary fit to the Hamiltonian model is made using the SPFIT program[15] and the results are used to obtain a more reliable predicted line list using the SPCAT program. From this point, the scan range can typically be reduced to a few hundred kHz, provided that the preliminary assignment is correct and the molecule is fairly rigid. With more lines assigned and fit, the parameters in the Hamiltonian model improve, giving better prediction of the remaining transitions. Ultimately, an unambiguous assignment is made based on the requirement that 1) the Hamiltonian model accounts for all observed lines; 2) the determined parameters are physically meaningful (i.e. they are well-determined and sensible in both sign and magnitude).

Weak rotational transitions often present challenges to the observation and assignment process. When searching for transitions due to minor isotopic species in natural abundance, the search effort is reduced by using the percentage difference between the calculated and observed transitions of the corresponding main isotopic species transition to "scale" the calculated frequency for the minor isotopologues. As the minor isotopologues' emission signal is normally extremely weak, it is very important to pay attention to the signal consistency across the full spectral range by checking the intensity of a known parent line regularly and re-optimizing the experimental conditions as needed.

References

[1] J. -U. Grabow and W. Caminati, *Frontiers of Molecular Spectroscopy: Microwave spectroscopy*, Elsevier, Amsterdam Oxford (2009).

[2] T. J. Balle, E. J. Campbell, M. R. Keenan and W. H. Flygare, *J. Chem. Phys.* 71 (1979) 2723-2724.

[3] T. J. Balle, E. J. Campbell, M. R. Keenan and W. H. Flygare, *J. Chem. Phys.* (1980) 922-932.

[4] T. J. Balle and W. H. Flygare, *Rev. Sci. Instrum.* 52 (1981) 33-45.

[5] G. Sedo and J. van Wingaarden, *J. Chem. Phys.* 131 (2009) 044303 1-5.

[6] R. H. Dicke, U. S. Patent, September 9 (1958) 2 851 652.

[7] A. M. Prokhorov, *JETP (USSR).* 34 (1958) 1658-1659.

[8] A. M. Prokhorov, *Sov. Phys. JETP,* 7(1958)1140-1141.

[9] A. L. Schawlow and C. H. Townes, *Phys. Rev.* 29(1958)1940-1949.

[10] B. R. Kogelnik and T. Li, *Proc. IEEE.* 54 (1966) 1312-1329.

[11] J. -U. Grabow, Universität Hannover, available at http://www.pci.unihannover.de/~lgpca/spectroscopy/ftmw.

[12] M. Havenith, *Infrared Spectroscopy of Molecular Clusters*, Springer-Verlag, Berlin Heidelberg (2002).

[13] W. Demtröder, *Laser Spectroscopy in Molecular Beams*, Springer-Verlag, Berlin Heidelberg (2008).

[14] W. Gordy and R. L. Cook, *Microwave Molecular Spectra*, Wiley-Interscience, New York (1984).

[15] H. M. Pickett, *J. Mol. Spectrosc*. 148 (1991) 371-337.

[16] P. A. M. Dirac, *Math. Proc. Cambridge Philos. Soc.* 35 (1939) 416-418.

[17] J. K. G. Watson, *J. Chem. Phys.* 45 (1966) 1360-1361.

[18] J. K. G. Watson, *J. Chem. Phys.* 46 (1967) 1935-1349.

[19] J. K. G. Watson, *Vibrational Spectra and Structure* (edited by J. R. Durig) Elsevier, Amsterdam, Vol.6 (1977) 1-89.

[20] Gaussian 03, Revision C.02, M. J. Frisch, G. W. Trucks, H. B. Schlegel, G. E. Scuseria, M. A. Robb, J. R. Cheeseman, J. A. Montgomery, Jr., T. Vreven, K. N. Kudin, J. C. Burant, J. M. Millam, S. S. Iyengar, J. Tomasi, V. Barone, B. Mennucci, M. Cossi, G. Scalmani, N. Rega, G. A. Petersson, H. Nakatsuji, M. Hada, M. Ehara, K. Toyota, R. Fukuda, J. Hasegawa, M. Ishida, T. Nakajima, Y. Honda, O. Kitao, H. Nakai, M. Klene, X. Li, J. E. Knox, H. P. Hratchian, J. B. Cross, V. Bakken, C. Adamo, J. Jaramillo, R. Gomperts, R. E. Stratmann, O. Yazyev, A. J. Austin, R. Cammi, C. Pomelli, J. W. Ochterski, P. Y. Ayala, K. Morokuma, G. A. Voth, P. Salvador, J. J. Dannenberg, V. G. Zakrzewski, S. Dapprich, A. D. Daniels, M. C. Strain, O. Farkas, D. K. Malick, A. D. Rabuck, K. Raghavachari, J. B. Foresman, J. V. Ortiz, Q. Cui, A. G. Baboul, S. Clifford, J. Cioslowski, B. B. Stefanov, G. Liu, A. Liashenko, P. Piskorz, I. Komaromi, R. L. Martin, D. J. Fox, T. Keith, M. A. Al-Laham, C. Y. Peng, A. Nanayakkara, M. Challacombe, P. M. W. Gill, B. Johnson, W. Chen, M. W. Wong, C. Gonzalez and J. A. Pople, Gaussian, Inc., Wallingford, CT USA (2004).

Chapter 3

High resolution Fourier transform infrared spectroscopy

The high resolution vibrational spectra of the four-membered heterocycles presented in this thesis were recorded using a commercially available Bruker IFS HR 125 Fourier transform infrared (FTIR) spectrometer at the Canadian Light Source (CLS) far infrared beamline. This chapter gives a brief description of the principle and design of a FTIR spectrometer, theoretical background of rovibrational spectroscopy and an outline of the general scheme to analyze rotationally resolved vibrational spectra.

3.1 Overview of FTIR spectroscopy

FTIR spectroscopy is based on the design of the Michelson interferometer[1, 2] which has a simple optical system: an infrared source, a beamsplitter, a detector and two mirrors as shown in Figure 3.1. The operation principle of an interferometric FTIR spectrometer is briefly discussed here. The incident beam from an IR light source (S) is split at the beamsplitter (BS). One half of the beam is reflected to the movable mirror M_1 and bounces back to the beamsplitter. The other half is transmitted through the beamsplitter and travels to the stationary mirror M_2 and returns to the beamsplitter. Depending on the optical path difference between the movable mirror M_1 and stationary mirror M_2, the subsequent recombination of beams reflected by both mirrors at the beamsplitter interferes constructively or destructively.

The recorded signal at the detector D, or interferogram when a polychromatic light source is used, can be expressed in the form of:

Figure 3.1: A schematic of the Michelson interferometer (M_1: movable mirror, M_2: fixed mirror, S: source, BS: beamsplitter D: detector, C: computer to carry out fast Fourier transformation, δ: optical path difference, L: the maximum optical path difference to achieve highest resolution).
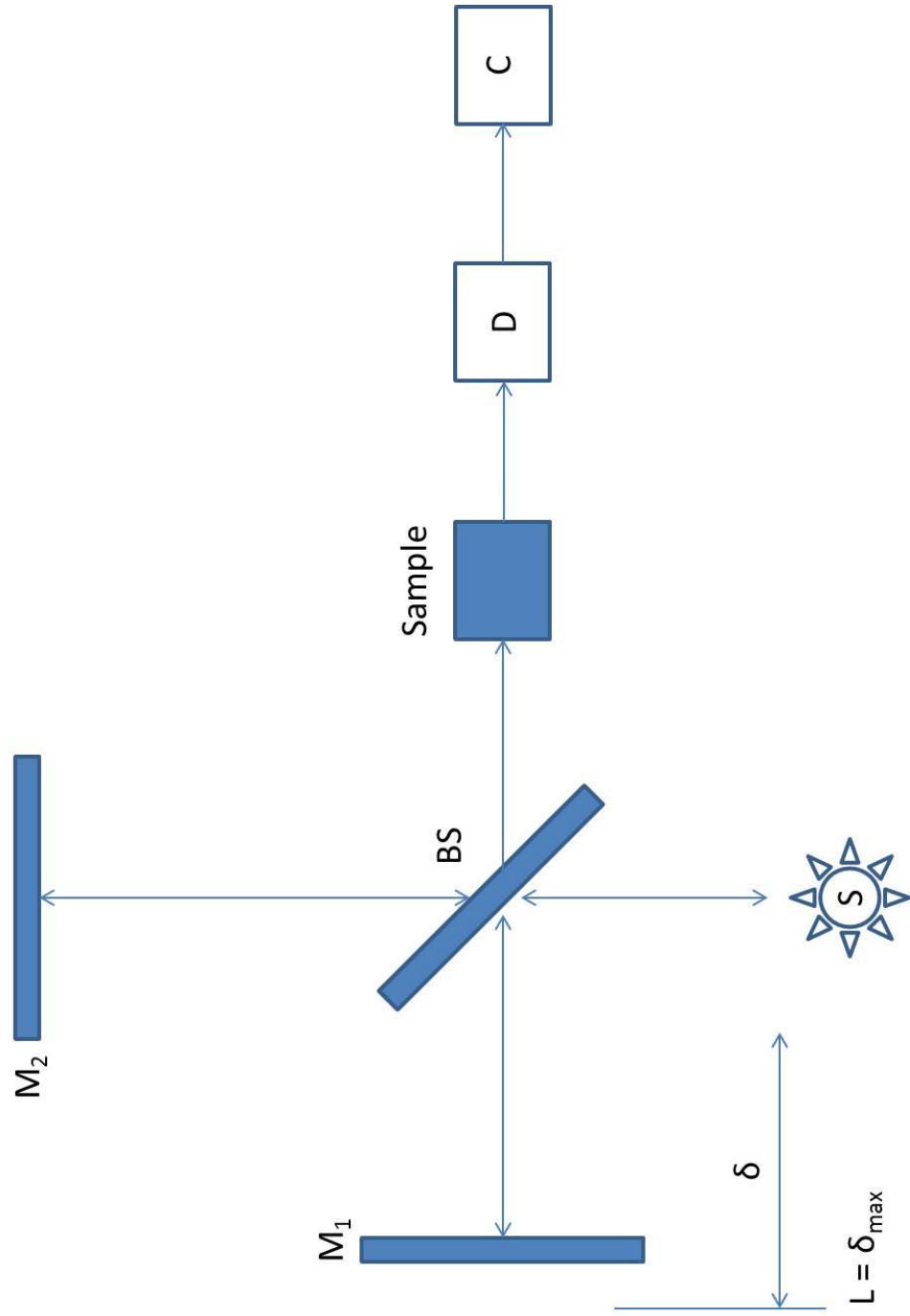
$$I(\delta) = \int_0^\infty I(\tilde{\nu}) \cos(2\pi\tilde{\nu}\delta)d\tilde{\nu} \qquad (3.1)$$

where $I(\tilde{\nu})$ is the wavenumber dependent spectral intensity and $I(\delta)$ is the optical path difference (δ) dependent spectral intensity which is also the cosine Fourier transform integral of $I(\tilde{\nu})$. Thus, applying the inverse Fourier transform of $I(\delta)$ gives:

$$I(\tilde{\nu}) = \text{constant} \int_0^\infty I(\delta) \cos(2\pi\tilde{\nu}\delta)d\delta \qquad (3.2)$$

which allows the determination of intensities at different wavenumbers. To improve the signal-to-noise (S/N) level of a spectrum, multiple interferograms are often recorded and averaged. Equation 3.1 shows that *in theory*, infinitely high resolution can be achieved as $d\tilde{\nu} \to 0$ while Equation 3.2 shows that in order to do so, one must record the interferogram at an infinitely long optical path difference where $\delta \to \infty$, which is *impractical*. Therefore, the interferogram is effectively truncated at the maximum optical path difference $d_{MOPD}=2L$ (twice the farthest distance that the movable mirror M_1 can travel from the point at which both mirrors M_1 and M_2 are equidistant from the beamsplitter) by multiplying by a box-car function:

$$D(\delta) = 1 \qquad \text{if} \qquad -L < \delta < +L \qquad (3.3)$$

$$D(\delta) = 0 \qquad \text{if} \qquad \delta < -L \quad \text{or} \quad \delta > +L \qquad (3.4)$$

Equation 3.2 then becomes:

$$I(\tilde{\nu}) = \text{constant} \int_0^\infty I(\delta)D(\delta) \cos(2\pi\tilde{\nu}\delta)d\delta. \qquad (3.5)$$

The convolution theorem states that the Fourier transform of the product of two functions is equal to the product of the Fourier transform of individual functions. [3] Consequently, an *instrumental line function* $f(\tilde{\nu})$ is generated as the Fourier transform of the truncation function $D(\delta)$ in Equation 3.5:

$$f(\tilde{v}) = 2\, d_{MOPD}\, \frac{\sin(2\pi\tilde{v}d_{MOPD})}{2\pi\tilde{v}d_{MOPD}}. \tag{3.6}$$

which shows that, instead of having an infinitesimally narrow spike at an infinitely long optical path difference, the line width of the spectrum is limited to a *finite* value by the full-width-at-half-maximum (FWHM) of $f(\tilde{v})$ (shown in Figure 3.2) in the form of:

$$\text{FWHM} = \frac{0.605}{d_{MOPD}} \tag{3.7}$$

This FWHM value of the instrumental line function is often referred to as the unapodized resolution of a FTIR spectrometer. For example, the Bruker IFS 125 HR FTIR instrument at the CLS with a d_{MOPD} of 9.4 meters has a value of 0.00064 cm^{-1}. The actual resolution may be Doppler limited as molecules move at different velocities relative to the detector at room temperature. The Doppler line width Δv can be expressed as:

$$\Delta v = \frac{v}{c}\left(\frac{2kT\ln2}{m}\right)^{\frac{1}{2}} \tag{3.8}$$

where v is the transition frequency, m is the molecular weight and T is the ambient temperature. Generally, for a heavy molecule in the far infrared region, the line width is likely instrument-limited by Equation 3.7 while for a light molecule in the mid infrared region, the Doppler line width given by Equation 3.8 determines the line width.

3.2 "Synchrotron advantage" in high resolution FTIR spectroscopy

Although the history of interferometric FTIR spectroscopy dates back to the late 19th century, the resolution was hindered by the computational resources needed to carry out Fourier transformation. It was not until the 1980s that high spectral resolution (better than 0.04 cm^{-1}) using FTIR spectroscopy was achieved for the first time.[4] The efforts to

Figure 3.2: A plot of the instrumental line function $f\left(\tilde{v}\right) = 2\ d_{MOPD}\ \dfrac{\sin(2\pi\tilde{v}d_{MOPD})}{2\pi\tilde{v}d_{MOPD}}$
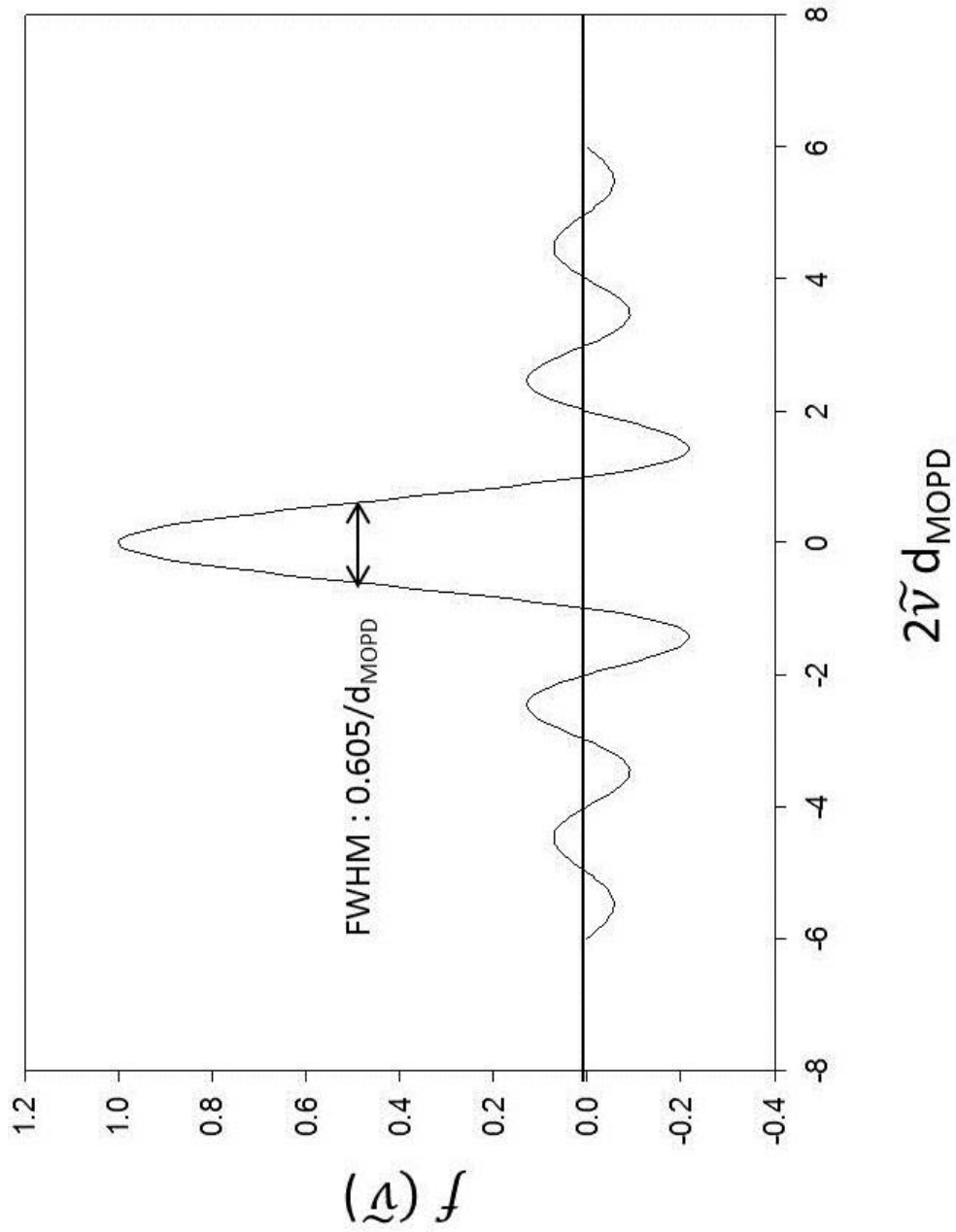
push the resolution to new limits encountered challenges. The optical path differences needed to achieve such high resolution and the circular fringe patterns formed as a result of beam divergence of the infrared source posed problems for the recording of interferograms.[5] In order to obtain a high resolution spectrum, experiments require the aperture of the infrared source to be limited to include only one fringe of the incident beam, sacrificing the infrared flux through the sample and ultimately, the sensitivity. From this point of view, a collimated beam is highly desired to optimize the resolution. As such, high resolution measurements in the far infrared are often difficult for FTIR spectrometers as conventional thermal sources output much smaller infrared flux in this region compared to in the mid and near infrared ranges.[6]

Synchrotron radiation (SR) is an ideal light source for high spectral resolution spectroscopy in the far infrared region as it offers three orders of magnitude greater brightness [7] (defined by the photon flux allowed through a narrow aperture) than conventional light sources, ensuring high sensitivity when a narrow aperture is required. It should also be noted that the synchrotron advantage (SA) over conventional sources is limited by source noise and mechanical vibrations in the transporting optical systems.[8] As a result, the actual magnitude of SA is not as great as the theoretical values predict but still offers significant improvement in sensitivity. At the CLS, the SA is most pronounced in the 300-800 cm^{-1} spectral region with efforts being made to extend this range. A recent study of pyrrole (the current SA benchmark measurement) compared spectra recorded using a globar (which is commonly used as a conventional thermal source in the infrared spectral region) and the CLS synchrotron.[9] With the same number of interferograms, the S/N ratio of the synchrotron spectrum has a factor of eight improvement over the globar

spectrum. That is to say, if the same quality had been obtained by using a globar, it would have taken $8^2 = 64$ times longer acquisition time to compensate for the inferior source brightness.

The concept of coupling synchrotron light with high resolution FTIR spectroscopy was first realised at MAX-lab, Sweden in 1995.[10] The promising results demonstrated the value of this emerging technique in high resolution infrared spectroscopy. Motivated by that, four permanent, dedicated far-infrared synchrotron beamlines including the Canadian Light Source (CLS) located in Saskatoon, Canada have been commissioned in the last five years around the world with more being planned. As the first such beamline to come online in 2007, the CLS currently serves as the only synchrotron-based high resolution FTIR facility in North America. The far infrared beamline at the CLS is equipped with a Bruker IFS 125 HR FTIR spectrometer which is capable of producing infrared spectra at an unapodized resolution of 0.00064 cm^{-1}. There are also suitable multi-pass gas cells at CLS offering up to 72 m absorption path length. This allows absorption spectra to be recorded at low sample pressures without sacrificing resolution due to pressure broadening.

3.3 General procedures to record and analyze rotationally-resolved vibrational spectra

3.3.1 Theoretical considerations

In general, rovibrational spectra originate from motions in which molecules rotate and vibrate at the same time. A transition occurs when the molecules absorbs infrared radiation that corresponds to the energy difference between a specific rotational energy

level in a specific vibrational state and that of a specific rotational energy level in a different vibrational state. Thousands of rovibrational transitions are often observed arising from the large range of populated rotational energy levels in the vibrational ground state at room temperature. From the Born-Oppenheimer approximation, the rovibrational Hamiltonian can be approximated by combining the rotational and vibrational Hamiltonian as:

$$\hat{H}_{rovib} = \hat{H}_{vib} + \hat{H}_{rot} \tag{3.9}$$

The vibrational energy E_{vib} can be estimated from the harmonic oscillator (vibrational) Hamiltonian while the rotational energy E_{rot} can be estimated from the rigid-rotor (rotational) Hamiltonian. However, as discussed in Section 2.4.1.1, no analytical solution can be obtained for the Schrödinger equation for asymmetric tops. Consequently, Pickett's SPFIT/SPCAT program [11] which includes the rovibrational Hamiltonian models of Watson,[12, 13] as well as terms for various interactions was used in fitting and predicting rovibrational spectra in this thesis.

3.3.1.1 Rovibrational symmetry and selection rules

An infrared active vibrational mode requires a changing dipole moment during the vibration. The intensity of a vibrational transition is dictated by the transition moment integral:

$$M_{v'v''} = \int \psi^*(v') \hat{\mu}\, \psi(v'')d\tau \tag{3.10}$$

where v' and v'' are the quantum labels of the lower and higher states involved in the transition, respectively, $\hat{\mu}$ is the dipole moment operator and ψ is the wavefunction of the states. From group theory, a non-zero transition moment integral occurs if the product of

irreducible representations $\Gamma_{v'} \times \Gamma_{\hat{\mu}} \times \Gamma_{v''}$ contains the totally symmetric representation. For example, for a molecule with C_{2v} symmetry, the product must contain the A_1 (symmetric) irreducible representation for an active infrared mode.

The rovibrational selection rules can be divided into two parts: pure rotational selection rules as discussed in Section 2.4.1.3 and the vibrational selection rule $\Delta v = 1$. Briefly, the selection rules are the same as pure rotational transitions as follows:

1) *a*-type bands:

   $\Delta K_a = 0, \Delta K_c = \pm 1$

2) *b*-type bands.

   $\Delta K_a = \pm 1, \Delta K_c = \pm 1$

3) *c*-type bands.

   $\Delta K_a = \pm 1, \Delta K_c = 0$

with $\Delta J = \pm 1, 0$ and $\Delta v = 1$ for all three types. Rovibrational transitions in the same vibrational mode can be categorized into three branches by their ΔJ values, namely: P ($\Delta J = -1$), Q ($\Delta J = 0$) and R ($\Delta J = 1$) branches.

3.3.1.2 Coriolis interactions

Coriolis perturbations originate from interactions between vibration-rotation energy levels in different vibrational states. The rovibrational Hamiltonian incorporating corrections for this interaction can be expressed as:

$$\hat{H} = \hat{H}_{vib} + \hat{H}_{rot} + \hat{H}_{cor} \tag{3.11}$$

where $\hat{H}_{vib}$ and $\hat{H}_{rot}$ are the vibrational and rotational Hamiltonian, respectively, and :

$$\hat{H}_{cor} = -\frac{p_a J_a}{I_a} - \frac{p_b J_b}{I_b} - \frac{p_c J_c}{I_c} + \frac{p_a}{2I_a} + \frac{p_b}{2I_b} + \frac{p_c}{2I_c} \tag{3.12}$$

where p_x, J_x and I_x are the vibrational angular momentum, total angular momentum and moment of inertia along the specified axes, respectively. The $\hat{H}_{cor}$ term is small compared to the other two terms, therefore can be treated using perturbation theory.[14] As a result, the Hamiltonian matrix $\hat{H}$ in Equation 3.11 has off-diagonal elements due to $\hat{H}_{cor}$. The amount of the perturbation of rovibrational energy levels can then be determined by diagonalization of this matrix. The SPFIT/SPCAT program[11] which has operators of the type shown in Equation 3.12 was used in this thesis to fit and predict rovibrational transitions that experience Coriolis interactions.

Similar to the derivation of the vibrational selection rules, Coriolis interaction selection rules can be deduced by considering which states are coupled by non-zero matrix elements of the Coriolis perturbation operator. Mills[14] derived the selection rules for asymmetric tops as follows:

$$\Gamma_{v'} \times \Gamma_{v''} = \Gamma_{R_x} \tag{3.13}$$

Equation 3.13 can be interpreted such that the *x*-type of Coriolis interaction is said to be permitted by symmetry between two energy levels if the direct product of the irreducible representation of the two gives rotation about the *x*-axis (R_x in character tables) where *x* can be *a*-, *b*- or *c*- axis in the principal axis system. For example, for two vibrations of 3-oxetanone of C_{2v} symmetry with $\Gamma_{v'} = B_1$ and $\Gamma_{v''} = B_2$, the product $\Gamma_{v'} \times \Gamma_{v''} = B_1 \times B_2 = A_2$ is of the same symmetry as Γ_{R_a} which means that v' and v'' can interact via an *a*-type Coriolis term.

The spectroscopic implication of Coriolis interaction between rovibrational levels is that these levels are shifted from predicted energy levels based on an unperturbed Hamiltonian model, causing changes to the frequencies and intensities of the observed transitions. The treatment of perturbed spectra requires the assignment of shifted transitions that are sensitive to the off-diagonal elements of $\hat{H}_{cor}$ so that these parameters can be determined. However, in practice, the implementation of these perturbation terms can be difficult given the sheer number of transitions present in a narrow spectral window.

3.3.2 Spectrum collection and analysis scheme

As getting access to the CLS is a merit-based, competitive process, the proposed investigation must be well-planned beforehand. There are three major aspects to consider when targeting specific vibrational bands of a molecule to measure and analyze:

1) *Scientific considerations*: Bands that have unique spectroscopic features including tunneling doubling, Coriolis interactions, etc. are of particular interest as the subsequent analyses using quantum mechanical models can reveal important

scientific insights into fundamental molecular properties that are not available from conventional techniques.

2) *Spectroscopic considerations:* Strong isolated bands will be analyzed first so that the ground state spectroscopic constants can be improved to aid in the assignment of more complex and perturbed bands later.

3) *Technical considerations*: Proposed bands must fall in the spectral range allowed by the apparatus (beamsplitter, detector, window, etc.) available at CLS and where the synchrotron advantage is greatest. The predictions from *ab initio* calculations combined with prior low resolution studies, if available, offer the estimated frequencies and intensities of bands of interest.

Before devoting time to the lengthy collection process at the CLS, experimental conditions must be optimized to obtain the best S/N ratio. One of the most important contributing factors is the sample pressure which should be maintained at such a value that the maximum absorption is realized in the target spectral region without pressure broadening and while the strongest transitions remain unsaturated. This is often achieved by performing collections of a few low resolution interferograms at various pressures to estimate a suitable pressure at which the high resolution data will be recorded. The choices of detector filters (if available) should also be considered to obtain the highest quality spectrum in the allocated time period.

Analysis of rotation-vibration spectra starts by finding quantum number assignments of regularly spaced spectral patterns in the R and P branches, corresponding to selection rules of $\Delta J = +1$ and -1, respectively. For this, the observed spectrum is compared to a simulated spectrum based on the ground state rotational constants (often

from a previous microwave study) and the estimated vibrational band center (often from a previous low resolution infrared study or *ab initio* calculation). In the case of a congested spectrum in which no patterns can be identified by visual inspection, a Loomis-Wood (LW) plot[15] is constructed to find patterns of the strongest progressions of transitions. On a LW plot, regularly spaced rovibrational transitions are grouped in such a way that those belonging to the same progression (i.e. having common K_a but different J for *a*-type transitions) are arranged in an almost vertical series. *Ground state combination differences* (GSCDs) are then used to confirm new rotational quantum number (J, K_a, K_c) assignments. GSCDs are calculated as the energy difference between a pair of transitions (one from the P branch and one from the R branch) that share the same upper state as illustrated in Figure 3.3, and this provides an indirect determination of the energy gaps in the lower (ground) state which are typically well-characterized in advance from microwave experiments.

The preliminarily assigned transitions are fitted using an appropriate Hamiltonian in the SPFIT program[11] to provide more accurate ground state constants and estimate an initial set of upper state parameters. Improved simulated spectra are generated in an iterative fashion until the quantum number assignments of the strongest transitions in the spectrum are known to high values of J, K_a and K_c. A global analysis will yield a set of accurately determined spectroscopic constants that are consistent across the ground state and multiple vibrationally excited states. When Coriolis and Fermi interactions are encountered, the ground state spectroscopic constants must be separately determined from fitting the ground state combination differences to remove any residual effects from the perturbed upper vibrational states. Terms to account for the perturbation can then be included in the Hamiltonian in the SPFIT program to improve the model and account for

both perturbed and unperturbed transitions. While collecting data for one band typically takes several hours or days, a full spectral analysis may take months or years depending on the complexity.

Figure 3.3: A schematic of ground state combination differences (GSCD) for a typical c-type band. A pair of rovibrational transitions from the P ($J+1$, K_a+1, K_c, $v=0 \rightarrow J+1$, K_a, K_c, $v=1$) and R ($J-1$, K_a-1, K_c, $v=0 \rightarrow J+1$, K_a, K_c, $v=1$) branches share a common upper state (J, K_a, K_c, $v=1$). The difference between these two infrared transitions (indicated as ΔE) yields the energy gap of the lower rotational states within the ground vibrational state ($v=0$).

Excited state v=1

Ground state v=0

J, K_a , K_c

R (J-1)

$J-1, K_a-1, K_c$

P (J+1)

$J+1, K_a+1, K_c$

$\Delta E=GSCD$

54
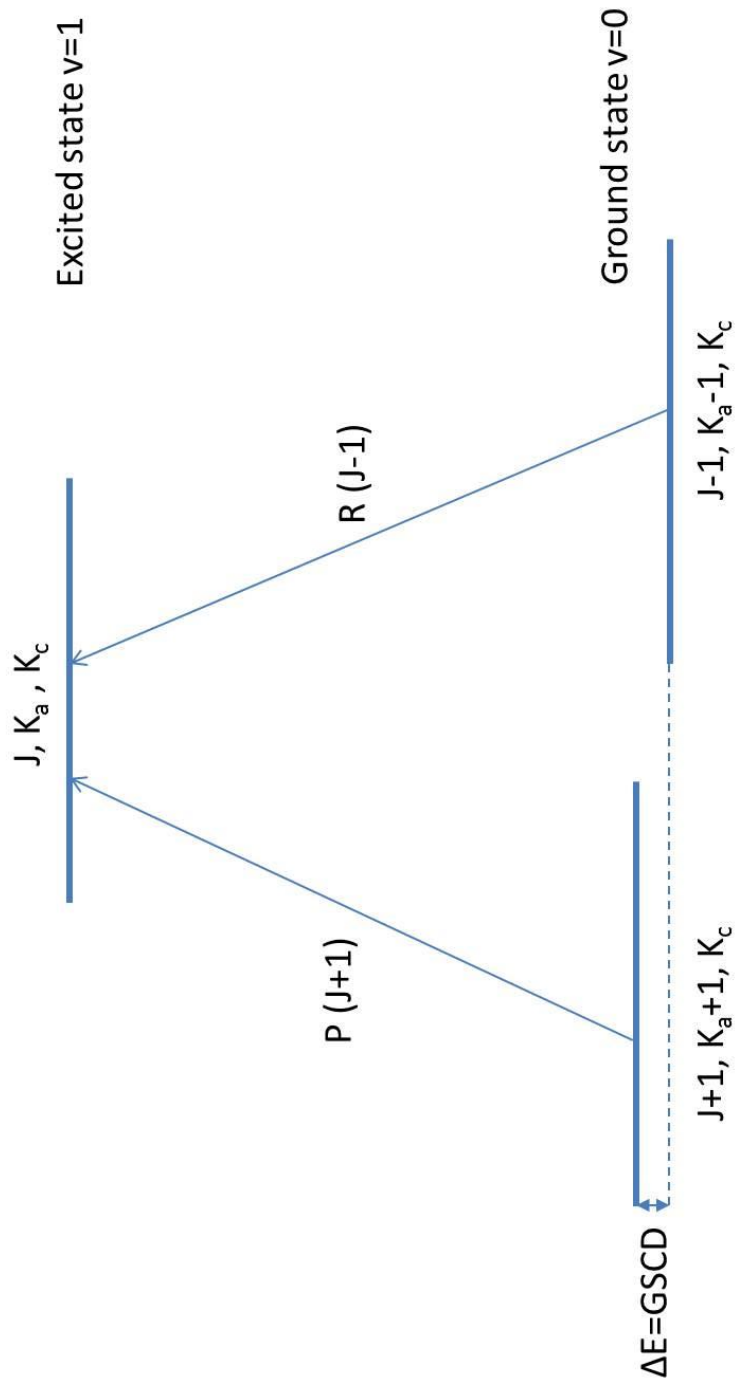
References

[1] A. A. Michelson, *Phil. Mag. Ser.* 31 (1891) 256-259.

[2] A. A. Michelson, *Phil. Mag. Ser.* 34 (1891) 250-255.

[3] R. Bracewell, *The Fourier Transform and its Applications*, McGraw-Hill, New York (1965).

[4] S. Albert, K. K. Albert and M. Quack, *High-Resolution Fourier Transform Infrared Spectroscopy. Handbook of High-Resolution Spectroscopy*, John Wiley & Sons (2001).

[5] P. R. Griffiths, *Chemical Infrared Fourier Transform Spectroscopy,* John Wiley & Sons, New York (1975)

[6] P. R. Griffiths and C. C. Homes, *Instrumentation for Far-infrared Spectroscopy. Handbook of Vibrational Spectroscopy*, John Wiley & Sons (2006).

[7] G. P. Williams, *Synchrotron and Free Electron Laser Sources of Infrared Radiation. Handbook of Vibrational Spectroscopy*, John Wiley & Sons (2006).

[8] A. R. W. McKellar, *J. Mol. Spectrosc*. 262 (2010) 1-10.

[9] D. W. Tokaryk and J. van Wijngaarden, *Can. J. Phys.* 87 (2009) 443-448.

[10] B. Nelander, *Vib.Spectrosc*. 9 (1995) 29-41.

[11] H. M. Pickett, *J. Mol. Spectrosc*. 148 (1991) 371-337.

[12] J. K. G. Watson, *J. Chem. Phys.* 45 (1966) 1360-1361.

[13] J. K. G. Watson, *J. Chem. Phys.* 46 (1967) 1935-1949.

[14] I. M. Mills, *Pure Appl. Chem*. 11 (1965) 325-344.

[15] Neese, C. F. Loomis-Wood Add-In (LWA) for Igor Pro, Version 2.0; 56th Ohio State University International Symposium on Molecular Spectroscopy, Columbus, OH, June 20−24, 2005, http:// fermi.uchicago.edu/freeware/LoomisWood.shtml.

Chapter 4

A high resolution study of the pure rotational and rovibrational spectra of β-propiolactone[a]

4.1 Introduction

As part of efforts to characterize potential energy profiles of four-membered heterocycles, β-propiolactone (2-oxetanone) (c-$C_3H_4O_2$) has been the subject of numerous spectroscopic studies for many years. Its structure was established based on results from electron diffraction[1] experiments and microwave spectroscopy,[2,3] showing that all five heavy atoms are coplanar in a strained ring. Durig conducted a comprehensive vibrational study of all 21 fundamental bands of β-propiolactone in the liquid and gas phase using a combination of infrared and Raman spectroscopy at low resolution.[4] However, *ab initio* calculations[5,6] of the vibrational frequencies of β-propiolactone showed poor agreement with experimental results with some vibrational band frequencies off by up to 85 cm^{-1}.[6]

As the early microwave[2,3] and infrared[4] studies of β-propiolactone were only conducted at low resolution, the current work using the high resolution techniques as described in Chapters 2 and 3 was carried out to obtain a better understanding of five low frequency vibrations with broad coverage of energy levels. This chapter describes the first high resolution microwave and infrared spectra of five bands of β-propiolactone. The pure rotational spectrum was recorded using Fourier transform microwave (FTMW)

spectroscopy in a supersonic jet. The resultant ground state spectroscopic constants provided a basis for the subsequent analysis of the rotationally resolved vibrational spectra in the far infrared region. The five vibrational bands including the ν_{13} (C=O deformation in-plane), ν_{20} (C=O deformation out-of-plane), ν_{19} (α-CH$_2$ rocking), ν_{12} (ring deformation) and ν_8 (C=O ring stretching) modes were studied under high resolution for the first time. The accurately determined band centers were also compared with computational results from DFT calculations of harmonic and anharmonic vibrational frequencies of β-propiolactone. The band origins of the ν_{13} and ν_{20} bands were used to correct the previous misassignment of these two bands from the low resolution study in Ref. [4]. An *a*-type Coriolis interaction between the ν_{13} and ν_{20} bands was observed and included in the quantum mechanical analysis. The ground state spectroscopic constants were refined using the pure rotational transitions complemented with the ground state combination differences calculated from pairs of assigned rovibrational transitions.

4.2 Experimental details

The pure rotational spectrum of β-propiolactone was recorded using the Balle-Flygare type pulsed-jet Fourier transform microwave (FTMW) spectrometer described in Chapter 2. Neon gas was flowed continuously over a liquid sample of β-propiolactone (90%, Sigma-Aldrich) to make a gas mixture. The backing pressure of the gas mixture was maintained at *ca*. 2 atm and the liquid temperature was kept at ~ 45°C using an oil bath. With this sample preparation scheme, 19 pure rotational transitions of β-propiolactone were observed.

The rovibrational spectra of β-propiolactone were collected using the far infrared beamline at the Canadian Light Source (CLS) as described in Chapter 3. The low pressure gas sample was prepared by introducing vapour pressure from a liquid sample (90%, Sigma-Aldrich) to a multipass gas cell which was set to achieve a total pathlength of 72 m. A KBr beamsplitter and a GeCu detector were used in the required spectral range of 400-1200 cm^{-1} for data acquisition of the five bands. Key parameters of the experimental setup and the number of interferograms recorded for each individual band are summarized in Table 4.1. Sample interferograms were recorded, averaged and Fourier transformed. Background interferograms were taken at lower resolution (0.01536 cm^{-1}), averaged and Fourier transformed with zero filling before the final spectrum was calculated. Out of the five bands collected in this particular spectral region, only transitions in the highest frequency band ν_8 at ~1095 cm^{-1} were found to be Doppler broadened. To save time, this band was recorded at lower resolution than the instrument's maximum value. Calibration of the recorded transitions was performed using lines of two molecules (H_2O transitions from 470 to 525 cm^{-1}; N_2O transitions in the 550-630 cm^{-1} and 1130-1210 cm^{-1} regions) by comparison with those found in the HITRAN database.[7]

Table 4.1: Experimental parameters of recorded bands of β-propiolactone.

	ν_{13}	ν_{20}	ν_{12}	ν_{19}	ν_8
Band origin (cm^{-1})	491.0	512.3	747.2	791.3	1095.4
Pressure (mTorr)	44				3
No. of interferograms collected	215				400
Time spent to record interferograms (h)	22				42
Resolution (cm^{-1})	0.000959				0.001918[a]
Lines used in calibration	H$_2$O 470-525 cm^{-1}				N$_2$O
	N$_2$O 550-630 cm^{-1}				1130-1210 cm^{-1}

4.3 Frequency calculations

As there were no prior high level *ab initio* calculations available for β-propiolactone, a harmonic vibrational frequency calculation of β-propiolactone was performed using Gaussian 03W[8] at the B3LYP level with a basis set of 6-311++G (2d,3p) following a geometry optimization. Anharmonic corrections[9, 10] to those frequencies were calculated via second order perturbation theory in Gaussian 03W.[8] Additionally, an empirical scaling factor of 0.9679 was used to adjust the harmonic vibrational frequencies at B3LYP/6-311++G (2d, 3p) for comparison purposes.[11]

---

[a] Resolution was reduced for the ν_8 band as at 1095 cm^{-1} the line width is dominated by Doppler broadening.

4.4 Spectral assignment and analysis

Initially, the observed pure rotational transitions and rovibrational transitions in the five vibrational bands of β-propiolactone were assigned and fit separately. Eventually, transitions from all five vibrationally excited states sharing the same ground state were fit simultaneously in a global analysis using Watson's A-reduced Hamiltonian in I^r representation in Pickett's SPFIT program[12] to obtain a complete set of spectroscopic constants. The assignment and analysis of the pure rotational spectrum and rovibrational spectra of the individual modes are detailed below.

4.4.1 Pure rotational spectrum

The structural determination from the early low resolution microwave study[3] supports a coplanar skeleton of the β-propiolactone backbone with all five heavy atoms in the same plane. Figure 4.1 shows the ground state structure of the β-propiolactone in its principal inertial axis system. As an asymmetric rotor with C_s symmetry, its permanent dipole moment components are along the *a*-axis (μ_a= 3.67 D) and *b*-axis (μ_b= 1.99 D) which allow rotational transitions obeying both *a*- and *b*- type selection rules in the microwave region. Guided by the rotational constants determined in the previous low resolution microwave work,[3] a set of 19 pure rotational transitions of β-propiolactone were measured in the range of 7-21 GHz using the FTMW spectrometer. Table 4.2 lists the assigned transitions including six *a*-type and 13 *b*-type lines, some of which were observed for the first time. These microwave transitions were fit using Watson's A-reduced Hamiltonian in I^r representation in Pickett's SPFIT program,[12] the resulting rotational and centrifugal distortion constants are given in Table 4.3.

Figure 4.1: Structure of β-propiolactone in its principal axis system.
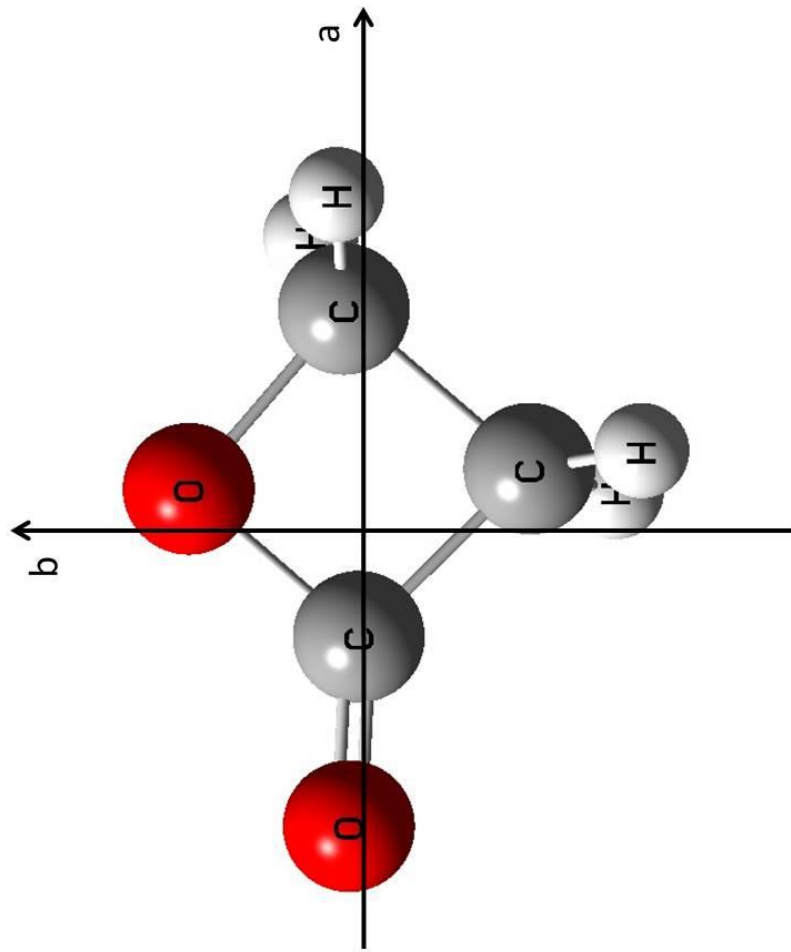
Table 4.2: Observed pure rotational transitions of β-propiolactone in MHz.

$J'_{K'_a K'_c}$	→	$J''_{K''_a K''_c}$	ν_{obs}	$\nu_{obs\text{-}cal}$
1_{01}	→	0_{00}	9113.6497	-0.0010
1_{11}	→	0_{00}	16275.1813	-0.0004
1_{10}	→	1_{01}	8536.7871	0.0016
2_{02}	→	1_{01}	18047.5972	0.0002
2_{02}	→	1_{11}	10886.0671	0.0011
2_{11}	→	1_{10}	19602.5191	-0.0010
2_{12}	→	1_{11}	16852.0194	-0.0004
2_{11}	→	2_{02}	10091.7094	0.0009
4_{13}	→	4_{04}	16714.7804	0.0001
3_{03}	→	2_{12}	20675.6502	0.0007
3_{21}	→	3_{12}	20421.1771	0.0001
4_{22}	→	4_{13}	19574.5732	-0.0003
5_{23}	→	5_{14}	19607.6468	0.0002
3_{12}	→	3_{13}	8236.6572	-0.0009
2_{20}	→	2_{11}	21664.1879	0.0000
4_{13}	→	4_{14}	13649.6505	0.0004
3_{12}	→	2_{21}	7798.5917	0.0004
3_{12}	→	3_{03}	12733.1958	-0.0003
4_{13}	→	3_{22}	19255.5967	-0.0004

Table 4.3: Ground state spectroscopic constants of β-propiolactone determined by FTMW spectroscopy.

Rotational constants	/MHz		/cm^{-1}
	This work	Ref. [3]	This work
A	12405.9970(5)	12406.01(20)	0.413819510(16)
B	5244.4591(19)	5244.53(20)	0.174936326(6)
C	3869.1943(3)	3869.18(20)	0.129062428(9)
Centrifugal distortion constants	/ kHz		/10^{-6} cm^{-1}
Δ_J	0.668(5)	-	0.0223(2)
Δ_{JK}	3.86 (6)	-	0.129(2)
Δ_K	4.30(9)	-	0.143(3)
δ_j	0.181(3)	-	0.00603(9)
δ_k	2.24(9)	-	0.075(3)
rms error /kHz	0.679		

4.4.2 Infrared spectra of the v_{12}, v_{19} and v_8 bands

The three vibrational bands that were first analyzed correspond to motions involving ring deformation (v_{12}), α-CH$_2$ rock (v_{19}) and C=O ring stretching (v_8). Figure 4.2 shows a portion of the spectrum containing the v_{12} band which exhibits a typical a-type band contour with rotational selection rules (K_aK_c) $eo \leftrightarrow ee$ and $oe \leftrightarrow oo$ as a result of the A′ symmetry. The v_{12} band centered at ~747 cm^{-1} was chosen as the first band to be

Figure 4.2: An overview spectrum showing the *a*-type band structure of the ν_{12} band of β-propiolactone.
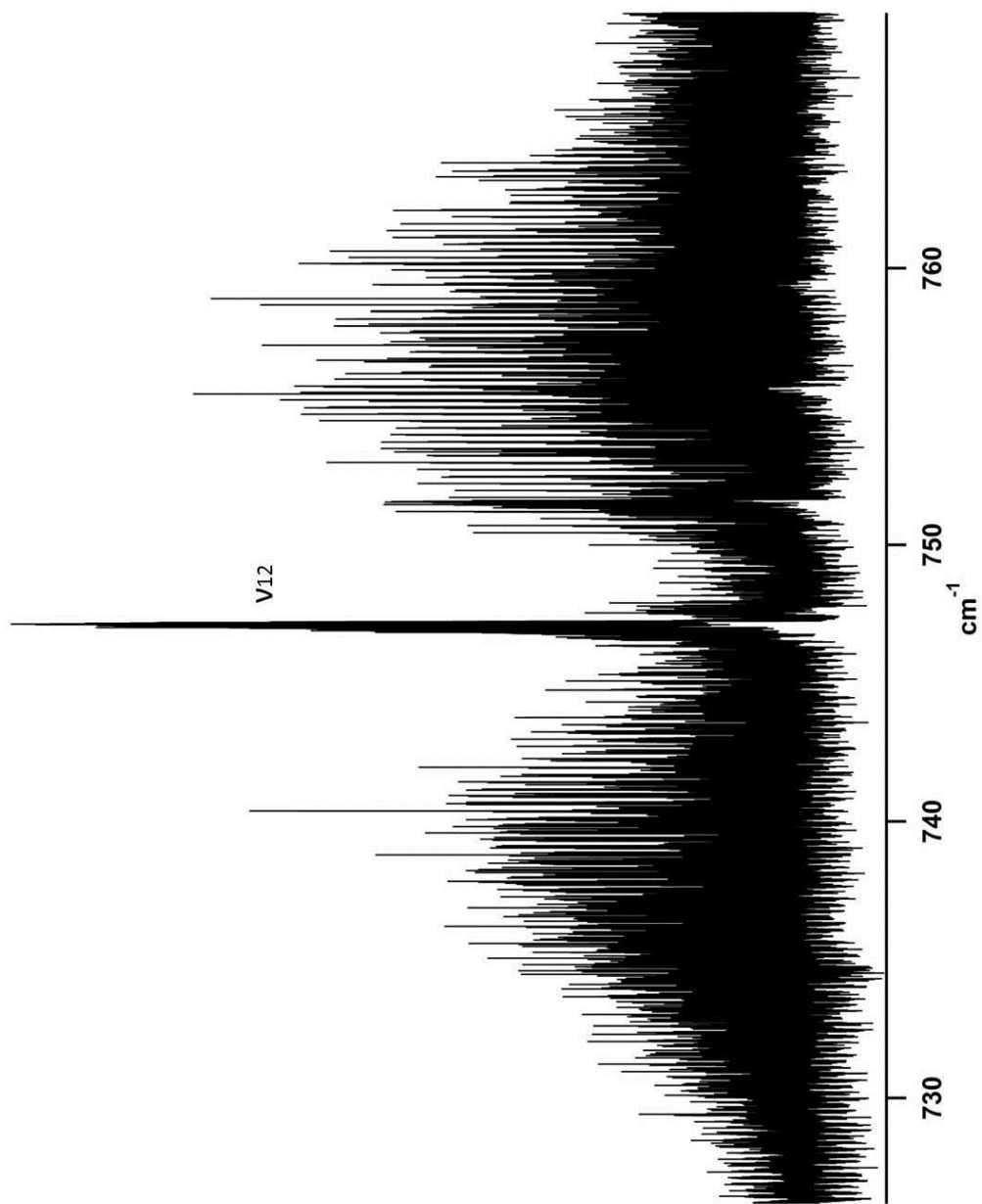
analyzed as: 1) it is separated from other strong absorption features thus less prone to potential interactions with nearby energy levels; 2) a series of regularly spaced spectral patterns were readily identified through preliminary visual inspection even though the rotational structure of this mode is dense as shown in Figure 4.3. A simulated spectrum was generated using the estimated band origin from the previous low resolution infrared study[4] and the rotational constants from the pure rotational spectroscopic study in this work. The first attempt to assign the observed spectrum was based on comparison with the simulated spectrum. The preliminary assignment of those regularly spaced clusters of transitions was verified by using ground state combination differences (GSCDs) based on the rotational constants obtained from the microwave study. The simulated spectrum was refined after the addition of the newly assigned transitions and the process continued in an iterative fashion until the strongest transitions were assigned. In total, 2402 transitions were assigned from the P and R branches up to K_a =18 (J_{max} =68). Another 358 transitions from the Q branch were assigned with K_c values between 0 and 23 with J_{max} = 68. Figure 4.4 shows the progressions of assigned Q branch transitions of the ν_{12} band which have the typical a-type Q branch patterns. All 2760 transitions assigned from the ν_{12} band were fit using Watson's A-reduced Hamiltonian in I^r representation in Pickett's SPFIT program.[12] Although only nine excited state constants (three rotational constants and centrifugal distortion constants plus band origin) were allowed to vary in the individual band analysis, the root-mean-square (rms) error of the fit was only 0.000128 cm^{-1}.

The ν_{19} band attributed to the α-CH_2 rocking motion has A″ symmetry and obeys c-type selection rules $oe \leftrightarrow ee$ and $eo \leftrightarrow oo$. By following the above mentioned procedure,

Figure 4.3: A section of the R branch of the ν_{12} band of β-propiolactone showing the rotational structure. The strongest transitions of two adjacent progressions are labelled with quantum numbers $J'_{K'_a K'_c} - J''_{K''_a K''_c}$. Only select transitions are labelled here for simplicity.

67
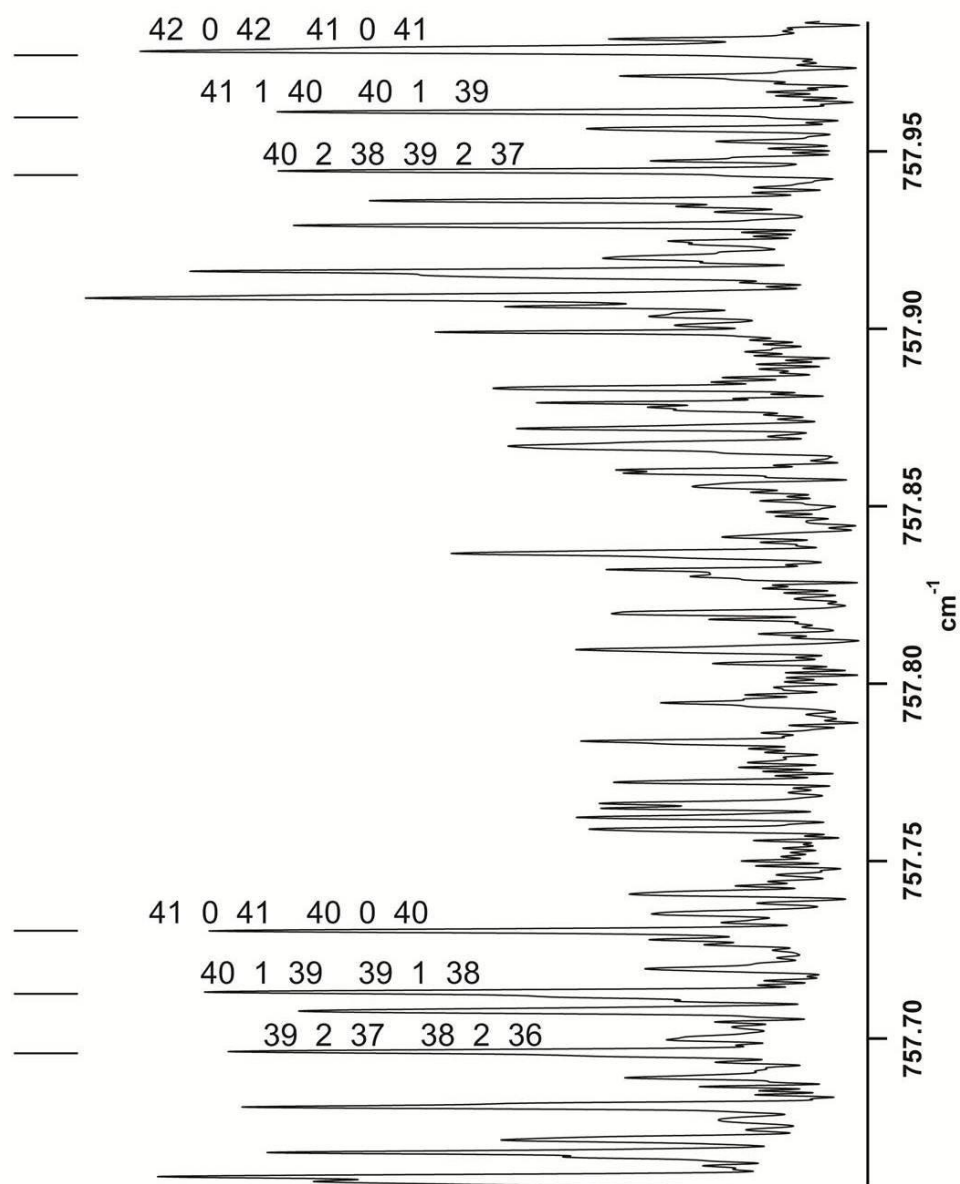
Figure 4.4: A narrow spectral window of ~0.04 cm^{-1} showing details of the Q branch of the ν_{12} band of β-propiolactone. Only select transitions are labelled with quantum numbers $J'_{K'_a K'_c} - J''_{K''_a K''_c}$ here for simplicity.
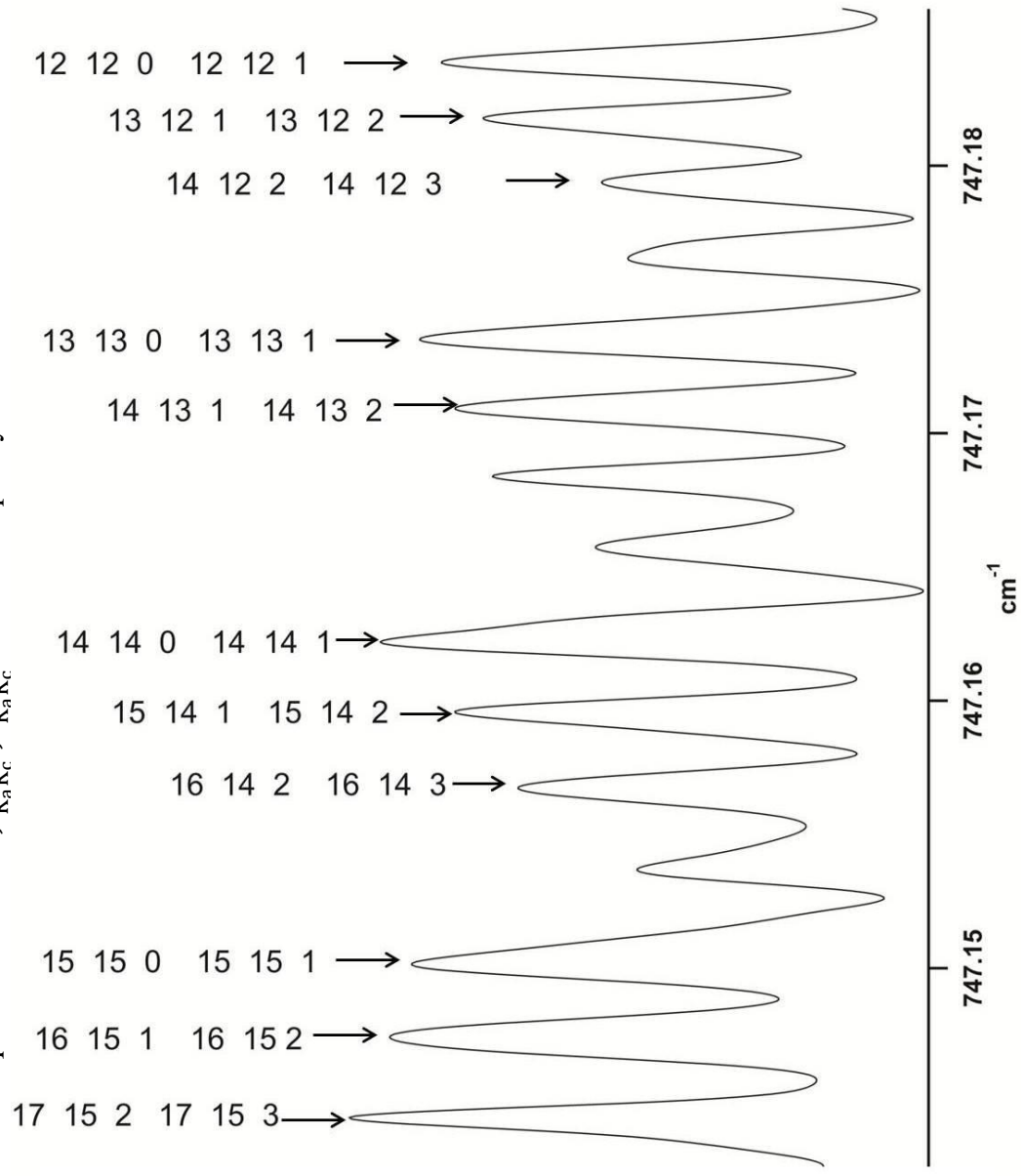
a total of 2590 transitions were assigned including 350 Q branch lines. In the P and R branches, progressions from J $=5$ to 45 with K_c ranging from 1 to 42 were assigned. For the Q branch, transitions with $J_{max} =52$ and K_c between 0 and 31 were assigned. The assigned transitions were fit as described above for the ν_{12} band and the overall rms error was 0.000126 cm^{-1} for this isolated band analysis.

The ν_8 C=O ring stretching mode at 1095 cm^{-1} has A$'$ symmetry and the observed spectrum clearly shows a characteristic b-type contour with the absence of a sharp center branch (Q) as shown in Figure 4.5. The rotational selection rules of a b-type band are $eo\leftrightarrow oe$ and $ee\leftrightarrow oo$. As the Q branch transitions now heavily blend with those from the P and R branches, the spectrum is denser than the other two bands (a-/c-type) discussed above. For this reason, the assignment of the ν_8 band presented extra difficulties. To circumvent this issue, the preliminary assignment was started in a spectral region further away from the band center where the Q branch transitions are substantially weaker. Extra care was taken to ensure that the quantum number assignment was correct for the first few transitions in this dense rotational structure using GSCDs. Overall, 1651 transitions were assigned for the ν_8 band including 726 from the Q branch. In the P and R branches, energy levels ranging from J=3 to 46 with K_a (max) $=22$ were covered. Progressions from $K_c = 0$ to 44 with J (max) = 53 in the Q branch were assigned. Those assigned transitions were fit using the same method mentioned above and the overall rms error was 0.000205 cm^{-1} for the analysis of the ν_8 band.

Figure 4.5: An overview spectrum showing the *b*-type band structure of the ν_8 band of β-propiolactone at ~1093 cm^{-1}.
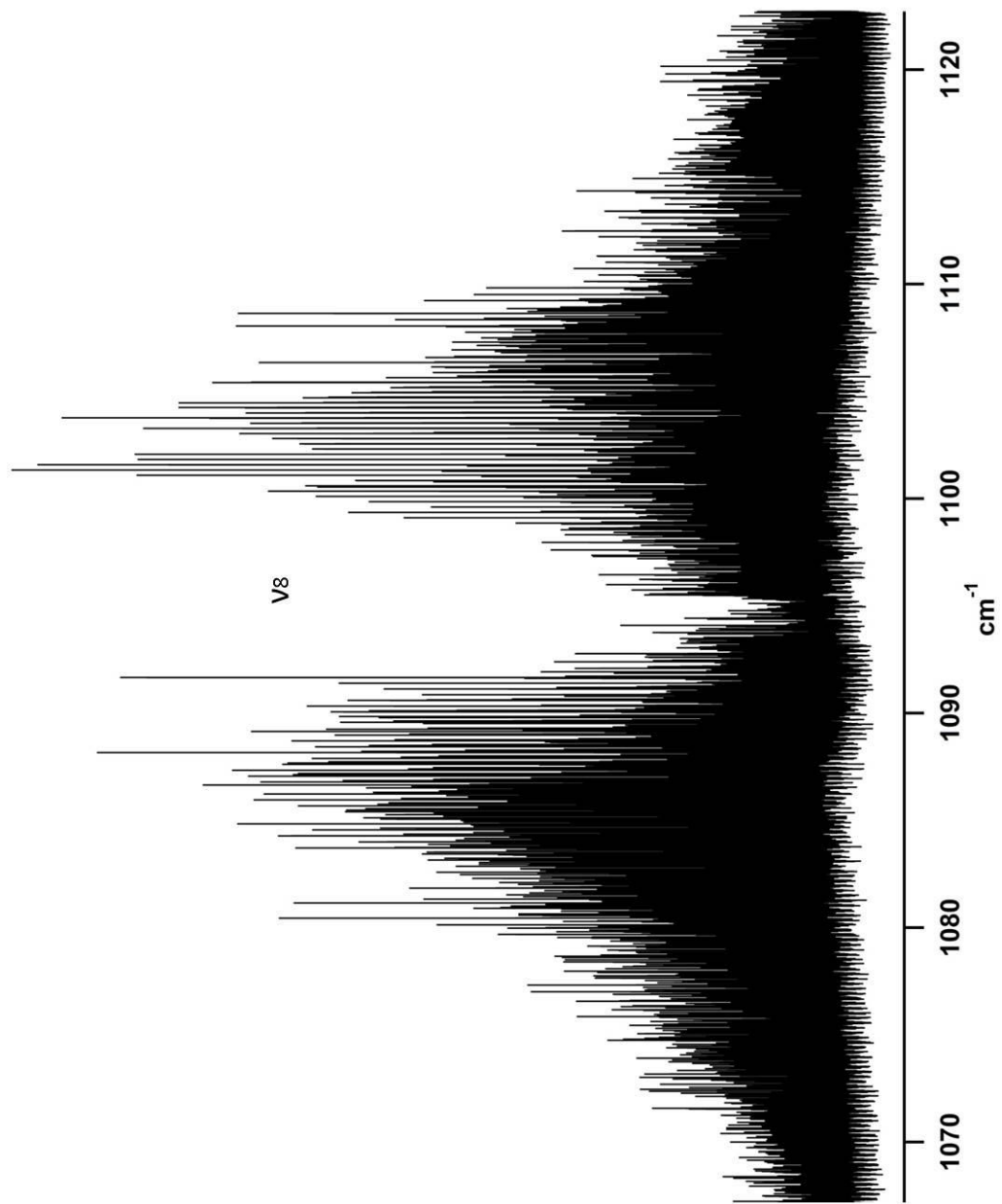
4.4.3 Infrared spectra of the ν_{13} and ν_{20} bands

4.4.3.1 Initial analysis of the ν_{13} and ν_{20} bands

An overview of the high resolution vibrational spectrum containing the two C=O deformation vibrational motions of β-propiolactone between 450-550 cm^{-1} is shown in Figure 4.6. In the early low resolution infrared study,[4] the lower band at 491 cm^{-1} was attributed to c-type selection rules and the higher band at 513 cm^{-1} to a-type selection rules based on the unresolved band contours identified at that time. As a consequence, the author assigned the lower band to the ν_{20} C=O deformation out-of-plane mode and the higher band to ν_{13} C=O deformation in-plane mode (referring to the motion of the carbonyl group relative to the ring). This is inconsistent with our high resolution spectrum shown in Figure 4.6 which clearly indicates the reverse assignment: a typical a-type band contour at 491 cm^{-1} and a characteristic c-type band contour with its sharp Q branch at 513 cm^{-1}. Thus, the lower band at 491 cm^{-1} is now correctly assigned to the ν_{13} C=O deformation in-plane mode with A′ symmetry and the higher band at 513 cm^{-1} to the ν_{20} C=O deformation out-of-plane mode with A″ symmetry based on the unambiguous assignment of rotational structure in the current study. This assignment is supported by DFT calculations in the present work.

As shown in Figure 4.6, the R branch of the lower frequency ν_{13} band significantly overlaps with the P branch of the higher frequency ν_{20} band. This highly congested region adds more complexities to the spectral analysis as the preliminary assignment relies on the observation of recurring patterns. To aid in the assignment, Loomis-Wood plots were constructed to identify regularly spaced transitions using the Loomis-Wood add-in

Figure 4.6: An overview spectrum showing the a- and c-type band structure of the ν_{13} and ν_{20} bands of β-propiolactone at $\sim$491 cm^{-1} and $\sim$513 cm^{-1}, respectively. Notice that the R branch of the ν_{13} band overlaps the P branch of the ν_{20} band.
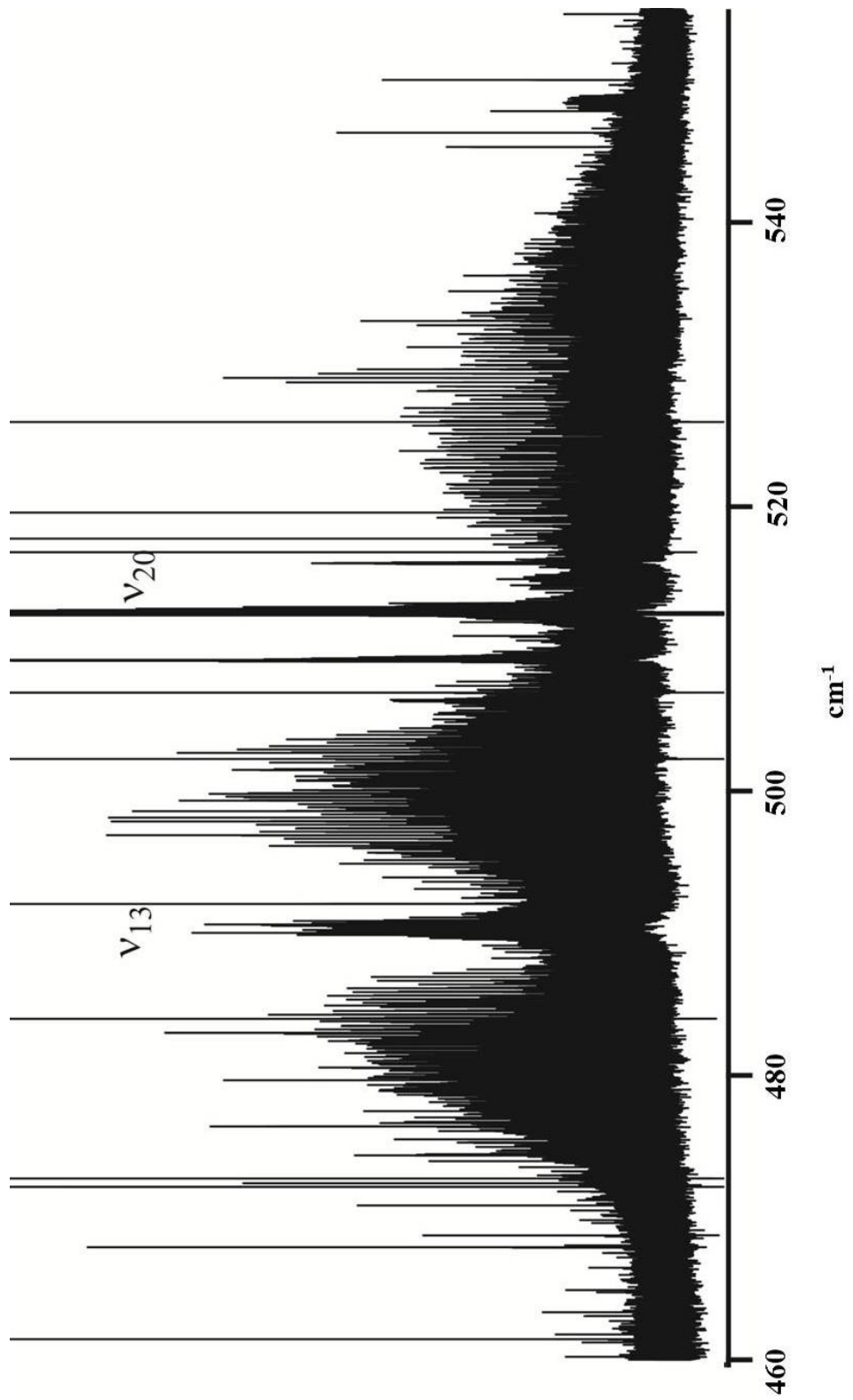
(LWA)[13] to Igor Pro[14] so that the preliminary assignment of P and R branch transitions in both bands could proceed using the method previously described in Chapter 3. A portion of the Loomis-Wood plot is shown in Figure 4.7 where progressions in the R branch of the ν_{20} band (517-534 cm^{-1}) differing in J but sharing common K_c are grouped vertically to stand out. Note that the adjacent transitions in a given cluster of lines, for example, those outlined by the horizontal box in Figure 4.7, arise from quantum number progressions differing by $\Delta K_c = 3$ in this particular band. Figure 4.8 shows the strongest lines assigned in a more tightly clustered small region of the ν_{20} spectrum which correspond to such a progression.

Upon initial inspection of the preliminary assignment of the ν_{13} and ν_{20} bands, some transitions were found to be shifted from their predicted frequencies, causing a larger than expected rms error. More importantly, the resultant spectroscopic constants from the fit did not account for a large number of unassigned transitions. Also, certain centrifugal distortion constants for the excited vibrational states were observed to have opposite signs to those of the ground state of β-propiolactone. These unusual observations were thought to be linked to an interaction between the ν_{13} and ν_{20} bands as they are only separated by 21 cm^{-1}. To properly treat this interaction, a set of ground state spectroscopic constants that are "perturbation free" was needed.

4.4.3.2 Determination of the ground state spectroscopic constants

Both pure rotational and rovibrational transitions from this study and Ref. [3] were used to establish the ground state spectroscopic constants of β-propiolactone. In

Figure 4.7: A portion of the Loomis-Wood plot of the ν_{20} band of β-propiolactone between ~517 and ~534 cm^{-1} showing c-type progressions used to aid in its assignment. The progressions in K_c' (shown vertically in the plot) extend over a large region of the spectrum making adjacent lines within a K_c' series difficult to identify. The plot also identifies the origin of the tight clusters of transitions (shown horizontally in the plot) in certain spectral regions. These groupings involve transitions in which K_c' differs by three but the ordering of lines within each cluster changes along the vertical as the progressions cross. The box near the center of the plot identifies the region of the spectrum corresponding to Figure 4.8 in which there are three clusters of transitions.
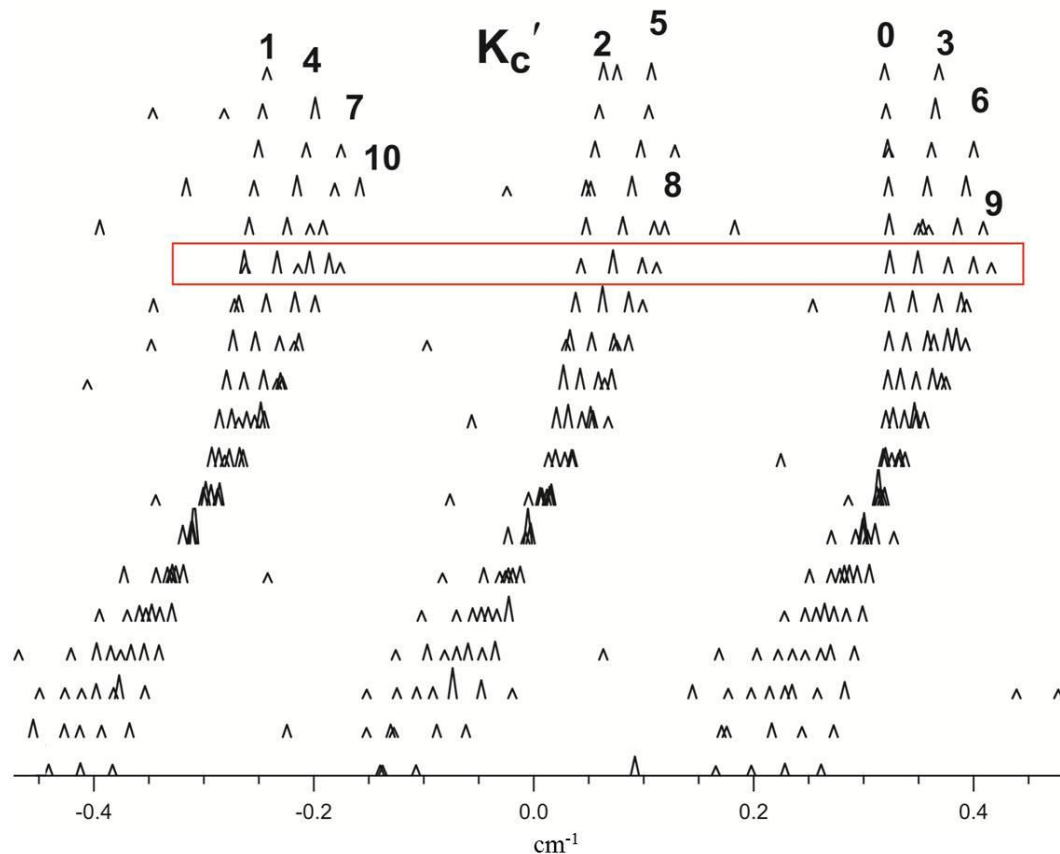
Figure 4.8: The rotational structure of a small region of the R branch of the ν_{20} band of β-propiolactone. The observed clustering of transitions arises from progressions in which K'_a of adjacent transitions changes by one and K'_c changes by 3. The K'_c value of each transition is emphasised by the circles on this spectrum.
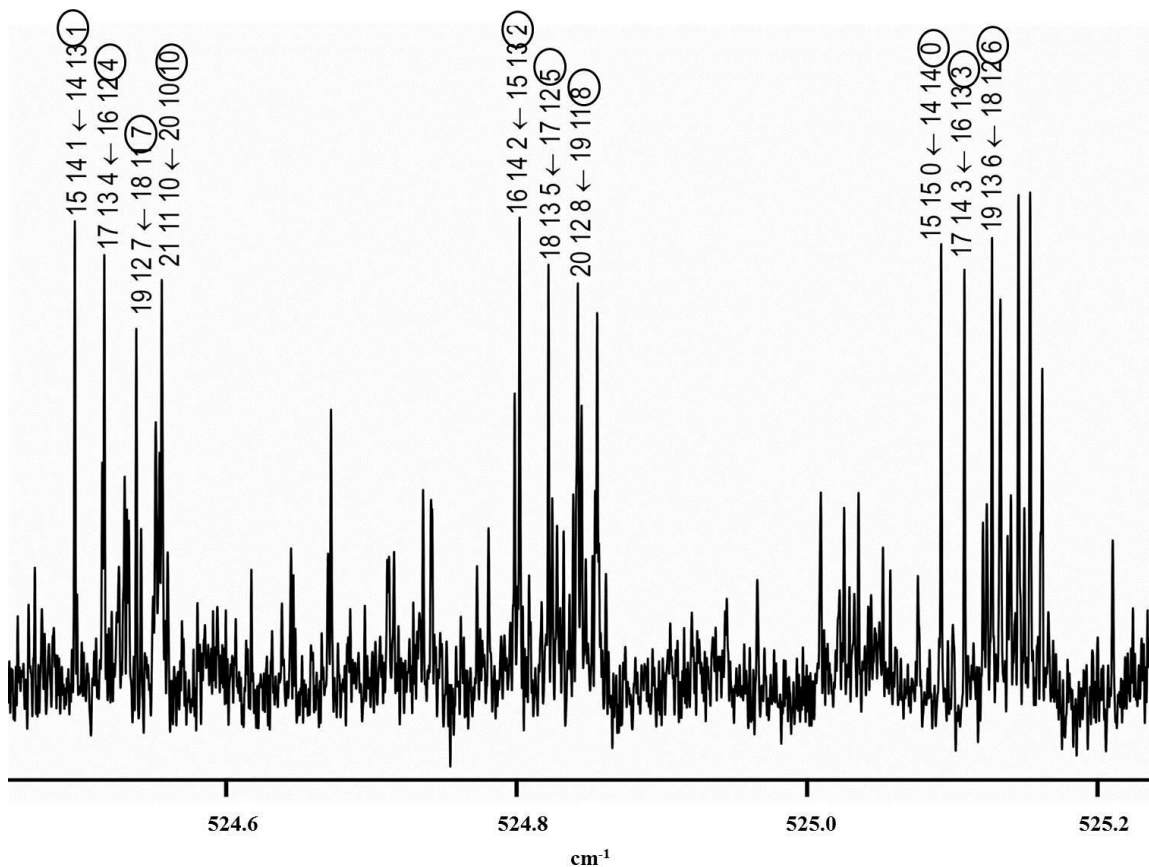
total, 1943 ground state combination differences calculated from 3886 pairs of P and R branches transitions were obtained which share common upper states. These were taken from multiple vibrational bands under study here in order to span a large range of quantum numbers including J from zero to 65. Combined with 19 microwave transitions, a total of 1962 transitions involving only the ground vibrational state were fit using

Watson's A-reduced Hamiltonian in I^r representation in Pickett's SPFIT program.[12] The estimated uncertainty of the pure rotational transitions is weighted 1/1500 that of the infrared data to reflect the greater precision of the microwave measurements. The ground state spectroscopic constants including three rotational constants and five centrifugal distortion constants are reported in Table 4.4. The rms error of the ground state fit was 0.000187 cm^{-1}. These ground state constants were held fixed in the subsequent infrared band analyses to eliminate any effect of perturbed upper states.

4.4.3.3 Perturbation analysis of the ν_{13} and ν_{20} bands

Based on C_s symmetry, the ν_{13} and ν_{20} bands of β-propiolactone have A′ and A″ vibrational symmetries, respectively, allowing these two bands to potentially interact via both a-type and b-type Coriolis couplings.[15] The symmetry-permitted a-type and b-type Coriolis coupling constants were tested in the simultaneous analysis of the ν_{13} and ν_{20} bands and the observed spectra were found to be sensitive to only the a-type interaction parameter G_a. With the incorporation of this perturbation term into the Hamiltonian model, the remaining transitions were consistent with their predicted frequencies and the centrifugal distortion constants of these two excited states matched their ground states counterparts in sign and magnitude. More importantly, the assignment of previously unassigned transitions with low intensity (most of which are those with low K_a values of the c-type ν_{20} band and those with high K_c values of the a-type ν_{13} band) were readily assigned following the inclusion of G_a in the Hamiltonian model.

Table 4.4: Spectroscopic constants for the ground state, v_{13} v_{20}, v_{19}, v_{12} and v_8 states of β-propiolactone determined from rovibrational studies.

	Ground state	v_{13}	v_{20}	v_{12}	v_{19}	v_8
v / cm⁻¹		490.955500 (9)	512.341950 (10)	747.244650(8)	791.343000(10)	1095.433570(10)
Rotational constants / cm⁻¹						
A	0.4138195 10(16)	0.4148370(10)	0.4138080(10)	0.41340521(2)	0.41305227(4)	0.4159858(3)
B	0.174936330(7)	0.17494820(4)	0.17494980(5)	0.1748118(3)	0.17495150 (10)	0.17457870(6)
C	0.129062440(7)	0.128862270(20)	0.12912660(6)	0.128940340(15)	0.12897720(14)	0.12877033(4)
Centrifugal distortion constants / 10⁻⁹ cm⁻¹						
Δ_J	22.70(6)	22.840(10)	22.77(2)	22.600(7)	22.60(7)	21.59(2)
Δ_{JK}	127.9(5)	118.30(7)	140.70(9)	133.69(3)	129.2(4)	162.4(4)
Δ_K	141.0(6)	130.20(9)	163.50(11)	133.36 (2)	137.4(3)	72.0(10)
δ_j	5.77(3)	5.820(6)	5.750(17)	5.836(4)	5.60(5)	5.220(13)
δ_k	77.0(7)	79.30 (10)	79.0(3)	79.00(6)	74.0(12)	65.50(20)
Coriolis interaction parameter / cm⁻¹						
G_a (13,20)	-	0.24171(5)		-	-	-
rms error / cm⁻¹	0.000187			0.000154		-

77

Overall, 3350 transitions were assigned for the c-type ν_{20} band including 760 transitions from the Q branch. For the P and R branches, the quantum numbers of assigned transitions span from J =5 to 40 with K_a (max) =37. In the Q branch, transitions were assigned with K_c covering from zero to 41 with J (max) = 42. For the a-type ν_{13} band, 3067 transitions were assigned including 536 transitions from the Q branch. The spanned quantum numbers of assigned transitions include those in the P and R branches from J = 4 through 62 with K_a (max) = 25. In total, 6417 transitions from the ν_{13} and ν_{20} bands were fit using the Hamiltonian described above including the G_a interaction term. The rms error of this fit was 0.000122 cm^{-1}.

4.4.4 Global analysis

A simultaneous fit consisting of all 13311 assigned rovibrational transitions from the ν_8, ν_{12}, $\nu_{13,}$ ν_{19} and ν_{20} bands was performed in Pickett's SPFIT program using Watson's A-reduced Hamiltonian, I^r representation[12] with the ground state spectroscopic constants held fixed to values determined from the GCSDs and microwave data. The determined spectroscopic parameters including the band origin along with the three rotational constants and five centrifugal distortion constants for each vibrational state plus the Coriolis interaction term G_a between the ν_{13} and ν_{20} states are summarized in Table 4.4. The overall rms error of this global fit was 0.000154 cm^{-1}.

4.5 Discussion

The low resolution vibrational study of β-propiolactone in Ref. [4] provided the estimated band origins, selection rules and intensities which aided the high resolution investigation discussed here. A set of accurately determined spectroscopic constants for the ground state and five low lying vibrational states was established for the first time. The simultaneous fit of 13311 rovibrational transitions yielded an rms error of only 0.000154 cm^{-1} which suggests that the Hamiltonian model employed provided a good description of the bands analyzed in the present work. From the results of this high resolution study, the two overlapping bands, ν_{13} and ν_{20} at ~491 cm^{-1} and ~513 cm^{-1}, respectively, were unambiguously assigned for the first time. This is the opposite of the assignment made in the earlier infrared work by of Durig[4] in which the band contours were obscured by the low resolution spectrum available at that time.

4.5.1 The determination of ground state spectroscopic constants

The pure rotational spectrum of β-propiolactone was recorded for the first time using Fourier transform microwave (FTMW) spectroscopy. Many of the $\nu_{obs-cal}$ residues are within 1 kHz as shown in Table 4.2. The three rotational constants compare reasonably well with those determined in the earlier microwave work as shown in Table 4.3, however, centrifugal distortion constants were not determined in Ref. [3] making strict comparison difficult. The accuracy of the rotational constants were better determined here than in the previous study of β-propiolactone. This played an important role in the subsequent characterization of the rovibrational spectra in the preliminary assignment stage.

On the other hand, the ground state combination differences (GSCDs) obtained from rovibrational transition pairs indirectly offer accurate ground state information over a much broader coverage of energy levels. Compared to the use of a few pure rotational transitions with J (max) = 5 in the microwave study, energy levels up to J = 65 and covering a broad range of K_a and K_c values from *a*-, *b*- and *c*-type transitions in the rovibrational study were included to derive the ground state spectroscopic constants via the GSCDs. This method not only combined the broad energy level coverage of rovibrational GSCDs and the high precision of pure rotational measurements but also removed the upper state dependence to eliminate any perturbation effects. As a consequence, the resulting spectroscopic parameters are well determined and physically meaningful rather than being "effective" constants. As a result of this work, a complete, accurate set of ground state spectroscopic constants has been established and listed in Table 4.4 which can be used for future high resolution studies of β-propiolactone using infrared or electronic spectroscopy. In a more general sense, the protocol developed to characterize the ground state of this prototype molecule can be used in future studies of this type.

4.5.2 The perturbation between the ν_{13} and ν_{20} bands

During the initial assignment of the closely spaced ν_{13} and ν_{20} bands, the rotational constant A and two centrifugal distortion constants Δ_K, δ_k appeared to be effective values as they were not consistent with the analogous ground state parameters as shown in Table 4.5. For instance, both Δ_K and δ_k had opposite signs compared to their ground state counterparts using a typical Hamiltonian model. Furthermore, these effective constants

did not account for many low intensity transitions in these two bands. The inclusion of the G_a parameter brought better consistency with the ground state values although the rotational constant A became less well determined due to the high correlation between G_a and itself. The rms error of the three-state fit was reduced by a factor of 30 when G_a was included in the fit suggesting that this interaction parameter is essential to the model that accounts for the observed spectrum of the ν_{13} and ν_{20} bands. This model also allowed extensive assignment of the remaining low intensity transitions and serves as a useful template for studying vibrational interactions in other molecules. These couplings tend to be important in the far infrared region of the spectrum and are thus critically important for deriving accurate potential energy profiles of molecules.

The value of the first order a-type Coriolis interaction term was determined as G_a = 0.24 cm^{-1}. The positive sign of G_a indicates a positive perturbation between these two vibrations, in which the R branch of the lower frequency vibrational band (ν_{13}) and the P branch of the higher frequency band (ν_{20}) gain intensity from the depleted P branch of the lower frequency band and the R branch of the higher frequency vibration. Classically, this occurs when two excited perpendicular motions (in this case the ν_{13} in-plane and ν_{20} out-of-plane C=O deformation motions) are enhanced by the rotation of the molecule producing Coriolis forces in the same sense as the vibrational angular momentum of the adjacent mode.[15]

Table 4.5: Subset of spectroscopic parameters (cm^{-1}) that illustrate the effect of including and excluding the a-type Coriolis interaction term between the v_{13} and v_{20} states of β-propiolactone with fitting transitions from these two bands only.

	Ground state	Without perturbation treatment		With perturbation treatment	
		v_{13}	v_{20}	v_{13}	v_{20}
A	0.413819510(16)	0.4121168(16)	0.4165205(11)	0.4148370(10)	0.4138080(10)
$10^9 \times \Delta_K$	141.0(6)	-73.9(2)	302.9 (2)	130.20(9)	163.50(11)
$10^9 \times \delta_k$	77.0(7)	-68.1(2)	207 (8)	79.30 (10)	79.0(3)
G_a	-	-		0.24171(5)	
rms error		0.004184		0.000122	

82

4.5.3 Determination of vibrational frequency

In this study, the band origins of the v_{13} (490.955500(9) cm^{-1}), v_{20} (512.341950(9) cm^{-1}), v_{12} (747.244650(8) cm^{-1}), v_{19} (791.34300(1) cm^{-1}) and v_8 (1095.43357(1) cm^{-1}) bands were accurately determined for the first time and compare well with the gas phase low resolution infrared results from Durig (490 cm^{-1}, 513 cm^{-1}, 746 cm^{-1}, 790 cm^{-1}, and 1093 cm^{-1}).[4] The only exception was the misassignment of the low frequency C=O deformation modes pairs (v_{13} and v_{20} bands) in Ref. [4]. It has been shown that the *a*-type band at ~491 cm^{-1} and the *c*-type band at ~513 cm^{-1} are unambiguously assigned to the v_{13} C=O deformation in-plane mode and the v_{20} C=O deformation out-of-plane mode, respectively, via the selections rules governing the rotational structure in this study.

When compared to the scaled *ab initio* harmonic frequencies (MP2/6-31G*) reported by Bordejé et al[6], the experimental values were found to be substantially higher (46 cm^{-1} and 35 cm^{-1} higher for the v_{12} and v_8 bands for example) than the calculations. In pursuit of a computational prediction that has better agreement with the experimental values, new DFT calculations (B3LYP/6-311G++(2d,3p)) of the harmonic, harmonic scaled and anharmonic frequencies were performed for β-propiolactone and the results are shown in Table 4.6. For the v_{12} and v_{19} modes (and many modes identified in Durig's spectrum above 700 cm^{-1}), the anharmonic calculations have frequencies that are accurate to within a few wavenumbers. This superior result over the two harmonic predictions was achieved at a steep computational price, however, as the anharmonic calculations took 40 times longer to complete. Surprisingly, for the v_{20} and v_{13} modes (the lowest two studied here), the harmonic calculation gives predictions within ~1 cm^{-1} of the observed

Table 4.6: Comparison of the experimentally observed infrared frequencies in cm^{-1} with computational predictions (B3LYP/6-311++G(2d,3p)). Bands studied in this work are highlighted in bold.

Expt (Ref. [4])	Calc. harmonic	Calc. harmonic scaled[a]	Calc. anharmonic	Normal mode	Symmetry
3001	3136	3036	2990	α, β-CH$_2$ antisym str	A'
2935	3085	2986	2971	α, β-CH$_2$ sym str	A'
1882	1901	1840	1871	C=O str	A'
	1525	1476	1531	β-CH$_2$ def	A'
1427	1461	1415	1442	α-CH$_2$ def	A'
1319	1343	1300	1309	β-CH$_2$ wag	A'
1199	1227	1188	1201	α-CH$_2$ wag	A'
ν$_8$ 1093	**1104[b]**	**1069**	**1075**	**CO ring str**	**A'**
	1010	978	988	CC ring str	A'
924	930	900	902	CO ring str	A'
891	887	859	864	Ring def	A'
ν$_{12}$ 746	**751**	**727**	**745[b]**	**Ring def**	**A'**
ν$_{13}$ 490	**489[b]**	**474**	**486**	**[c]C=O def in-plane**	**A'**
3028	3152	3051	3004	α, β-CH$_2$ antisym str	A''
3000	3093	2994	2996	α, β-CH$_2$ antisym str	A''
	1205	1167	1180	α-CH$_2$ twist	A''
1139	1157	1120	1132	β-CH$_2$ twist	A''
1046	1046	1012	1046	α-CH$_2$ rock	A''
ν$_{19}$ 790	**805**	**779**	**797[b]**	**β-CH$_2$ rock**	**A''**
ν$_{20}$ 513	**513[b]**	**497**	**522**	**[c]C=O def out-of-plane**	**A''**
113[d]	188	182	190	Ring puckering	A''

[a] Scaled with a factor of 0.9679 from Ref. [11].
[b] The underlined frequency indicates the closest prediction among the three calculation methods compared to experimental one.
[c] Assignment of the C=O deformation modes has been reversed in comparison to Ref. [4].
[d] Determined from combination bands.

frequencies while the harmonic scaled results are considerably lower (~ 16 cm^{-1}) and the anharmonic frequencies do not show a convincing trend (~ 9 cm^{-1} higher for the ν_{20} band and ~ 4 cm^{-1} lower for the ν_{13} band). This poor result of the harmonic scaled values may be explained by the fact that the scaling factor derived by Andersson and Uvdal was mostly based on stretching frequencies (-CH, -NH, -CC, etc.) and the rms error was 37 cm^{-1}.[11] Also, Scott and Radom commented that the scaling factors for low frequency vibrations are different from the values derived from a particular method across the whole infrared range.[16] Therefore, it is likely serendipitous that the unscaled harmonic calculation outperforms the scaled values. Nevertheless, the latter may provide direction for developing more reliable, less costly calculation methods for predicting vibrational energies. This would require systematic characterization of vibrational modes, particularly in the far infrared fingerprint region in order to accurately determine band centers of a range of molecules.

It should be pointed out that the lowest frequency mode (ν_{21} ring puckering) was observed neither in the present work nor in previous low resolution studies. This is probably due to the low intensity of this mode as the infrared intensity is predicted to be only 0.4% that of the ν_{12} band observed here. However, the band origin of the ν_{21} mode was estimated based on experimental observations of combination bands as 113 cm^{-1}.[4] Assuming this is the actual fundamental frequency of the ν_{21} mode, the closest prediction in Table 4.6 is more than 60% away and this suggests that the modelling of the lowest frequency modes is even more challenging. As discussed above, the comparison between the calculated (harmonic, harmonic scaled and anharmonic B3LYP/ 6-311G++(2d,3p)) and observed vibrational frequencies of β-propiolactone shows that

none of the three methods has demonstrated systematic improvement over the others in terms of prediction accuracy. Consequently, the value of the highly accurate band centers obtained in this study is that they provide benchmarks for theoreticians to improve existing calculation methods with the hope that precise, reliable modeling of molecular motions will be available in the future.

4.6 Summary

This work is the first high resolution microwave and infrared spectroscopic investigation of β-propiolactone. A total of 13311 rovibrational transitions corresponding to the five vibrational bands including the ν_{13} (C=O deformation in-plane), ν_{20} (C=O deformation out-of-plane), ν_{19} (α-CH$_2$ rocking), ν_{12} (ring deformation) and ν_8 (C=O ring stretching) modes was assigned and analyzed using a Hamiltonian model. The resultant spectroscopic constants for the excited vibrational states were accurately determined. The previously misassigned carbonyl in-plane and out-of-plane vibrational modes that overlap were unambiguously corrected based on rovibrational selection rules in this study. A first order *a*-type Coriolis perturbation between these two bands was observed and treated. The combined pure rotational transitions and ground state combination differences from assigned rovibrational transitions provided a set of improved ground state constants that can be used for analyses of other fundamental bands of β-propiolactone.

References

[1] J. Bregman and S. H. Brauer, *J. Am. Chem. Soc*. 77 (1955) 1955–1965.

[2] N. Kwak, J. H. Goldstein and J. W. Simmons, *J. Chem. Phys. 25* (1955) 1203–1205.

[3] D. W. Boone, C. O. Britt and J. E. Boggs, *J. Chem. Phys*. 43 (1965) 1190–1194.

[4] J. R. Durig, *Spectrochim. Acta* 19 (1963) 1225–1233.

[5] K. J. Jalkanen and P. J. Stephens, *J. Phys. Chem*. 95 (1991) 5446–5454.

[6] M. C. Bordejé, O. Mó, M. Yáňez, M. Herreros and J. -L. M. Abboud, *J. Am. Chem. Soc*.115 (1993) 7389–7396.

[7] L. S. Rothman, I. E. Gordon, A. Barbe, D. Chris Benner, P. F. Bernath, M. Birk, V. Boudon, L. R. Brown, A. Campargue, J. -P. Champion, K. Chance, L. H. Coudert, V. Danaj, V. M. Devi, S. Fally, J. -M. Flaud, R. R. Gamache, A. Goldmanm, D. Jacquemart, I. Kleiner, N. Lacome, W. J. Lafferty, J. -Y. Mandin, S. T. Massie, S. N. Mikhailenko, C. E. Miller, N. Moazzen-Ahmadi, O. V. Naumenko, A. V. Nikitin, J. Orphal, V. I. Perevalov, A. Perrin, A. Predoi-Cross, C. P. Rinsland, M. Rotger, M. Šimečková, M. A. H. Smith, K. Sung, S. A. Tashkun, J. Tennyson, R. A. Toth, A. C. Vandaele and J. Vander Auwera, *J. Quant. Spectrosc. Radiat. Transfer*. 110 (2009) 533-572.

[8] Gaussian 03, Revision C.02, M. J. Frisch, G. W. Trucks, H. B. Schlegel, G. E. Scuseria, M. A. Robb, J. R. Cheeseman, J. A. Montgomery, Jr., T. Vreven, K. N. Kudin, J. C. Burant, J. M. Millam, S. S. Iyengar, J. Tomasi, V. Barone, B. Mennucci, M. Cossi, G. Scalmani, N. Rega, G. A. Petersson, H. Nakatsuji, M. Hada, M. Ehara, K. Toyota, R. Fukuda, J. Hasegawa, M. Ishida, T. Nakajima, Y. Honda, O. Kitao, H. Nakai, M. Klene, X. Li, J. E. Knox, H. P. Hratchian, J. B. Cross, V. Bakken, C. Adamo, J. Jaramillo, R.

Gomperts, R. E. Stratmann, O. Yazyev, A. J. Austin, R. Cammi, C. Pomelli, J. W. Ochterski, P. Y. Ayala, K. Morokuma, G. A. Voth, P. Salvador, J. J. Dannenberg, V. G. Zakrzewski, S. Dapprich, A. D. Daniels, M. C. Strain, O. Farkas, D. K. Malick, A. D. Rabuck, K. Raghavachari, J. B. Foresman, J. V. Ortiz, Q. Cui, A. G. Baboul, S. Clifford, J. Cioslowski, B. B. Stefanov, G. Liu, A. Liashenko, P. Piskorz, I. Komaromi, R. L. Martin, D. J. Fox, T. Keith, M. A. Al-Laham, C. Y. Peng, A. Nanayakkara, M. Challacombe, P. M. W. Gill, B. Johnson, W. Chen, M. W. Wong, C. Gonzalez and J. A. Pople, Gaussian, Inc., Wallingford, CT USA (2004)

[9] V. Barone, *J. Chem. Phys*. 120 (2004) 3059-3065.

[10] V. Barone, *J. Chem. Phys*. 122 (2005) 014108.

[11] M. P. Andersson and P. Uvdal, *J. Phys. Chem. A* 109 (2005) 2937–2941.

[12] H. M. Pickett, *J. Mol. Spectrosc*. 148 (1991) 371-337.

[13] C. F. Neese, Loomis-Wood Add-In (LWA) for Igor Pro, Version 2.0; 56th Ohio State University International Symposium on Molecular Spectroscopy, Columbus, OH, June 20−24, 2005, http:// fermi.uchicago.edu/freeware/LoomisWood.shtml.

[14] IGOR Pro Manual, WaveMetric Inc., Lake Oswego, OR USA (2008)

[15] I. M. Mills, *Pure Appl. Chem*.11 (1965) 325-344.

[16]A. P. Scott and L. Radom, *J. Phys*. *Chem.* 100 (1996) 16502-16513.

Chapter 5

A high resolution study of the rovibrational spectra of 3-oxetanone [a]

5.1 Introduction

In this chapter, the high resolution spectroscopic investigation of potential functions in four-membered heterocyclic molecules is extended to 3-oxetanone (c-$C_3H_4O_2$). This is a structural isomer of β-propiolactone (2-oxetanone, C_s) having C_{2v} symmetry with the C=O group on the C_2 axis (a-axis in Figure 5.1) and all heavy atom are coplanar. As for β-propiolactone, 3-oxetanone has been the subject of studies aiming to determine its structure and dynamics. The structural parameters were probed by semi-empirical[1] and *ab initio*[2, 3] calculations. On the experimental front, the microwave results from Gibson and Harris have confirmed that the backbone of 3-oxetanone is planar with a permanent dipole moment of 0.877 D.[4] The planarity was further rationalized by Meinzer and Pringle who conducted an examination of the balance between torsional strain and ring strain and their connection to ring planarity in a series of heterocycles based on experimental ring puckering spectra.[5] A comprehensive low resolution infrared and Raman study in the gaseous and liquid phases by Durig led to the assignment of all 21 fundamental bands of 3-oxetanone without rotational resolution.[6] To date, 3-oxetanone has not been studied by high resolution techniques.

---

[a] A version of the work presented in this chapter has been published. Z. Chen and J. van Wijngaarden, Journal of Molecular Spectroscopy, 279 (2012) 31–36 copyright © 2012 Elsevier and Z. Chen and J. van Wijngaarden, Journal of Physical Chemistry A, 116 (2012) 9490-9496 copyright © 2012 American Chemical Society.

Figure 5.1: Structure of 3-oxetanone in its principal axis system.
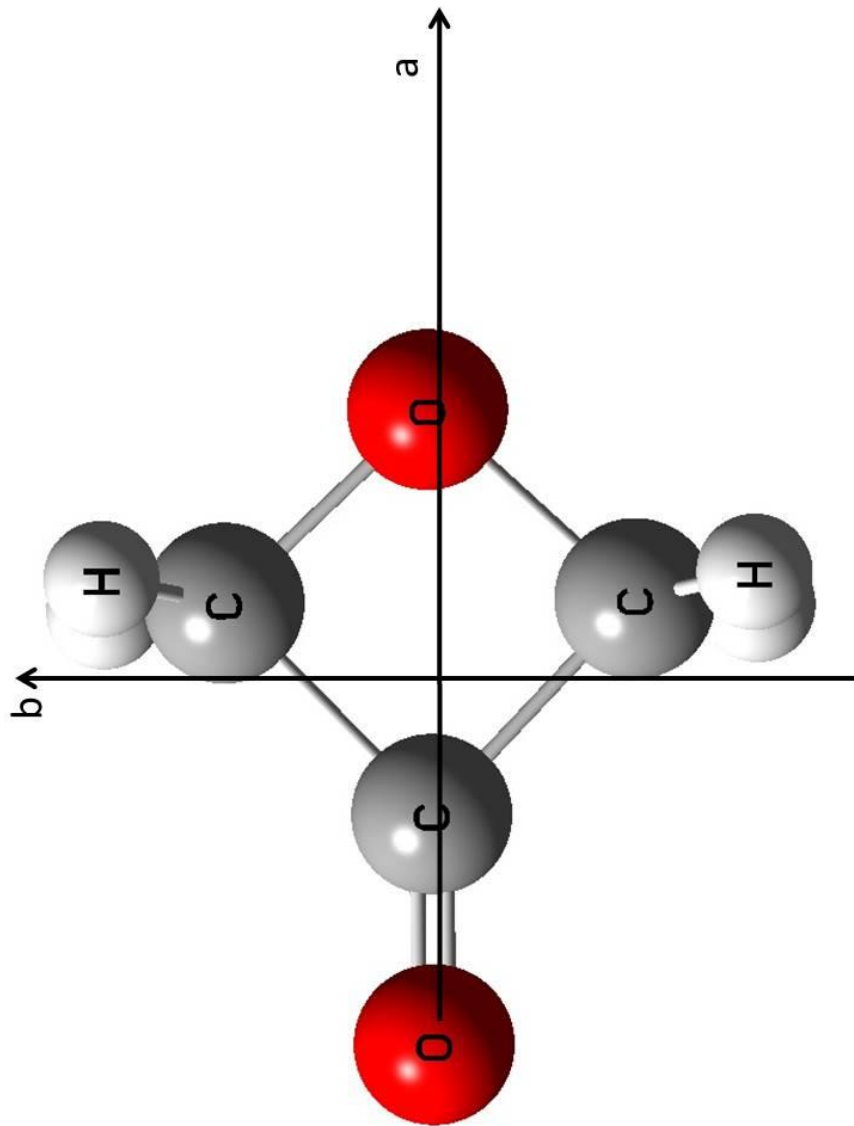
Carreira and Lord carried out the first study of the ring puckering mode of 3-oxetanone using low resolution infrared spectroscopy.[7] Later, Durig *et al.* observed the fundamental of this mode and several vibrational satellites between 140 and 150 cm^{-1} in a more comprehensive infrared and Raman study in the gaseous and liquid phases.[6] The estimated band origins from both studies were fit to a Hamiltonian model and the results support a single-well potential with a small degree of anharmonic character. A recent *ab initio* calculation by Vansteenkiste *et al.*[8] predicted that 3-oxetanone has a less anharmonic ring puckering potential function compared to those of similar four-membered ring molecules containing carbonyl groups but generally agrees with that derived from the low resolution experimental results. However, the ring puckering spectrum has never been rotationally resolved until the current work.

This chapter presents the first high resolution vibrational study of 3-oxetanone through the assignment and analyses of the rovibrational spectra of the ν_7 (ring deformation), ν_{16} (C=O deformation in-plane), ν_{20} (C=O deformation out-of-plane) and ν_{21} (ring puckering) fundamental bands. Furthermore, the first three vibrationally excited hotbands of the ν_{21} ring puckering mode were observed and analyzed in the spectrally congested region of 100-200 cm^{-1}. The band centers were fit to deduce the ring puckering potential function in the form of V=ax^4+bx^2 using a least squares fitting routine. An *a*-type Coriolis interaction between the two C=O deformation motions, ν_{16} (in-plane) and ν_{20} (out-of-plane) modes, was observed and included in the analysis. Accurate information about the ground vibrational state was established using a combination of pure rotational (Ref. [4]) and rovibrational transitions (this work), which can be used for future high resolution analyses of other bands of this molecule. The band origins

determined in this high resolution study were compared with DFT calculation results and as in the case of β-propiolactone discussed in the previous chapter, there appears to be no systematically reliable method to model low frequency modes in 3-oxetanone.

5.2 Experimental details

The rovibrational spectra of 3-oxetanone were collected at the Canadian Light Source (CLS) using a synchrotron based Fourier transform infrared (FTIR) spectrometer as described in Chapter 3. The collection of the spectra was conducted in three different spectral windows due to the intensity differences among the target bands and technical limitations of the required optical components as described below. Generally, the sample was prepared at room temperature by letting vapour pressure from a liquid sample (97% purity, Synthonix) occupy the 2 m multipass gas cell with a total absorption pathlength of 72 m. During the course of the whole experiment, the instrument's entire 9.4 m optical path difference was utilized to achieve the maximum spectral resolution (0.000959 cm^{-1}) for all regions.

For the low intensity ν_7 band, a vapour pressure of 708 mTorr was used. A total of 758 separate interferograms were recorded over ~78 hours and averaged, followed by Fourier transformation between 500 and 1130 cm^{-1} to yield the spectrum. For this particular region, a KBr beamsplitter and a GeCu detector were fitted to the spectrometer. The Doppler line width of 3-oxetanone in this region is such that the observed line widths (FWHM) were instrument limited and this is true for all other modes in this study as the ν_7 vibration is the highest frequency band. To record the spectrum of the ν_{16} and ν_{20} bands in the range of 360-550 cm^{-1}, the spectrometer was equipped with a 6 μm Mylar

beamsplitter and a GeCu detector. In total, 454 interferograms were collected over ~45 hours at a reduced pressure of 188 mTorr. For the ν_{21} ring puckering mode, 310 separate interferograms were recorded in the 100-200 cm^{-1} region at a vapour pressure of 78 mTorr with the spectrometer outfitted with 6 μm Mylar beamsplitter and a helium-cooled Si bolometer detector. Background interferograms for each setup were collected at lower resolution (0.01536 cm^{-1}), averaged and the result was Fourier transformed with appropriate zero filling before the calculation of the final spectra. Some important experimental parameters are summarized in Table 5.1.

All transitions recorded were calibrated by comparison with known H_2O and N_2O line positions from the HITRAN database.[9] The specific molecules and ranges of transitions used in this calibration process are listed in Table 5.1. Generally, it was found that the measured frequencies were accurate to within 0.0001 cm^{-1}.

Table 5.1: Experimental parameters of recorded bands of 3-oxetanone.

	ν_{21}	ν_{20}	ν_{16}	ν_7
Band origin (cm^{-1})	139.5	339.6	448.2	685.0
Pressure (mTorr)	78	188		708
No. of interferograms	310	454		758
Time spent to record	9	20		78
Resolution (cm^{-1})		0.00096		
Lines used in	H_2O	H_2O		N_2O
calibration	100-200 cm^{-1}	360-490 cm^{-1}		615-725 cm^{-1}

5.3 Frequency calculations

As there were no prior high level calculations of 3-oxetanone, harmonic vibrational frequency calculations were performed using Gaussian 03W[10] at the B3LYP level with a basis set of 6-311++G (2d, 3p) following geometry optimization. An empirical scaling factor of 0.9679 previously reported in the literature was used to scale the calculated harmonic frequencies.[11] The frequency predictions with anharmonic corrections[12, 13] were then calculated via second-order perturbation theory in Gaussian 03W to compare with the harmonic values and experimental results.

5.4 Spectral assignment and analysis

Early microwave studies show that 3-oxetanone has a planar ring skeleton with C_{2v} symmetry as depicted in Figure 5.1. The observed transitions for each of the four individual vibrational modes of 3-oxetanone were initially assigned and analyzed independently. This allowed the assignment of each band to be verified before global analysis. In the end, transitions from the ν_7, ν_{16}, ν_{20} and ν_{21} fundamental bands were co-fit using Watson's A-reduced Hamiltonian in I^r representation in Pickett's SPFIT program[14] from which the spectroscopic parameters for each band were accurately determined. The first three hotbands of the ν_{21} ring puckering mode were also analyzed along with the fundamental transitions in a simultaneous fit. This section details the assignment and analysis of the rovibrational spectra of these four modes of 3-oxetanone.

5.4.1 Infrared spectra of the ν_7 band

The ν_7 band, attributed to ring deformation, has A_1 symmetry which gives rise to *a*-type selection rules *eo*↔*ee* and *oe*↔*oo*. Centered at ~685 cm^{-1}, this band is well separated from other absorption features of 3-oxetanone. Thus, it is less likely to have interaction with adjacent vibrational modes, making it a good candidate to start the analysis. The initial inspection of the rotational structure of the band revealed clear *a*-type patterns of transitions. The estimated band center from the low resolution infrared work[6] combined with the rotational constants from the microwave study[4] provided information needed to generate a simulated spectrum with which the observed patterns were compared. Such comparison led to the tentative assignment of a few strong transitions and the ground state combination differences (GSCDs) were used to confirm the quantum number assignment. With the newly assigned transitions fit using Watson's A-reduced Hamiltonian, I^r-representation in Pickett's SPFIT program,[14] the simulated spectrum was refined, leading to the assignment of more transitions. This process continued in an iterative fashion until the strongest transitions were all assigned.

A total of 2768 *a*-type transitions were assigned including 307 Q branch transitions. Rotational energy levels up to K_a =29 with J (max) = 58 were covered in the P and R branches while the assignment in the Q branch accounted for transitions between K_a = 2 and 35 with J from 4 to 40. With only nine spectroscopic parameters being allowed to vary (three rotational constants and five centrifugal distortion constants for the ν_7 state plus the band origin and the ground state constants fixed to the values determined from GSCDs and microwave data), the rms error of the isolated band fit was only 0.000114 cm^{-1}.

5.4.2 Infrared spectra of the ν_{21} band

The ν_{21} ring puckering mode, first observed by Carreira and Lord between 140 and 150 cm^{-1},[7] has B$_1$ symmetry which gives rise to *c*-type transitions with selection rules *oe*↔*ee* and *eo*↔*oo*. At a glance, a series of sharp Q branches were observed as shown in Figure 5.2. Based on the observed intensities in this work and the assignments reported from previous low resolution studies, these four Q branches correspond to the fundamental and first three hotbands of 3-oxetanone which increase in frequency with the vibrational quantum number v. The P and R branches of these bands are greatly overlapped as the band centers are separated by ~1.5 cm^{-1}.

A Loomis-Wood plot was constructed using the Loomis-Wood add-in (LWA) software package for Igor Pro program[15, 16] with the hope of identifying patterns of regularly spaced transitions. However, unlike the successful use of this scheme in the analysis of β-propiolactone as discussed in Chapter 4, the dense spectrum prevented clear observation of such trends in the plot of this molecule. A portion of the Loomis-Wood plot of the ν_{21} mode of 3-oxetanone is shown in Figure 5.3 a) illustrating the complexity of the spectrum in the R branches between ~152 and ~163 cm^{-1}. This highly congested spectral region apparently arises as a result of having four times the number of transitions, which are on top of each other, compared with a normal (isolated fundamental) band. This forced the initial assignment to be done via trial and error. A few strong transitions were chosen from the R branches (shown as triangles on the Loomis-Wood plot) and a set of quantum numbers was estimated from simulated spectra. Based on this guess, the frequencies of their P branch counterparts (which share the same upper states) were calculated using the known GSCDs obtained from the analysis of the

Figure 5.2: Overview spectrum showing the Q branches of the fundamental and first three hotbands of the v_{21} band of 3-oxetanone.
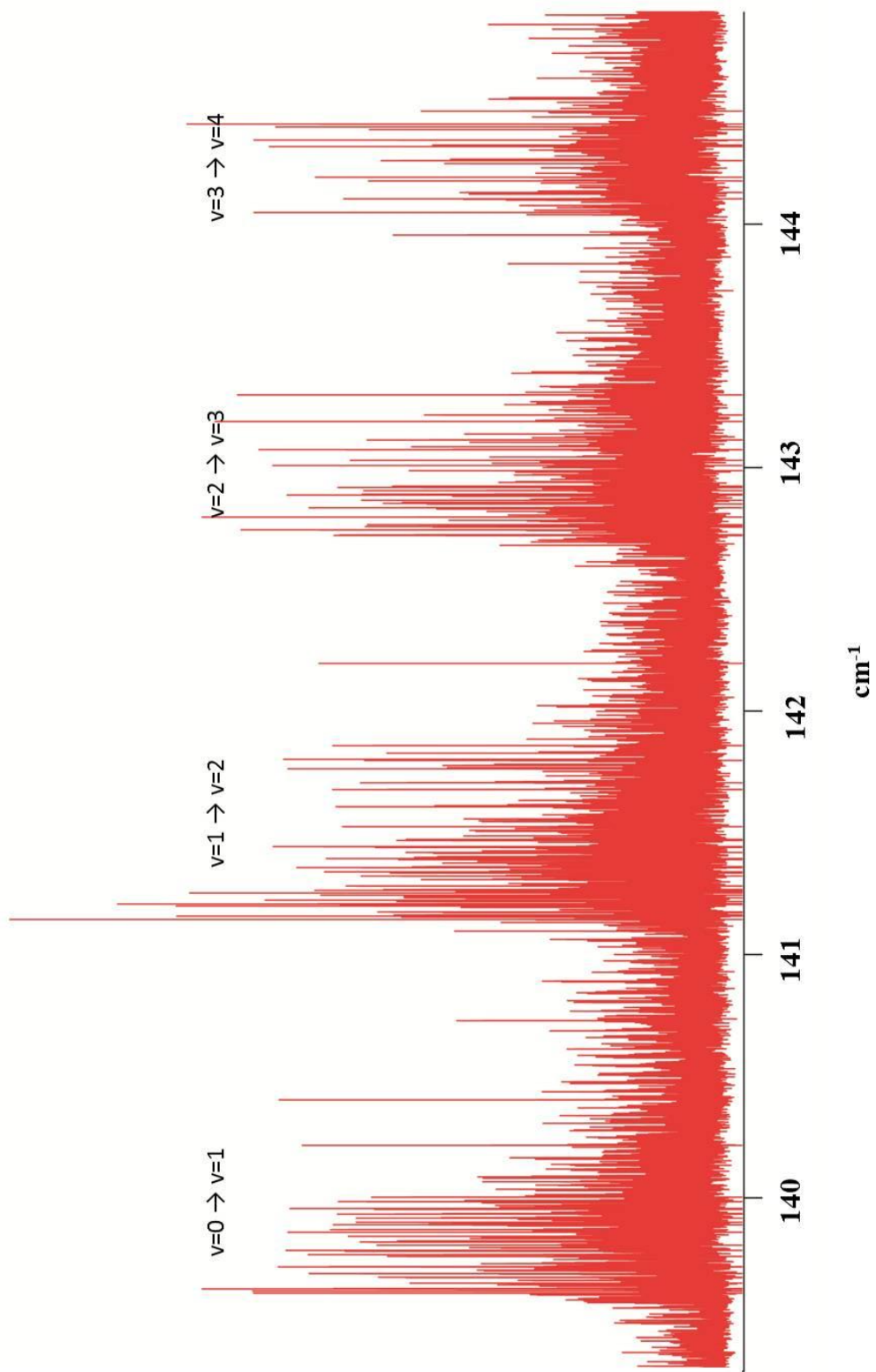
Figure 5.3 a) : A portion of the Loomis-Wood plot of the v_{21} band of 3-oxetanone showing the R branch transitions between 152 and 163 cm^{-1}. Note that no obvious trends are observed in this unlabelled version of the plot.
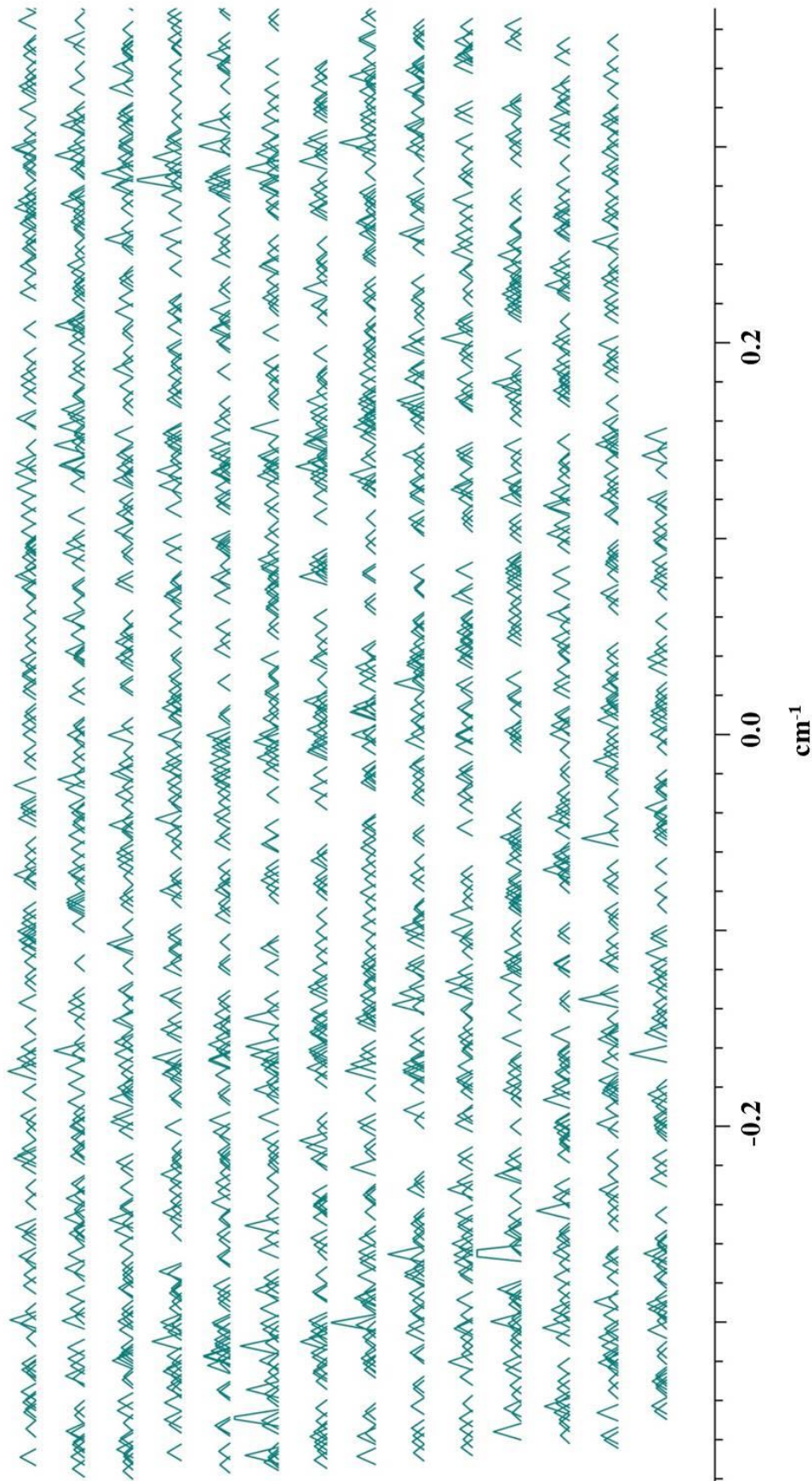
ν_7 band. Should the selected R branch transitions have the correct quantum numbers based on this guess, their P branch counterparts would line up with the predicted frequencies. To eliminate the possibility of accidental matches of P and R branches pairs, which was not uncommon given the line density in this particular case, a series of lines attributed to the same trend had to be assigned to confirm the pattern. The efficiency of such a trial and error assignment depends on how close the guessed quantum numbers of candidate transitions are to their actual values and on the reliability of the ground state information. Once the assignment of a few of the strongest transitions was confirmed, the assignment scheme described in the previous section was followed to assign the remaining transitions in this spectral region. The same Loomis-Wood plot with labeled transitions is given in Figure 5.3 b) and reveals the hidden patterns in the congested R branches of this spectral region. The strongest 12 progressions in the R branches (sharing common K_c) are labelled on the plot. These were assigned to transitions in the fundamental band and first two hot bands of the ν_{21} mode while progressions in the third hot band are absent here due to the low intensity on the scale of this plot.

For the fundamental ν_{21} band, a total of 3237 c-type transitions between $K_a=0$ and 43 with J (max) = 53 were assigned, including 400 transitions from the spectrally congested Q branch. Once the higher state (v = 1) was well determined from the fit, it served as the lower state to calculate combination differences (equivalent to the ground state combination differences in the analysis of any fundamental bands) in the assignment of transitions within the first hot band (v = 1→ v = 2). This allowed the assignment of 2668 P, Q and R branch rovibrational transitions from the first hot band, spanning

Figure 5.3 b) : The labelled version of Figure 5.3 a) with transitions due to the strongest progressions of the fundamental and first two hotbands of the ν_{21} band of 3-oxetanone marked. Note that the labels were added after the successful assignment.

100
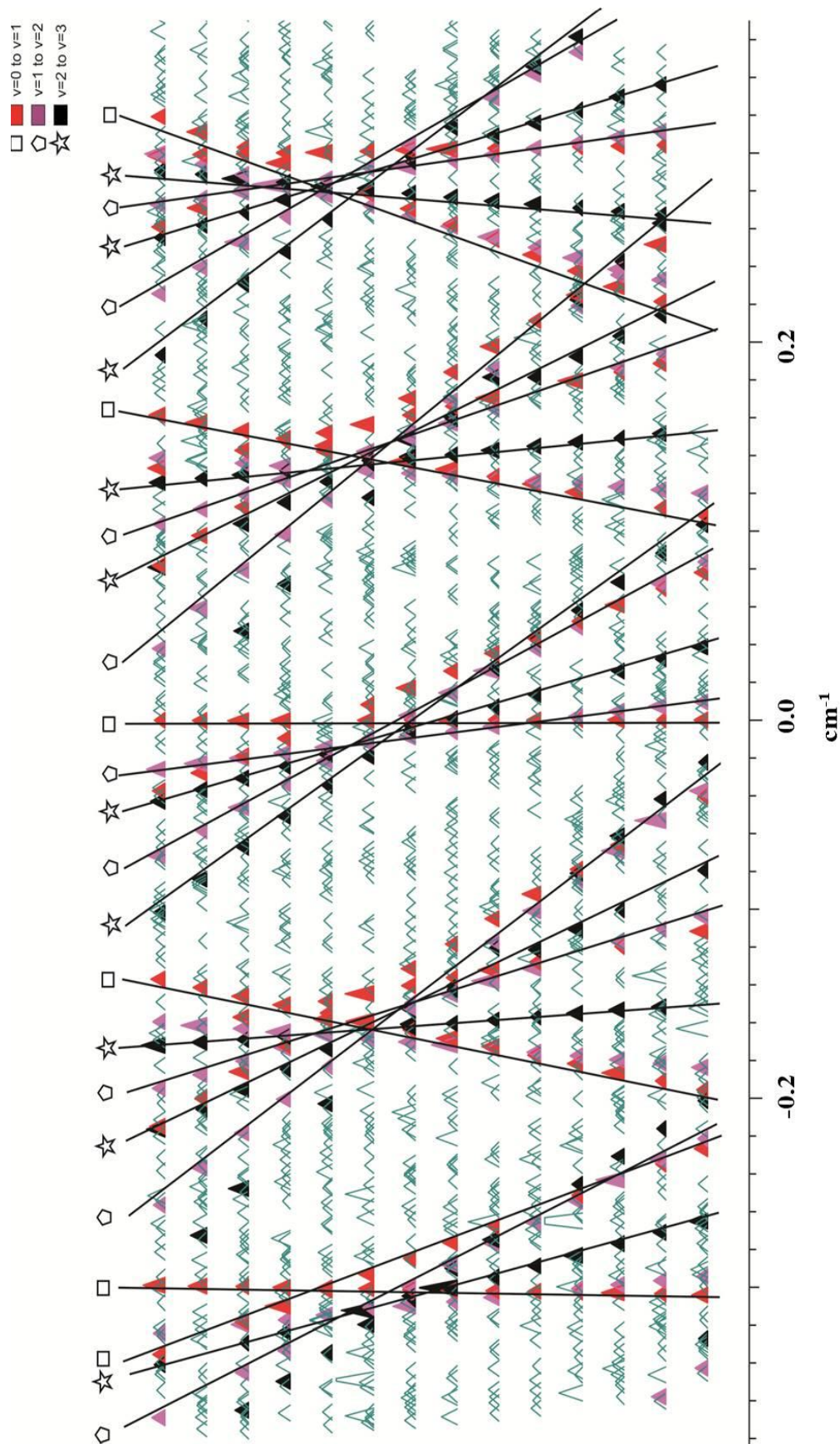
quantum number K_a from 0 to 42 with J (max) = 44. The spectra of the second and third hotbands were assigned in a similar manner. For the v=2→v=3 band, 2178 rovibrational transitions were assigned between K_a=0 and 37 with J (max) = 50. Due to the low intensity of the v=3→v=4 band, high J transitions of this hot band were too weak to be observed. As a result, only 1082 P, Q and R branch rovibrational transitions, about half the number of the assigned transitions for the second hot band, were assigned with K_a values from 0 through 29 and J values up to 30. To demonstrate the complexity of the analysis, Figure 5.4 shows a narrow spectral window of 0.15 cm^{-1} containing more than 20 transitions assigned to all four bands.

5.4.3 Infrared spectra of the v_{16} and v_{20} bands

5.4.3.1 Initial analysis of v_{16} and v_{20} bands

The v_{20} C=O deformation out-of-plane mode at 399.6 cm^{-1} has B_1 symmetry corresponding to c-type selection rules (*oe↔ee* and *eo↔oo*). The v_{16} band, attributed to the in-plane mode of C=O deformation at 448.2 cm^{-1}, has B_2 symmetry which give rise to the b-type selection rules (*eo↔oe* and *ee↔oo*). Compared to the isolated v_7 band previously discussed in section 5.4.1, the assignment of these two bands was more challenging not only because the v_{16} band is inherently weak, but also because the R branch of the v_{20} band significantly overlaps the P branch of the v_{16} band. This results in a very dense spectrum as shown in Figure 5.5. For this analysis, a Loomis-Wood plot was constructed in an effort to identify patterns of the strongest progressions of transitions. An example of this is shown in Figure 5.6.

Figure 5.4: A 0.15 cm⁻¹ spectral window of the R branches of the ν_{21} fundamental and the first three hotbands of 3-oxetanone showing the congested spectrum in this range.
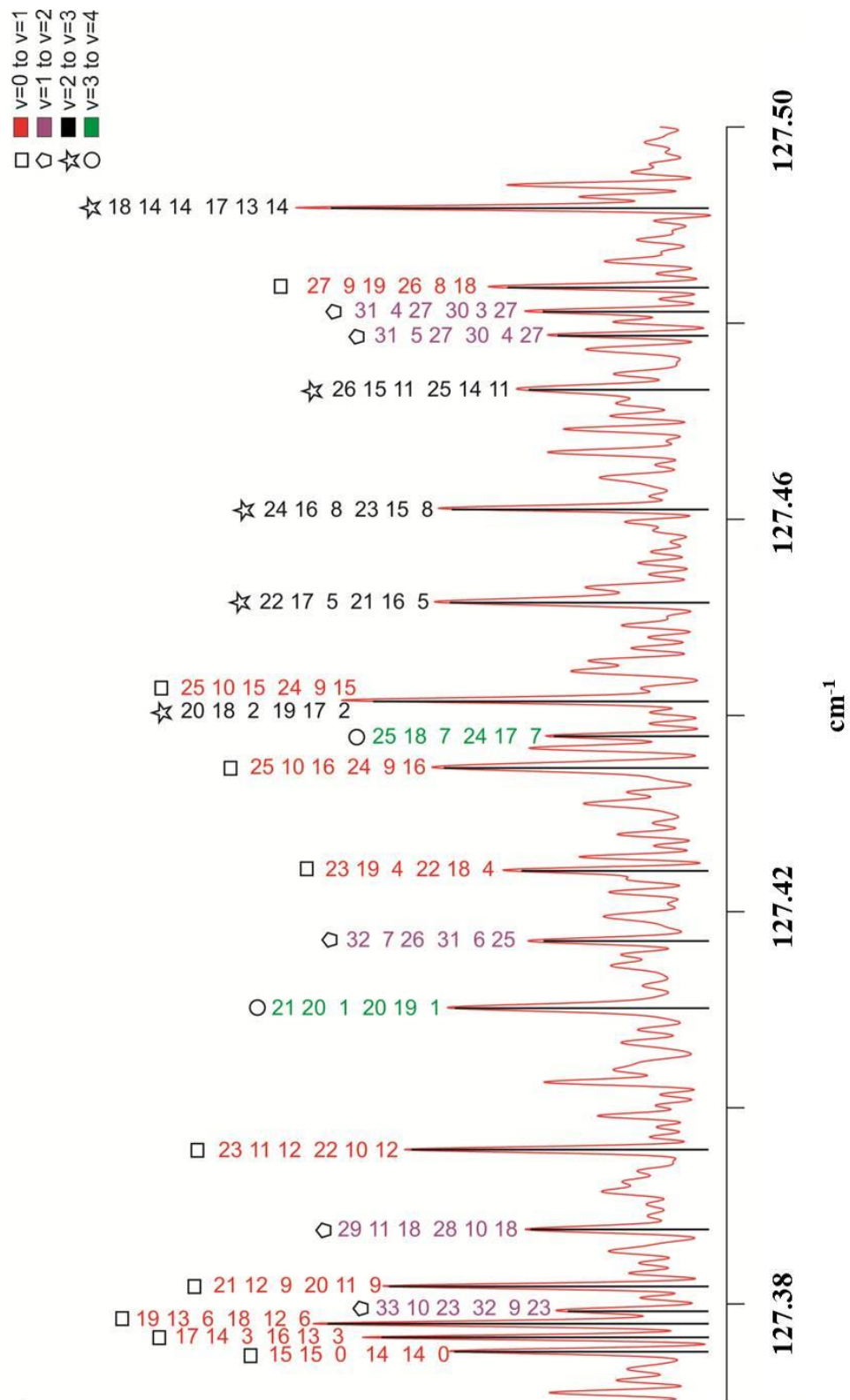
Figure 5.5: An overview spectrum showing the c- and a-type band structure of the ν_{20} and ν_{16} bands of 3-oxetanone at $\sim$399 cm^{-1} and $\sim$448 cm^{-1}, respectively. Notice that the R branch of the ν_{20} band overlaps the P branch of the ν_{16} band.
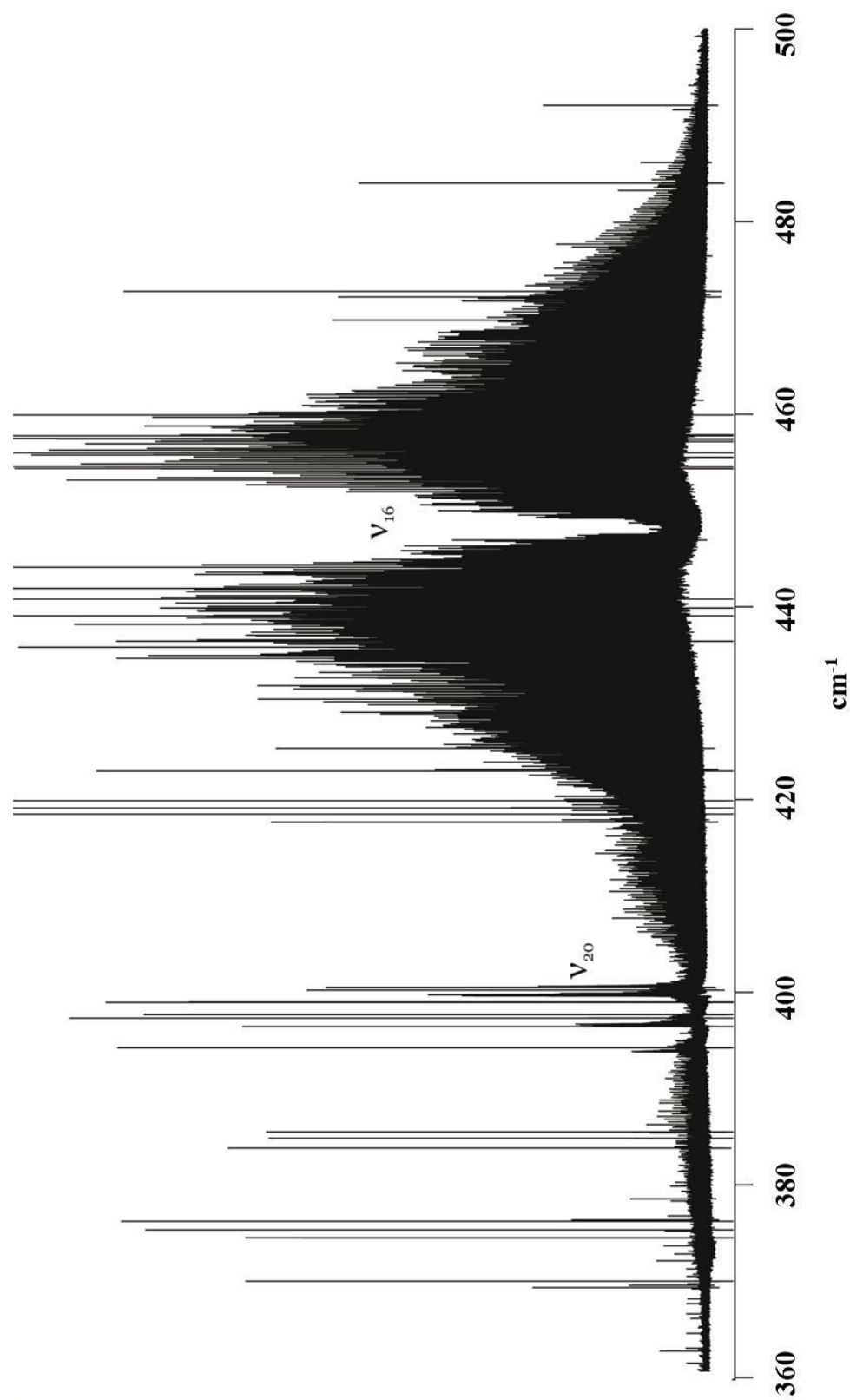
Figure 5.6: A portion of the Loomis-Wood plot of the v_{16} band of 3-oxetanone between ~452 and ~457 cm^{-1} showing b-type progressions used to aid in its assignment.
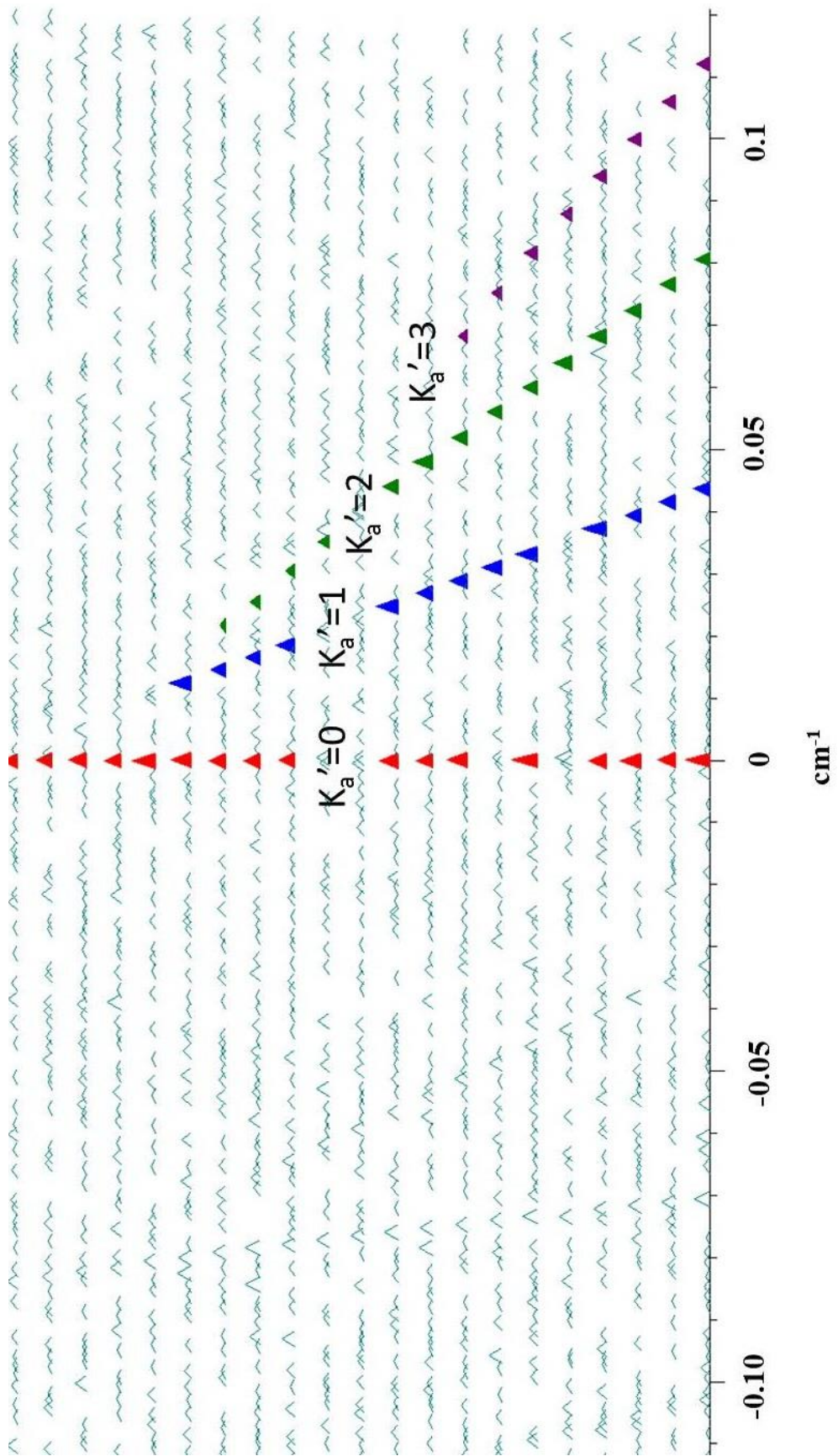
During the preliminary assignment stage, while many transitions lined up almost at the calculated frequencies, a number of transitions appeared to be noticeably shifted from their predicted frequencies. Figure 5.7 shows an example of one of these outliers. In the preliminary fits of the individual bands, certain excited states parameters (most notably A and Δ_K) were inconsistent with those in the ground state and, more importantly the Hamiltonian model could not account for many unassigned transitions (most of which were high K_a or K_c lines for the *a*- or *c*- type bands, respectively). Such discrepancies suggested that there were perturbations between these two adjacent bands, which are 48 cm^{-1} apart and share a large overlapping range. Also it can be seen in Figure 5.5 that the ν_{20} spectrum exhibits a 3:1 intensity ratio between the P and R branches and this is often an indication of intensity borrowing as a result of interaction with nearby energy levels of another band. To fully account for the observed perturbation, efforts were made to seek a set of "perturbation free" ground state spectroscopic constants as outlined below. This is done to ensure that the spectroscopic constants for both the ground state and excited states are physically meaningful rather than "effective" constants that reflect the best mathematical solution.

5.4.3.2 Determination of the ground state spectroscopic constants

A combination of pure rotational and rovibrational transitions from Ref. [4] and the ν_{21}, ν_{16}, ν_{20} and ν_7 bands in this work was used to determine the ground state spectroscopic constants of 3-oxetanone via direct fitting of the microwave frequencies and GSCDs. GSCDs obtained from the *a*-/*b*-type rovibrational transitions provide coverage of energy levels with high J and K_c values while those from the *c*-type bands

105

Figure 5.7: Zoomed-in section of the P branch of the *b*-type v_{16} band of 3-oxetanone showing the effect of Coriolis interaction with the *c*-type v_{20} band. The stick lines show the predicted frequencies of these labeled transitions in the absence of perturbation.
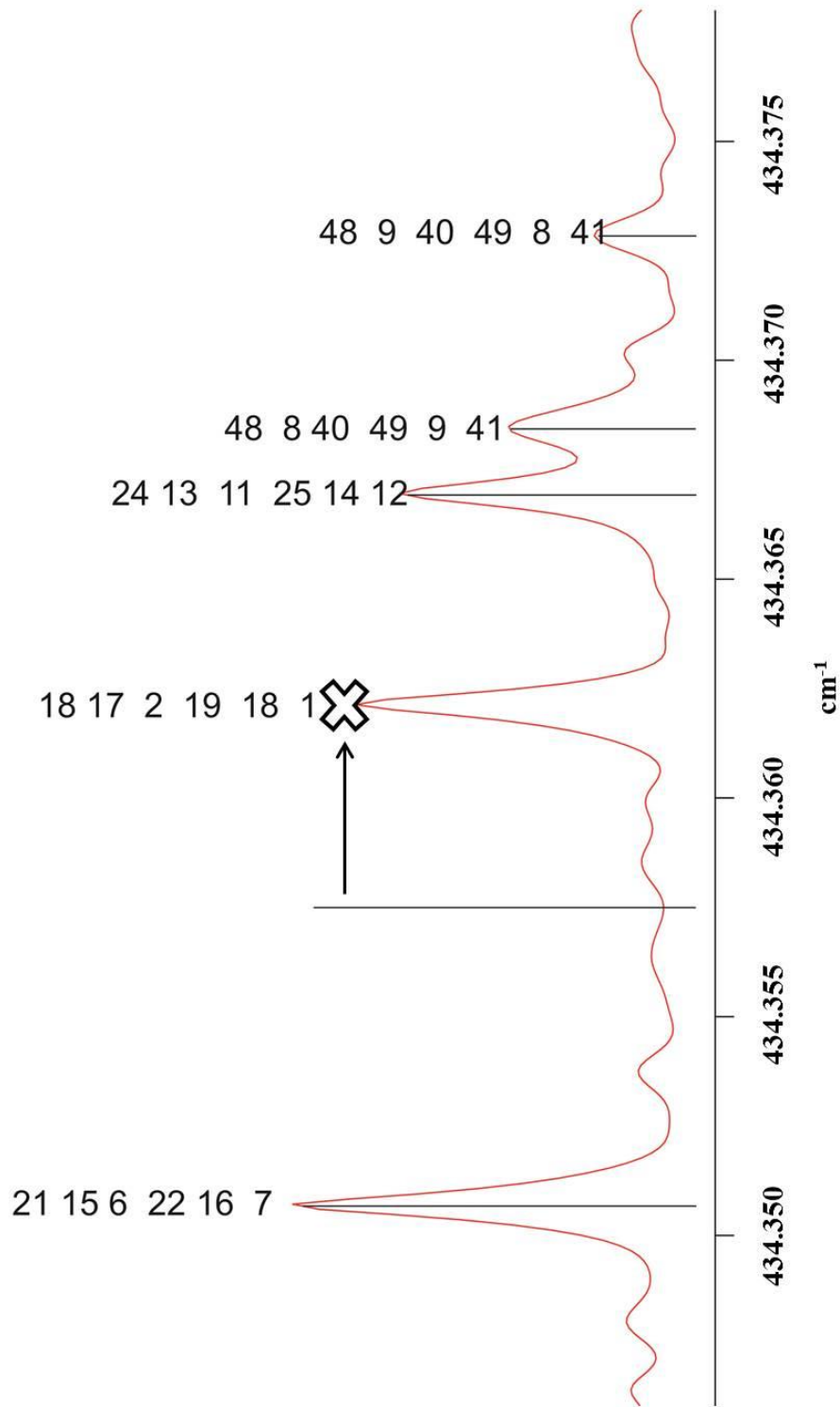
offer information about the high K_a levels. When GSCDs obtained from all three types of bands were combined, the ground state parameters were well-determined, owing to the broad coverage of energy levels provided by such a set. In the end, 2532 rovibrational GSCDs were obtained from four vibrational bands of 3-oxetanone with J up to 61 and K_a (max) = 34. This set of GSCDs supplemented with the nine previously reported pure rotational transitions[4] was fit using Watson's A-reduced Hamiltonian in I^r representation in Pickett's SPFIT program.[14] The resultant spectroscopic constants are presented in Table 5.2. The uncertainty assigned to the pure rotational transitions was 1/1500 that of the infrared transitions to reflect the greater precision of the microwave data. The ground state constants were held fixed in the subsequent global analyses of the excited vibrational states.

5.4.3.3 Perturbation analysis the ν_{16} and ν_{20} bands

Based on C_{2v} symmetry, two bands with B_2 (ν_{16}) and B_1 (ν_{20}) vibrational symmetries may interact through an *a*-type Coriolis perturbation.[17] Since the untreated perturbation was isolated through the isolated characterization of ground state energy levels, the Coriolis coupling can be dealt with in the upper states directly. A symmetry-permitted *a*-type Coriolis coupling constant G_a was incorporated into the Hamiltonian model, allowing the assignment of the remaining high K_a and K_c transitions in the ν_{20} and ν_{16} bands, respectively. Figure 5.8 shows a zoomed-in section in the Q branch of the ν_{20} band where transitions sharing common J=26 line up nicely with the predicted frequencies. In total, 4143 transitions were assigned for the *b*-type ν_{16} band including 949 transitions from the Q branch. The spanned quantum numbers of assigned transitions

Table 5.2: Spectroscopic constants for the ground state, ν_{21}, ν_{20}, ν_{16} and ν_7 fundamental states of 3-oxetanone.

	Ground state	ν_{21}	ν_{20}	ν_{16}	ν_7
ν / cm^{-1}	0	139.549148(5)	399.588606(6)	448.194670(5)	684.994728(7)
Rotational constants / cm^{-1}					
A	0.40455571(3)	0.4030009784(18)	0.40533(2)	0.40484(2)	0.404063372(4)
B	0.16532500(2)	0.16545977(3)	0.16542474(3)	0.16536694(3)	0.16519845(3)
C	0.12297756(2)	0.12330109(4)	0.12309730(3)	0.122781360(17)	0.122850816(17)
Centrifugal distortion constants / 10^{-9} cm^{-1}					
Δ_J	21.73(6)	22.642(16)	21.984(11)	21.882(4)	21.895(8)
Δ_{JK}	150.6(4)	144.86(8)	140.66(16)	164.62(15)	152.03(5)
Δ_K	103.4(4)	110.79(7)	102.56(14)	112.94(12)	104.10(5)
δ_j	5.28(3)	4.963(14)	5.213(6)	5.367(2)	5.299(5)
δ_k	90.8(8)	87.8(3)	101.5(3)	86.5(3)	91.90(8)
Coriolis interaction parameter / cm^{-1}					
G_a (16,20)	-	-	0.3402(17)		-
rms error / cm^{-1}	0.000159		0.000108		

Figure 5.8: Transitions sharing common J=26 quantum number from the Q branch of the c-type ν_{20} band of 3-oxetanone. The stick lines show their predicted frequencies.
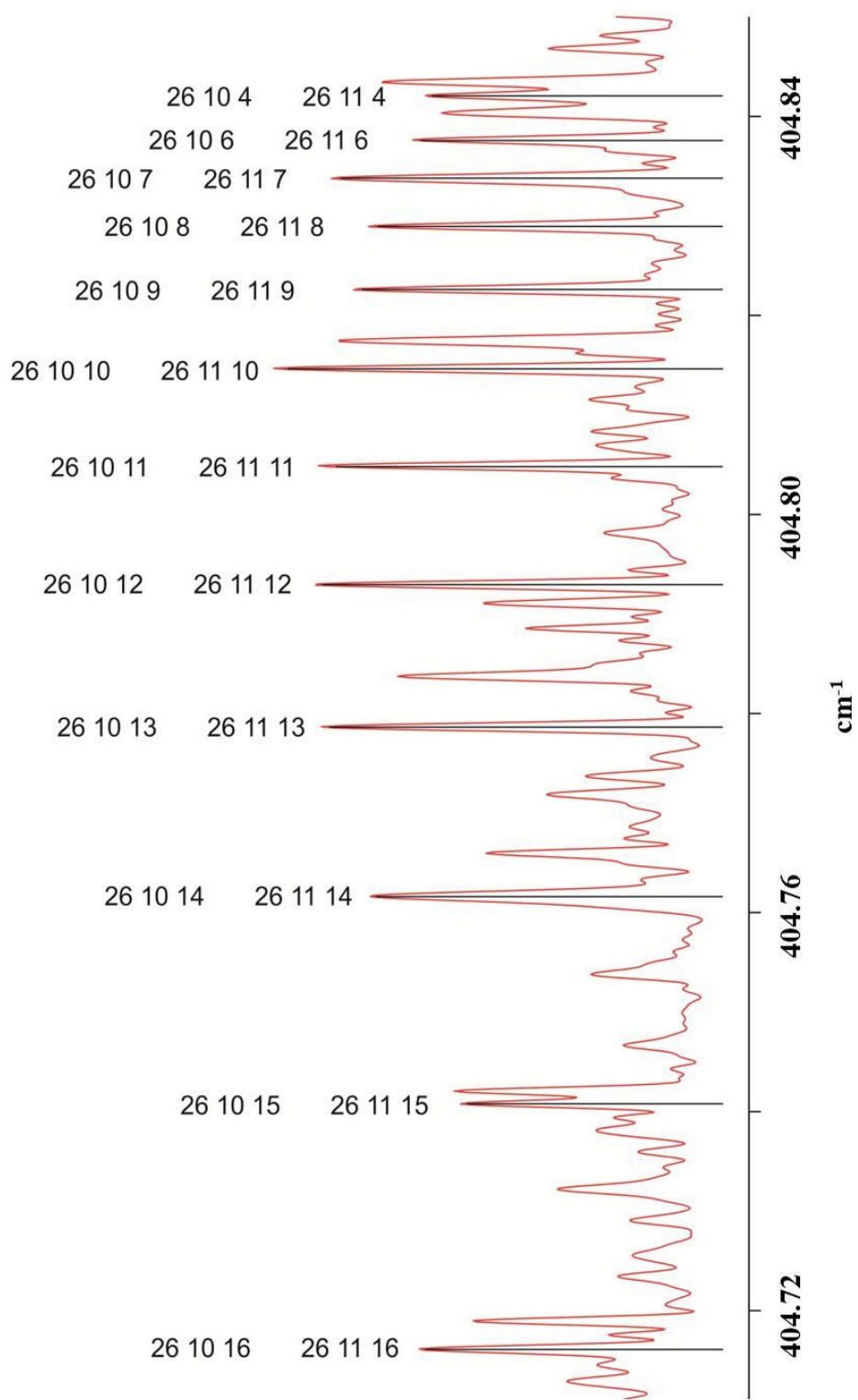
include those in the P and R branches from J=1 through 74 with a maximum K_a value of 37. Transitions in the Q branch were assigned with K_a between 0 and 32 and J up to 46. For the c-type ν_{20} band, overall 2814 P and R branch transitions between K_a =4 and 45 with J (max) =45 and 594 Q branch transitions with K_a up to 19 with a maximum J value of 52 were assigned. The rovibrational analysis of 7551 transitions assigned from these two vibrational states yielded a rms error of only 0.000108 cm^{-1} with the ground state constants held fixed to values determined from the analysis described in the previous section.

5.4.4 Global analysis

Two global fits which incorporate rovibrational transitions from multiple vibrational energy levels were performed in Pickett's SPFIT program using Watson's A-reduced Hamiltonian, I^r-representation[14] with the ground state spectroscopic constants held fixed to values calculated from GSCDs. A total of 13556 rovibrational transitions from all fundamentals (ν_7, ν_{16}, ν_{20} and ν_{21} bands) were fit in a simultaneous way and the resulting spectroscopic constants are listed in Table 5.2. A second global fit including 9 165 transitions from the fundamental and first hotbands of the ν_{21} ring puckering mode was established, and a set of spectroscopic parameters was obtained as shown in Table 5.3.

Table 5.3: Spectroscopic constants for the ground state and the first four vibrational energy levels of the ν_{21} vibration of 3-oxetanone.

	Ground state	ν_{21} v=1	ν_{21} v=2	ν_{21} v=3	ν_{21} v=4
ν / cm^{-1}	0	139.549148(5)	141.093457(14)	142.644034(19)	143.989670(26)
Rotational constants / cm^{-1}					
A	0.4045571(3)	0.4030009784(18)	0.401443410(3)	0.39987326(4)	0.39828864(9)
B	0.16532500(2)	0.16545977(3)	0.16560914(5)	0.16577090(10)	0.16594099(19)
C	0.12297756(2)	0.12330109(4)	0.12362574(7)	0.12393918(14)	0.1242563(3)
Centrifugal distortion constants / $\times10^9$ cm^{-1}					
Δ_J	21.73(6)	22.642(16)	23.85(3)	23.62(5)	25.87(13)
Δ_{JK}	150.6(4)	144.86(8)	138.04(15)	139.4(3)	129.8(6)
Δ_K	103.4(4)	110.79(7)	117.99(13)	110.0(3)	105.8(5)
δ_j	5.28(3)	4.963(14)	4.39(3)	5.34(5)	4.38(15)
δ_k	90.8(8)	87.8(3)	89.6(6)	68.3(13)	90(2)
rms error /	0.000159		0.000098		

5.5 Discussion

5.5.1 Determination of ground state spectroscopic constants

Despite the fact that the pure rotational measurements normally offer better precision, the ground state spectroscopic parameters obtained from fitting the ground state combination differences in this work are better determined than those in the prior microwave work.[4] This is a result of the inclusion of energy levels spanning a larger range of quantum numbers (the coverage of high J and K_c levels from the *a-* and *b-* type bands and the high K_a levels assigned from the *c*-type bands in this study). The latter are sensitive to centrifugal distortion constants, whereas the microwave data consisting of nine pure rotational transitions (sampled energy levels to up to J =3) was only fit with the rotational constants A, B and C. As shown previously for β-propiolactone, the improved ground state parameters were key to successful rovibrational assignment of the far infrared spectrum and in this case, this was essential for unravelling both the Coriolis perturbed bands and the congested hot band spectra. Thus, even though 3-oxetanone has greater symmetry, careful characterization of the ground state spectroscopic parameters is important.

5.5.2 The perturbation between the v_{16} and v_{20} bands

During the initial assignment of the overlapping v_{16} and v_{20} bands, it was found that, although the strongest transitions were readily assigned, the rotational constant A and the centrifugal distortion constant Δ_K seemed to be "effective" constants as they were not consistent with their ground state counterparts as shown in Table 5.4. With the inclusion of the Coriolis interaction parameter G_a, the spectroscopic parameters A and Δ_K

Table 5.4: Subset of spectroscopic parameters (cm^{-1}) that illustrate the effect of including and excluding the a-type Coriolis interaction term between the v_{16} and v_{20} states of 3-oxetanone with fitting transitions from these two bands only.

	Ground state	Without perturbation treatment		With perturbation treatment	
		v_{20}	v_{16}	v_{20}	v_{16}
A	0.4045571(3)	0.40295009(7)	0.40721404(7)	0.40533(2)	0.40484(2)
Δ_K /10^{-9}	103.4(4)	11.52(13)	205.16(7)	102.56(14)	112.94(12)
G_a		-		0.3402(17)	
rms error		0.000295		0.000108	

showed better consistency with the ground state analogues as seen in Table 5.4, however, the excited state A rotational constant became less well-determined due to a high correlation between G_a and itself. The rms error of the three-state fit (the ground state, ν_{16} and ν_{20} states) was reduced by a factor of three when G_a was included in the fit, meaning that this set of constants gives a much better description of the observed spectra of the ν_{16} and ν_{20} bands. Furthermore, this term allowed extensive assignment of the rotational structure of the two low frequency bands (over 7000 transitions in total for these two bands alone). This study shows that interacting bands should be analyzed together so that the perturbation can be dealt with. It should be pointed out that the symmetry considerations (discussed in Section 3.3.1.2) provided a very useful guideline to predict and analyze this type of perturbation which when left untreated often prevents complete assignment of rovibrational spectra. The successful application of this scheme can be extended to the spectral analyses of other molecules.

As a similar a-type Coriolis interaction was observed in β-propiolactone (also between two in-plane and out-of-plane C=O deformation modes as discussed in Section 4.5.2), it is interesting to compare this coupling in these two structural isomers. The G_a values determined for both molecules have positive signs, indicating a positive Coriolis interaction. This is consistent with the observed intensity stealing from the R branch of the higher band (ν_{16}) and the P branch of the lower band (ν_{20}). An imbalanced intensity ratio of 1:3 between the P and R branches of the ν_{20} band is very obvious in Figure 5.5. The rms error of the three-state fit was reduced by a factor of three when G_a was included in the Hamiltonian model for 3-oxetanone while a factor of 30 reduction was obtained for β-propiolactone. Mathematically, a large rms error may be due to the number of

perturbed transitions, the magnitude of the perturbation (to individual transitions), or both. The former is supported by the examination of individual $\nu_{obs-cal}$ values in the non-Coriolis fit which revealed many more transitions affected by Coriolis interaction in the β-propiolactone case. This is not surprising because the two coupled states of β-propiolactone are only ~12 cm^{-1} apart whereas the ν_{16} and ν_{20} bands of 3-oxetanone are separated by almost 50 cm^{-1}, meaning that more rovibrational energy levels are close enough to potentially interact with each other in the former in comparison to the latter.

5.5.3 The ν_{21} ring puckering mode

5.5.3.1 The ring puckering potential function

Transitions from the ν_{21} ring puckering fundamental and first three hotbands were unambiguously assigned using lower and upper state combination differences, resulting in a simultaneous fit of 9165 lines with a rms error of only 0.000098 cm^{-1}. Such remarkably low rms error indicates that the Hamiltonian model gives an accurate description of the energy levels in the first four excited states of the ring puckering potential energy ladder. Among those spectroscopic constants determined from the rovibrational analysis, the corresponding band centers were accurately determined as: 139.549148(5) cm^{-1} (fundamental), 141.093457(14) cm^{-1} (v = 1→ v = 2), 142.644034(19) cm^{-1} (v = 2→v = 3) and 143.989670(26) cm^{-1} (v = 3→v = 4). A least squares fitting method was used to derive the ring puckering potential function of 3-oxetanone.[18] This is based on a Hamiltonian model for an oscillator in the form of: $\hat{H} = \frac{\hat{p}}{2\mu} + ax^4 + bx^2$ (μ is the ring puckering reduced mass of 3-oxetanone, assumed to be 151 amu as determined in Ref. [7]). Using the band centers from this study, the potential function was

determined in the form of $V = a\text{x}^4 + b\text{x}^2$ where $a = 2.04388 \times 10^5$ cm^{-1}/Å^4 and $b = 4.26392 \times 10^4$ cm^{-1}/Å^4. The positive sign of the quadratic term b is indicative of a single-well potential function.

Comparing the values with those in Carreira and Lord's work ($a = 1.86 \times 10^5$ cm^{-1}/Å^4 and $b = 4.31 \times 10^4$ cm^{-1}/Å^4), the quartic term has changed considerably (~10%) relative to the quadratic coefficient b. This is likely caused by the fact that their reported band centers are systematically blue-shifted, most severely for the first two bands by about a half wavenumber. Figure 5.9 shows an example of the Q branch structure of the ring puckering fundamental. It can be seen that the determined band center from this high resolution study is the frequency of the onset of the sharp Q branch structure whereas the point of maximum absorption was chosen in the low resolution study. This comparison underlines the value of high resolution investigation in the accurate determination of potential energy functions that reflect molecular properties.

From a chemical point of view, a larger quartic constant (a) determined from this work implies greater ring strain (in favour of a planar ring) in 3-oxetanone than previously thought as the quartic term reflects the magnitude of the ring strain while the quadratic term indicates the torsional forces. This is consistent with Meinzer and Pringle's conclusion that there is a reduction in torsional repulsion that accompanies insertion of a carbonyl group, favouring a planar ring.[5] Mathematically, an increased a constant in a function of form $V = a\text{x}^4 + b\text{x}^2$ suggests that the shape of the potential is flatter about its minimum and less harmonic than expected from early studies. However, compared with related four-membered heterocycles, 3-oxetanone's ring puckering potential is still considered fairly harmonic.[8]

Figure 5.9: An overview of the Q branch of the v_{21} fundamental band of 3-oxetanone. The arrow on the left marks the band center determined from fitting 3237 infrared transitions in the current work, the arrow on the right labels the band origin estimated from the low resolution study in Ref. [7].
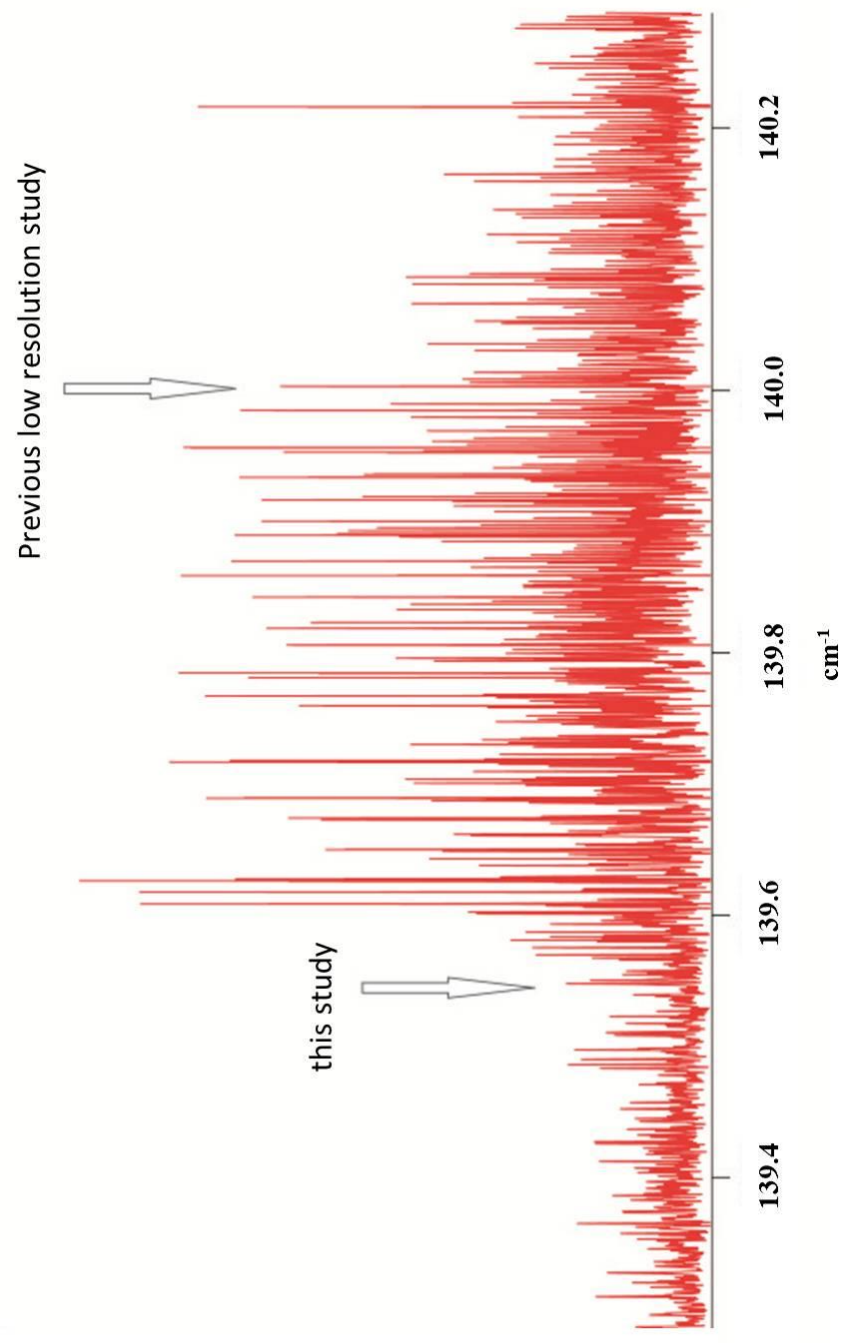
5.5.3.2 Vibrational dependence of rotational constants in the first four levels of the ring puckering mode

The rotational constants determined in this study for the ν_{21} ring puckering fundamental and first three hotbands are compared to those from the microwave experiment of Gibson and Harris.[4] The rotationally resolved infrared spectrum of the ν_{21} ring puckering mode of 3-oxetanone is described by three rotational constants and five centrifugal distortion constants as shown in Table 5.3. More importantly, all terms in the Hamiltonian model seem to be more physically meaningful compared to those in the early microwave work in which only three rotational constants were included in the analysis.[4]

The rotational constants from the fundamental and first three hotbands are plotted as a function of vibrational energy level in Figure 5.10 and reveal a linear relationship for each. This is consistent with a relatively harmonic single-well potential for the ring puckering mode of 3-oxetanone.[19, 20] The plot of the A rotational constants exhibits a rather large negative slope compared to those of B and C. This can be justified by considering the structure of the ring in its principal inertial axis system. The ring is divided by the *a*-axis through the two oxygen atoms (as seen in Figure 5.1). Higher excited vibrational states for the ring puckering mode result in geometries such that the two oxygen atoms are further away from the *a*-axis on average as the ring flexes. This would increase I_a and decrease the A rotational constant for higher ring puckering vibrational states. As for the increased B and C constants, this observation can be rationalized by the fact that the heavy atoms of the ring are, on average, closer to the *b*- and *c*- axes during the ring puckering motion in 3-oxetanone (as they move off the *a*-

Figure 5.10: Rotational constants plotted as a function of the vibrational energy levels of the ring puckering mode of 3-oxetanone.

The A/MHz plot shows data points with fit line $A_v = -46.98766v + 12128.6$, $R^2 = 0.99998$.

The B/MHz plot shows data points with fit line $B_v = 4.62593v + 4955.9$, $R^2 = 0.99792$.

The C/MHz plot shows data points with fit line $C_v = 9.58580v + 3686.8$, $R^2 = 0.99995$.
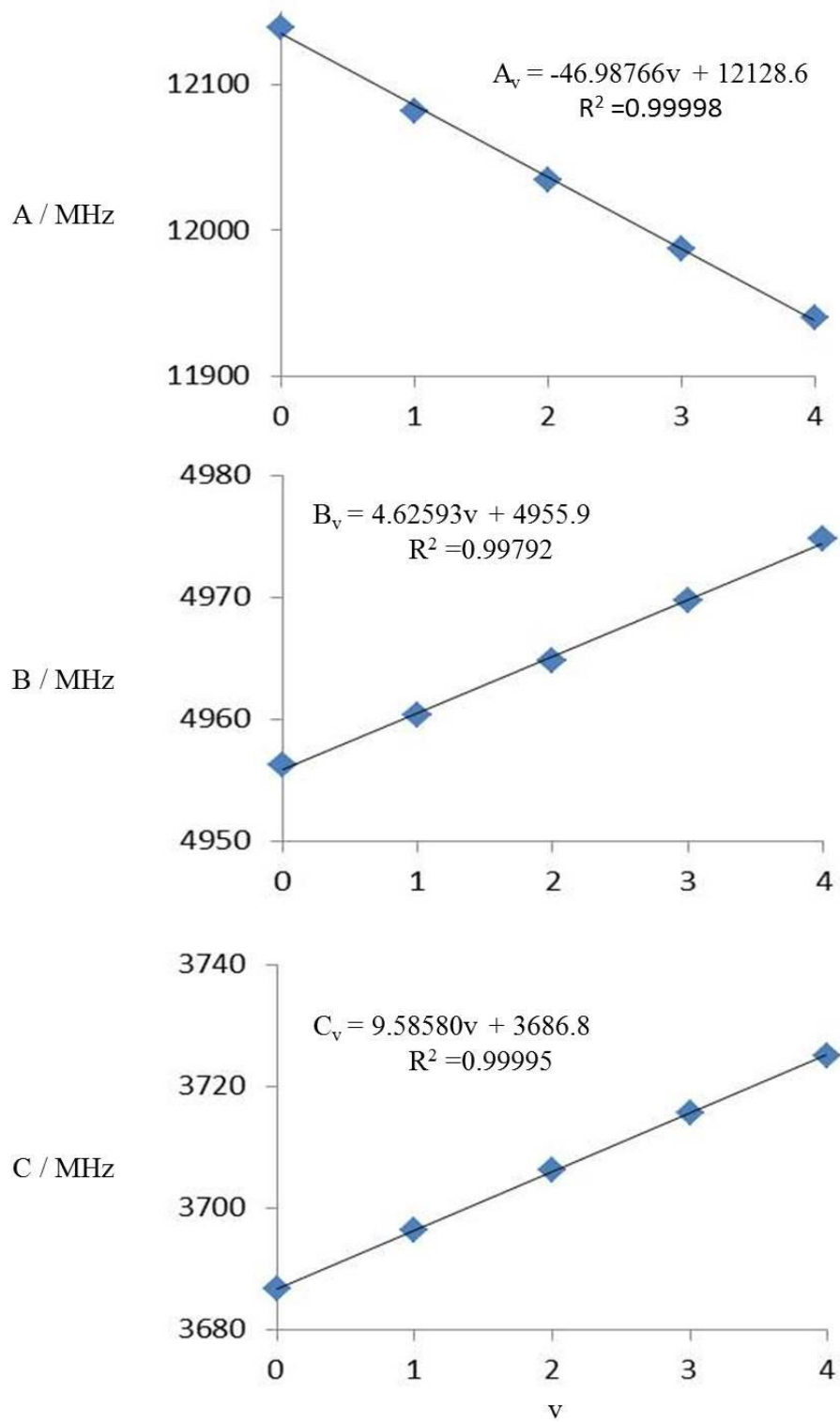
axis).

5.5.4 Determination of vibrational frequency

For the other low lying fundamental modes of the 3-oxetanone, the band origins of the ν_{20} (399.588606(6) cm^{-1}), ν_{16} (448.194670(5) cm^{-1}) and ν_7 (684.994728(7) cm^{-1}) modes were accurately determined for the first time via a simultaneous fit of 13556 assigned rovibrational transitions (including 3237 transitions from the ν_{21} ring puckering mode). They compare well with values reported by Durig (401 cm^{-1}, 448 cm^{-1} and 683 cm^{-1}).[6] The fact that this co-fit of more than thirteen thousand transitions across four different vibrational energy states has an exceptionally small rms error of 0.000108 cm^{-1} has illustrated the validity of the Hamiltonian model employed to accurately describe these rovibrational energy levels.

Both harmonic and anharmonic DFT calculations of the frequencies of the vibrational modes of 3-oxetanone are compared with those observed in this high resolution study in Table 5.5. Scaled harmonic frequencies based on an empirical scaling factor (0.9679)[11] were also included in the comparison. Generally, the determined band centers of the ν_{20} (399.588606(6) cm^{-1}), ν_{16} (448.194670(5) cm^{-1}) and ν_7 (684.994728(7) cm^{-1}) modes in this study compare well with the harmonic frequencies at the level of B3LYP/6-311++G (2d, 3p) (410, 449[a] and 688 cm^{-1}). The scaled harmonic (397, 434 and 666 cm^{-1}) and anharmonic frequencies (411, 444 and 680 cm^{-1}) provide roughly the same degree of agreement. Although the largest discrepancy is only ~15 cm^{-1}, the above comparison clearly shows that none of the calculation methods delivers a systematic,

---

[a] The underlined frequency indicates the closest prediction of that vibrational mode among the three calculation methods compared to the experimental value.

Table 5.5: Comparison of the experimentally observed infrared frequencies of 3-oxetanone in cm^{-1} with computational predictions (B3LYP/6-311++G(2d,3p)). Bands studied in this work are highlighted in bold.

Expt (Ref.[6])	Calc. harmonic	Calc. harmonic scaled[a]	Calc. anharmonic	Normal mode	Symmetry
2931[a]	3037	2936	2889	CH₂ sym str	A₁
1847	1888	1827	1851	C=O str	A₁
1457	1488	1440	1472	CH₂ scissoring	A₁
1134	1311	1269	1279	CH₂ wag	A₁
979	991	959	971	ring breathing	A₁
832	840	813	822	ring def	A₁
ν₇ 683	**688**	**666**	**680**	**ring def**	**A₁**
2962[c]	3081	2982	2927	CH₂ antisym str	A₂
1111[c]	1120	1084	1094	CH₂ twist	A₂
1102[c]	770	745	755	CH₂ rock	A₂
2924	3026	2929	2839	CH₂ sym str	B₂
1430	1461	1414	1425	CH₂ scissoring	B₂
1250[b]	1272	1231	1242	CH₂ wag	B₂
1076	1087	1052	1051	ring def	B₂
955[b]	991	958	958	ring def	B₂
ν₁₆ 448	**449**	**434**	**444**	**C=O def in-plane**	**B₂**
2956	3080	2981	2925	CH₂ antisym str	B₁
1284[b]	1158	1121	1131	CH₂ twist	B₁
1049	1070	1036	1048	CH₂ rock	B₁
ν₂₀ 401	**410**	**397**	**411**	**C=O def out-of-plane**	**B₁**
ν₂₁ 140	**149**	**135**	**158**	**Ring puckering**	**B₁**

[a] Scaled with a factor of 0.9679 from Ref.[11].
[b] From liquid IR spectrum.
[c] From liquid Raman spectrum.

121

reliable prediction of vibrational frequencies as each of the three provides the best calculated frequency of only one of the three bands. This observation is consistent with the DFT calculations of vibrational frequencies in β-propiolactone.

Furthermore, the v_{21} ring puckering mode of 3-oxetanone observed at 139.549148(5) cm^{-1} provides a rare opportunity to test the validity of theoretical modelling of this very low frequency vibrational mode which was not detectable in the case of β-propiolactone due to its low intensity. As it can be seen in Table 5.5, the scaled harmonic calculation gives the best match of frequency at 135 cm^{-1}. This is likely coincidental as the scaling factor used here was derived based mainly on high frequency stretching modes[11] and our observations have shown that this particular mode of 3-oxetanone has a nontrivial degree of anharmonicity in its potential function. Ironically, the anharmonic result (158 cm^{-1}) has the worst predicted frequency, despite the fact that it takes ~40 times longer to compute. Again, the combined experimental and theoretical studies of the vibrational frequencies of 3-oxetanone have shown that the modelling of low frequency, anharmonic vibrations still presents difficulties due to the lack of precise, widely-available methods.

5.6 Summary

The first rotationally resolved vibrational study of 3-oxetanone is reported here. By analyzing the high resolution infrared spectra collected using synchrotron light at the Canadian Light Source, 13556 rovibrational transitions from the v_{21}, v_{20}, v_{16} and v_7 fundamental vibrational modes were assignment and fit. Besides the accurate determination of spectroscopic parameters of the excited states including the band origins,

rotational and centrifugal distortion constants, the ground state of 3-oxetanone has been comprehensively characterized using GSCDs with the coverage of a broad range of energy levels. An a-type Coriolis coupling was identified between the two perpendicular C=O deformation modes and treated to account for the perturbed transitions. For the ν_{21} ring puckering mode, a total of 9165 transitions from the fundamental and first three hotbands were unambiguously assigned using lower and upper state combination differences. Among the accurate spectroscopic constants obtained from fitting the assigned transitions, precise band origins of the first four levels of the ring puckering vibration allowed the determination of the ring puckering potential function of 3-oxetanone in the form of $V = a\mathrm{x}^4 + b\mathrm{x}^2$ where $a = 2.04388 \times 10^5$ cm^{-1}/Å^4 and $b = 4.26392 \times 10^4$ cm^{-1}/Å^4. This model suggests that the ring puckering potential is flatter and less harmonic than previously thought. However, the linear trend in the rotational constant as a function of vibrational level shows that it is still fairly harmonic compared to other members of this four-membered heterocycle family.

References

[1] L. L. Combs and M. Rossie Jr., *J. Mol. Struct.* 32 (1976) 1-7.

[2] D. J. Pasto, D. M. Chipman and J. J. Worman, *J. Phys. Chem.* 86 (1982) 3981-3989.

[3] C. Thomson, *J. Mol. Struct.* 88 (1982) 55-60.

[4] J. S. Gibson, D. O. Harris, *J. Chem. Phys.* 57 (1972) 2318-2328.

[5] A. L. Meinzer and W. C. Pringle, *J. Phys. Chem.* 80 (1976) 1178-1180.

[6] J. R. Durig, A. C. Morrissey and W. C. Harris, *J. Mol. Struct.* 6 (1970) 375-390.

[7] L. A. Carreira and R. C. Lord, *J. Chem. Phys.* 51 (1969) 3225-3231.

[8] P. Vansteenkiste, V. Van Speybroeck, G. Verniest, N.t. De Kimpe and M. Waroquier, *J. Phys. Chem. A.* 111 (2007) 2797-2803.

[9] L. S. Rothman, I. E. Gordon, A. Barbe, D. Chris Benner, P. F. Bernath, M. Birk, V. Boudon, L. R. Brown, A. Campargue, J. -P. Champion, K. Chance, L. H. Coudert, V. Danaj, V. M. Devi, S. Fally, J. -M. Flaud, R. R. Gamache, A. Goldmanm, D. Jacquemart, I. Kleiner, N. Lacome, W. J. Lafferty, J. -Y. Mandin, S. T. Massie, S. N. Mikhailenko, C. E. Miller, N. Moazzen-Ahmadi, O. V. Naumenko, A. V. Nikitin, J. Orphal, V. I. Perevalov, A. Perrin, A. Predoi-Cross, C. P. Rinsland, M. Rotger, M. Šimečková, M. A. H. Smith, K. Sung, S. A. Tashkun, J. Tennyson, R. A. Toth, A. C. Vandaele and J. Vander Auwera, *J. Quant. Spectrosc. Radiat. Transfer.* 110 (2009) 533-572.

[10] Gaussian 03, Revision C.02, M. J. Frisch, G. W. Trucks, H. B. Schlegel, G. E. Scuseria, M. A. Robb, J. R. Cheeseman, J. A. Montgomery, Jr., T. Vreven, K. N. Kudin, J. C. Burant, J. M. Millam, S. S. Iyengar, J. Tomasi, V. Barone, B. Mennucci, M. Cossi, G. Scalmani, N. Rega, G. A. Petersson, H. Nakatsuji, M. Hada, M. Ehara, K. Toyota, R.

Fukuda, J. Hasegawa, M. Ishida, T. Nakajima, Y. Honda, O. Kitao, H. Nakai, M. Klene, X. Li, J. E. Knox, H. P. Hratchian, J. B. Cross, V. Bakken, C. Adamo, J. Jaramillo, R. Gomperts, R. E. Stratmann, O. Yazyev, A. J. Austin, R. Cammi, C. Pomelli, J. W. Ochterski, P. Y. Ayala, K. Morokuma, G. A. Voth, P. Salvador, J. J. Dannenberg, V. G. Zakrzewski, S. Dapprich, A. D. Daniels, M. C. Strain, O. Farkas, D. K. Malick, A. D. Rabuck, K. Raghavachari, J. B. Foresman, J. V. Ortiz, Q. Cui, A. G. Baboul, S. Clifford, J. Cioslowski, B. B. Stefanov, G. Liu, A. Liashenko, P. Piskorz, I. Komaromi, R. L. Martin, D. J. Fox, T. Keith, M. A. Al-Laham, C. Y. Peng, A. Nanayakkara, M. Challacombe, P. M. W. Gill, B. Johnson, W. Chen, M. W. Wong, C. Gonzalez and J. A. Pople, Gaussian, Inc., Wallingford CT, 2004.

[11] M. P. Andersson and P. Uvdal, *J. Phys. Chem. A* 109 (2005) 2937–2941.

[12] V. Barone, *J. Chem. Phys*. 120 (2004) 3059-3065.

[13] V. Barone, *J. Chem. Phys*. 122 (2005) 014108.

[14] H. M. Pickett, *J. Mol. Spectrosc*. 148, (1991) 371-377.

[15] C. F. Neese, Loomis-Wood Add-In (LWA) for Igor Pro, Version 2.0; 56th Ohio State University International Symposium on Molecular Spectroscopy, Columbus, OH, June 20−24, 2005, http:// fermi.uchicago.edu/freeware/LoomisWood.shtml.

[16] IGOR Pro Manual, WaveMetric Inc., Lake Oswego, OR USA (2008)

[17] I. M. Mills, *Pure Appl. Chem*.11(1965) 325-344.

[18] A. S. Gaylord and W. C. P. Pringle, Wesleyan University, (2012) Private communication.

[19] A.C. Legon, *Chem. Rev*. 80 (1980) 231-262.

[20] S. I. Chan, T. R. Borgers, J. W. Russell, H. L. Strauss and W. D. Gwinn, *J. Chem. Phys*. 44 (1966) 1103-1111.

Chapter 6

A high resolution study of the rovibrational spectra of azetidine[a]

6.1 Introduction

Unlike β-propiolactone and 3-oxetanone discussed in Chapters 4 and 5, which are planar due to carbonyl insertion to the ring, azetidine (c-C_3H_6N) has a puckered ring backbone and the –NH functional group can move between equatorial or axial positions as illustrated in Figure 6.1. This conformational ambiguity in azetidine makes it an interesting prototype of a flexible four-membered heterocycle for quantum mechanical modelling that has a greater degree of complexity than in the previous two cases. Particularly in this molecule, the low energy dynamics are influenced by the presence of two large amplitude vibrations (–NH inversion and ring puckering, shown in Figure 6.2) and the interaction between them. Thus, the examination of the low frequency vibrational modes of azetidine offers new insights into the characterization of the highly dynamic heterocyclic molecules.

As a result of the interesting dynamics, the potential energy functions of azetidine have been the subject of both experimental and theoretical investigation. The vibrational spectrum of azetidine was recorded in the gas phase,[1, 2] liquid phase[2, 3] and in a solid argon matrix.[4] Based on the infrared spectrum collected between 400 and 3400 cm^{-1} at low resolution and *ab initio* force field calculation results, Dutler and co-workers conducted a comprehensive vibrational study where the assignment of the normal modes

---

Figure 6.1: Structure of: a) azetidine in its principal axis system; b) equatorial conformer and c) axial conformer. The definition of the ring puckering (θ) and –NH inversion (β) angles are given graphically.
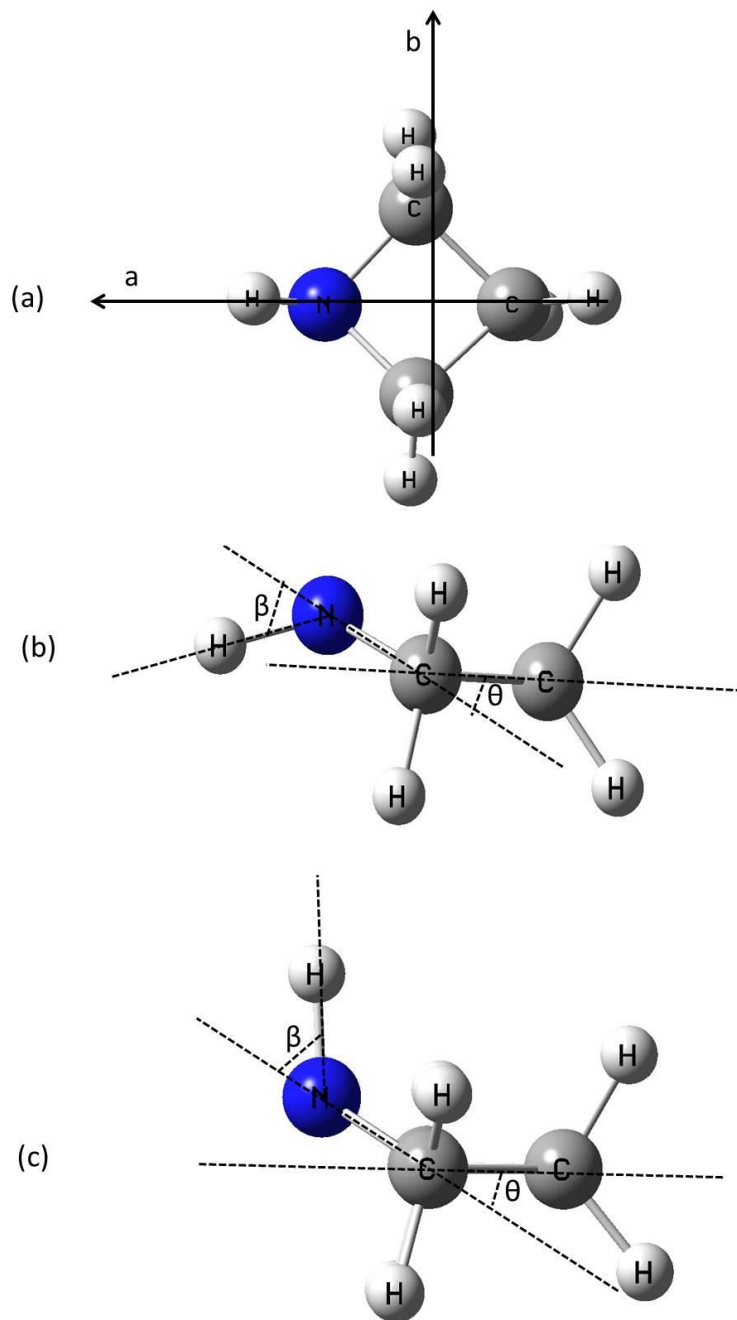
Figure 6.2: One dimensional potential energy functions of azetidine presented in: a) –NH inversion (β); b) ring puckering (θ) and c) the concerted ring puckering and –NH inversion (X=θ=τ) coordinates.

(a)

E

equatorial

axial

-NH inversion coordinate (β)

(b)

E

axial

equatorial

Ring puckering coordinate (θ)

(c)

E

C_{2v} barrier

equatorial

equatorial

Ring puckering + -NH inversion coordinate (X=θ= β)
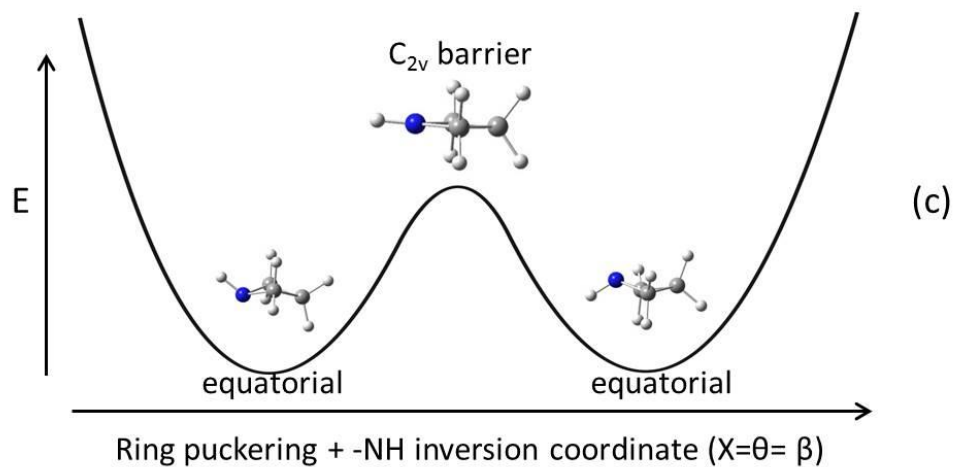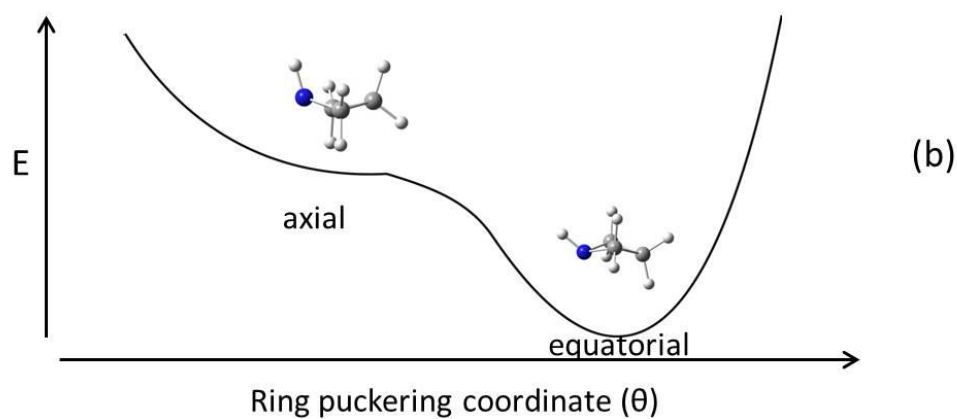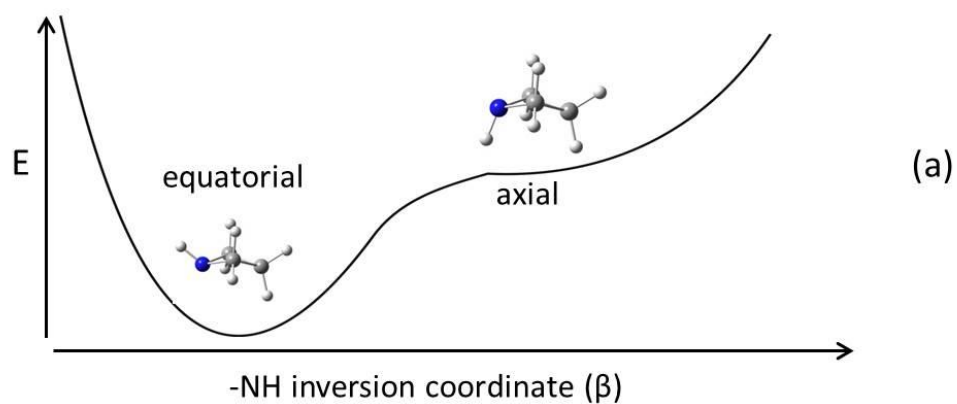
was established.[2]

As the most characteristic vibrational motion in four-membered heterocycles, the ring puckering mode of azetidine has been investigated extensively using microwave and infrared spectroscopic techniques as well as theoretical calculations. The results showed disagreement about the form of its potential energy function. Carreira and Lord [5] measured the low resolution far infrared spectrum corresponding to the ν_{16} puckering manifold and initially fit the fundamental along with hot bands to an asymmetric double well potential function with minima corresponding to a puckered ring backbone with the amine hydrogen atom in either an equatorial or axial position. The barrier to interconversion between the two conformers was predicted to lie 441 cm^{-1} above the lower minimum which was assumed to correspond to the equatorial structure. The energy of the two conformers are separated by 95 cm^{-1}.[5] Later, the results from a re-analysis of the far infrared data by Robiette *et al.* showed better agreement with a single well asymmetric potential function with the equatorial conformer being the only stable structure.[6] Subsequent investigations including *ab initio* calculations,[7, 8] a Raman study[9] and a more recent low resolution far infrared study are qualitatively consistent with this potential function.[10]

The structural parameters of azetidine were determined in a combined microwave and electron diffraction study by Günther and co-workers in which the presence of the equatorial conformer was confirmed along with a ring puckering angle of 29.7°.[1] Later, López *et al.* measured the pure rotational transitions via high resolution FTMW spectroscopy in multiple vibrational states of the ring puckering manifold and a tunnelling doubling was observed.[11] Combined with *ab initio* calculations, they

investigated the potential function along both the ring puckering (θ) and $-$NH inversion (β) coordinates. Their *ab initio* calculations suggest that azetidine has: a) asymmetric single well potential functions along the pure $-$NH inversion ($\theta=0$ and $\beta\neq0$) and pure ring puckering ($\theta\neq0$ and $\beta=0$) coordinates as shown in Figure 6.2 (a) and (b), respectively; b) a symmetric double well potential function along the coordinate of involving both the $-$NH inversion and ring puckering vibrations (along the diagonal of the potential energy surfaces defined by θ and β, i.e. $\theta=\beta$). The shape of the potential function is qualitatively shown in Figure 6.2(c) and has an estimated barrier of 1900-2600 cm^{-1} through an intermediate with C_{2v} symmetry. The observed tunnelling splitting in the microwave region was attributed to the coupling between the ring puckering and $-$NH inversion motions along this combined coordinate.[12]

In this chapter, the assignment and analysis of three rotationally-resolved vibrational bands including the ν_{14} (β-CH$_2$ rocking), ν_{15} (ring deformation) and ν_{16} (ring puckering) motions of azetidine are reported. For the first time, the band origins of the three lowest vibrational modes of azetidine were accurately determined and compared with results of previous theoretical calculations. The analysis of the rotational structures of the ν_{14} and ν_{15} bands revealed the existence of transitions obeying both *a*- and *c*- type selections rules suggesting that these vibrational modes are coupled to $-$NH inversion tunnelling. In contrast, only *a*-type transitions were observed in the ν_{16} band. The global analysis of assigned transitions from these bands enabled the precise characterization of the lowest three vibrational states of azetidine and thus, provided detailed information about the vibrational energy landscape of this highly fluxional molecule.

6.2 Experimental details

The far infrared spectra of azetidine were recorded at the Canadian Light Source (CLS) using a synchrotron based Fourier transform infrared (FTIR) spectrometer as described in Chapter 3. The gas sample was prepared by introducing vapour pressure from a liquid sample (98% purity, Sigma-Aldrich) into a gas cell. Instead of the 2 m multipass gas cell (physical dimension, capable of providing up to 72 m total absorption pathlength) used in the studies reported in Chapters 4 and 5, a smaller, 30 cm White cell set to a total absorption pathlength of 7 m was used due to the expensive cost of the azetidine sample (~ $1000 /ml).

Data for the ν_{14}, ν_{15} and ν_{16} bands were recorded in two different spectral windows due to the different specifications of the required optical system of the interferometer. In the lower region of 100-350 cm^{-1}, the spectrometer was equipped with a 6 μm Mylar beamsplitter and a helium-cooled Si bolometer detector. For the ν_{16} band in this region, a sample pressure of 700 mTorr was maintained during the data acquisition and 17 separate interferograms were obtained. For the ν_{14} and ν_{15} bands between 500 and 850 cm^{-1}, 60 mTorr sample pressure was used with the spectrometer outfitted with a KBr beamsplitter, a GeCu detector and an optical filter (490-1190 cm^{-1}). A total of 112 separate interferograms were recorded in this spectral region. The instrument was set to collect spectra at the highest spectral resolution of 0.000959 cm^{-1} for both windows. Key experimental parameters are summarized in Table 6.1.

The final spectra were calibrated in the two spectral windows mentioned above separately. Residual water lines observed in the 130-300 cm^{-1} region were compared with those in the HITRAN database.[13] In the higher spectral window, CO_2 lines at ~667 cm^{-1}

Table 6.1: Experimental parameters of recorded bands of azetidine.

	ν_{14}	ν_{15}	ν_{16}
Band origin (cm^{-1})	736.7	648.1	207.7
Pressure (mTorr)		60	700
No. of interferograms collected		112	17
Time spent to record interferograms (h)		13	3
Resolution (cm^{-1})		0.00096	
Lines used in calibration		CO_2 around 667 cm^{-1}	H_2O 130-300 cm^{-1}

were used for calibration in the same way. Generally, it was found that the measured frequencies were accurate to within 0.0001 cm^{-1} and 0.0007 cm^{-1} for the lower and higher spectral windows, respectively.

6.3 Spectral assignment and analysis

The combined microwave and electron diffraction study by Günther *et al.*[1] showed that the ground state structure of azetidine has a puckered ring skeleton with a ring puckering angle (θ) of 29.7° relative to the *ab*-plane of the molecule as shown in Figure 6.1 (a). In the microwave study of the ground state and several ring puckering excited states of azetidine by López and co-workers,[11] tunnelling splittings due to –NH inversion coupled to the ring puckering vibration were observed. The double well potential in Figure 6.2 (c) gives rise to a splitting of vibrational states below the barrier. Based on their high quality microwave spectrum, two sets of spectroscopic constants were established for the ground vibrational state as a result of this splitting which are labelled 0^+ and 0^- in which the added superscript describes the symmetry of the –NH

inversion component of the wavefunction. However, based on the similarity of the spectroscopic constants for states 0^+ and 0^-, the analogous splitting in the far infrared spectrum is below the resolution of any FTIR spectrometer.

In such flexible molecules, it is often necessary to consider the large amplitude motions when describing the selection rules that govern the allowed transitions. This permits the treatment of tunnelling splittings and of transition types which would not be observed in the absence of tunnelling. In the case of azetidine, the point group classification is C_s but when one considers the possibility of –NH inversion, the molecule belongs to the C_{2v} molecular symmetry group.[11] Molecular symmetry group theory and its application to flexible molecules is treated in detail by Bunker and Jensen[14] and was used in Ref. [11] to describe the relevant symmetry features of azetidine for the microwave spectrum.

Based on the C_{2v} molecular symmetry group, the –NH inversion motion has B_1 symmetry (Γ_{inv}) and thus the tunnelling split states (such as 0^+ and 0^-) have a symmetric component with A_1 inversion symmetry and an antisymmetric component with B_1 inversion symmetry. The three excited vibrational states in the current study have B_1 symmetry (Γ_{vib}) and significant –NH out-of-plane character [2, 11] which facilitates coupling of these vibrations to the –NH inversion motion. The symmetry of the rotational part of the wavefunction (Γ_{rot}) depends on the even (e)/odd(o) nature of the K_a and K_c quantum numbers. For azetidine, the rotational energy levels have the following symmetries: $A_1(ee)$, $A_2(eo)$, $B_1(oo)$ and $B_2(oe)$ for various combinations of (K_aK_c).

The allowed transitions are governed by the product of the symmetries of the rotational, vibrational and inversion parts of the wavefunction ($\Gamma_{rot} \times \Gamma_{vib} \times \Gamma_{inv}$) for each

state. The product of the wavefunctions for the upper and lower states must contain the totally symmetric (A_1) representation when combined with the symmetry of the space-fixed molecular dipole moment (A_2). Considering this, there are two possibilities as shown in Figure 6.3: a-type rotation-vibration-inversion transitions between rotational levels of $eo \leftrightarrow ee$ and $oe \leftrightarrow oo$ symmetries and c-type rotation-vibration transitions between rotational levels of $ee \leftrightarrow oe$ and $oo \leftrightarrow eo$ symmetries. Thus, although the resolution of the spectrometer may be insufficient to resolve two closely spaced sets of transitions originating from the tunnelling split ground state (0^+ and 0^-), the possibility of transitions that cross inversion states (a-types) are indicative of the presence of –NH inversion tunnelling.

Initially, the observed rovibrational transitions in the ν_{14}, ν_{15} and ν_{16} bands of azetidine were assigned and fit separately. Ultimately, transitions assigned in the individual analyses of all three bands were fit simultaneously in a global analysis using Watson's A-reduced Hamiltonian in I^r representation in Pickett's SPFIT program[15] to obtain a complete set of spectroscopic constants for these states. The assignment and analyses of the rovibrational spectra of azetidine are detailed below.

6.3.1 Infrared spectrum of the ν_{16} band

The ν_{16} ring puckering mode has B_1 symmetry and as described above, may involve a-type and c-type transitions. Centered at ~207 cm^{-1} as shown in Figure 6.4, this band is isolated from other vibrational modes, making it a good candidate to start the rovibrational analysis. The overall band contour is that of an a-type band and a closer look at the rotational structure reveals a series of regularly spaced patterns. These a-type

Figure 6.3: A schematic of transitions expected in the spectra of out-of-plane modes coupled with –NH inversion in azetidine. Rotational levels of each vibrational state are labelled to reflect rotation-inversion-vibration symmetry. Solid and dashed lines indicate the allowed c-type and a-type transitions, respectively. e (o) indicates even (odd) of K_a or K_c value. Note that relative energy differences between states are not to scale.
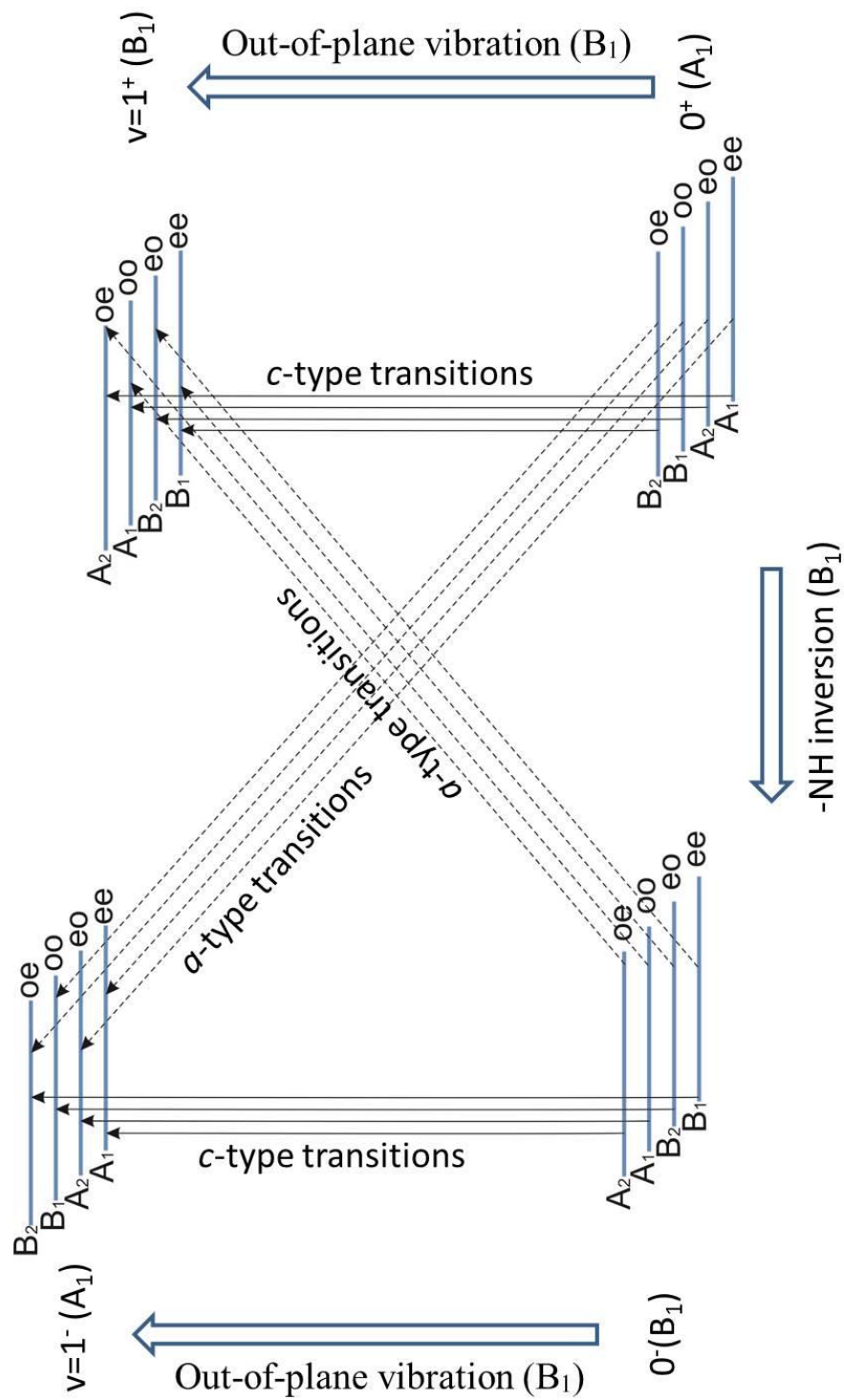
Figure 6.4: An overview spectrum showing the *a*-type band structure of the v_{16} band of azetidine at $\sim$207 cm^{-1}.

137
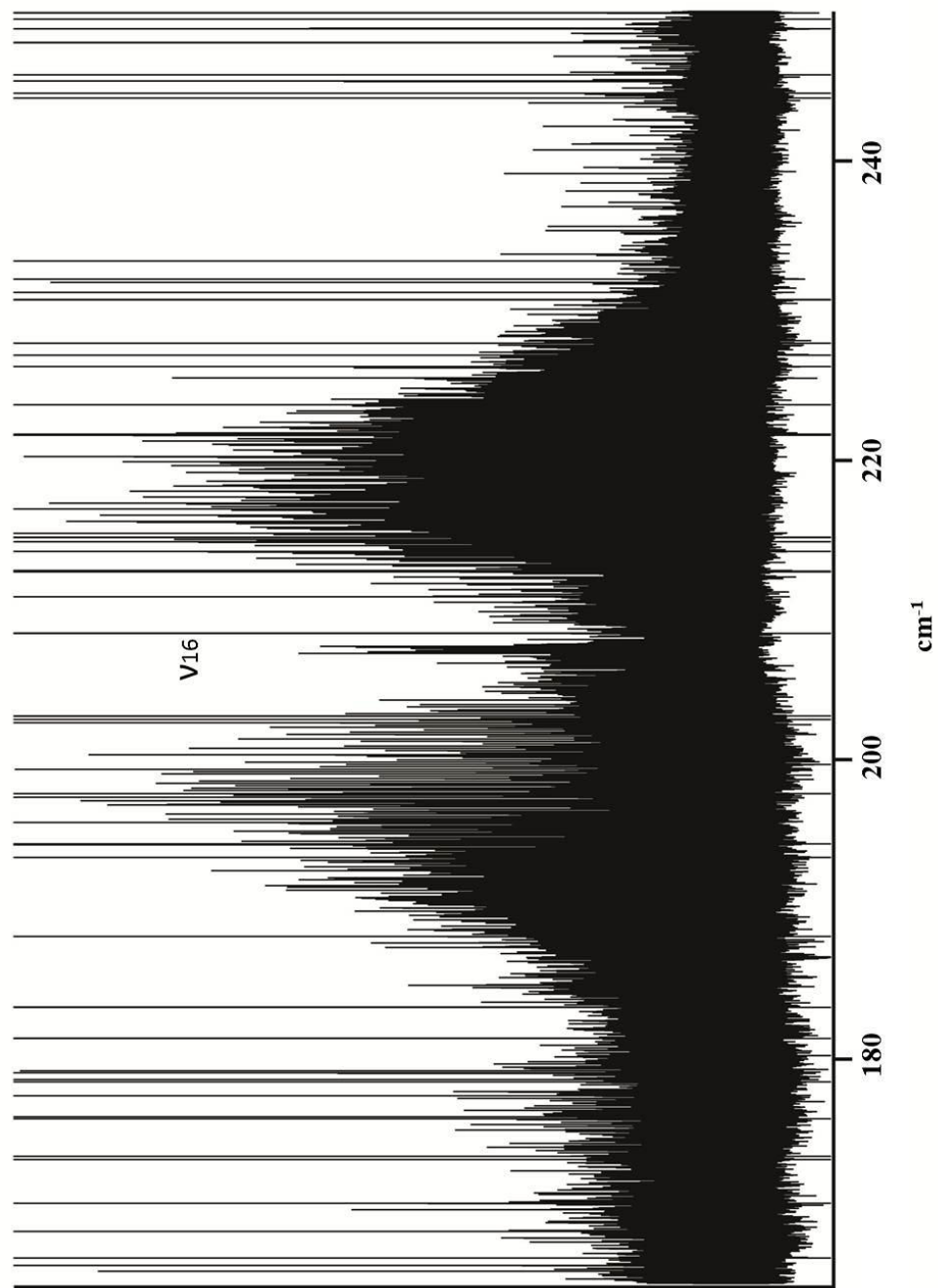
progressions were then compared with the simulated spectrum based on the ground state constants from Ref. [11] and the estimated band origin from Ref. [2]. This comparison led to the tentative assignment of a few strong transitions in each progression that was confirmed by ground state combination differences. Figure 6.5 shows such leading transitions in the R branch following the trend $\Delta J = +1$, $\Delta K_a = 0$ and $\Delta K_c = +1$ toward the band center (lower frequency side). The simulated spectrum was refined after the addition of the newly assigned transitions and the process continued in an iterative fashion until the strongest transitions were assigned.

A line list of assigned transitions for the ν_{16} band was compiled including 2350 a-type transitions from the P and R branches and 928 transitions from the Q branch. Rotational energy levels with J from 4 through 55 were covered in the P and R branches while the assignment in the Q branch accounted for transitions between $K_c = 5$ and 32 with J up to 46. All 3278 a-type transitions were fit using Watson's A-reduced Hamiltonian in I^r representation in Pickett's SPFIT program[15] and a set of spectroscopic constants including the band origin, ground state and excited state rotational constants and centrifugal distortion constants were determined. These accurately determined constants were used to predict line positions of c-type transitions, which are allowed by symmetry, but no such transitions were found in the observed spectrum.

6.3.2 Infrared spectrum of the ν_{14} band

The ν_{14} band of azetidine is attributed mainly to the β-CH_2 rocking motion with B_1 symmetry and follows the same selection rules as the ν_{16} band. Figure 6.6 shows an overview of the ν_{14} band at ~ 736 cm^{-1} alongside the ν_{15} band at ~ 648 cm^{-1}, which both

Figure 6.5: A section of the R branch of the ν_{16} band of azetidine showing the rotational structure.

cm^{-1}

215.7   215.9   216.1   216.3

20 1 20 19 1 19
20 0 20 19 0 19

19 2 18 18 2 17
19 1 18 18 1 17

18 3 16 17 3 15
18 2 16 17 2 15

17 4 14 16 4 13
17 3 14 16 3 13

16 5 12 15 5 11
16 4 12 15 4 11

19 1 19 18 1 18
19 0 19 18 0 18   15 6 10 14 6 9
                         15 5 10 14 5 9

18 2 18 17 2 16
18 1 17 17 1 16
                  14 7 8 13 7 7
                  14 6 8 13 6 7

17 3 15 16 3 14
17 2 15 16 2 14
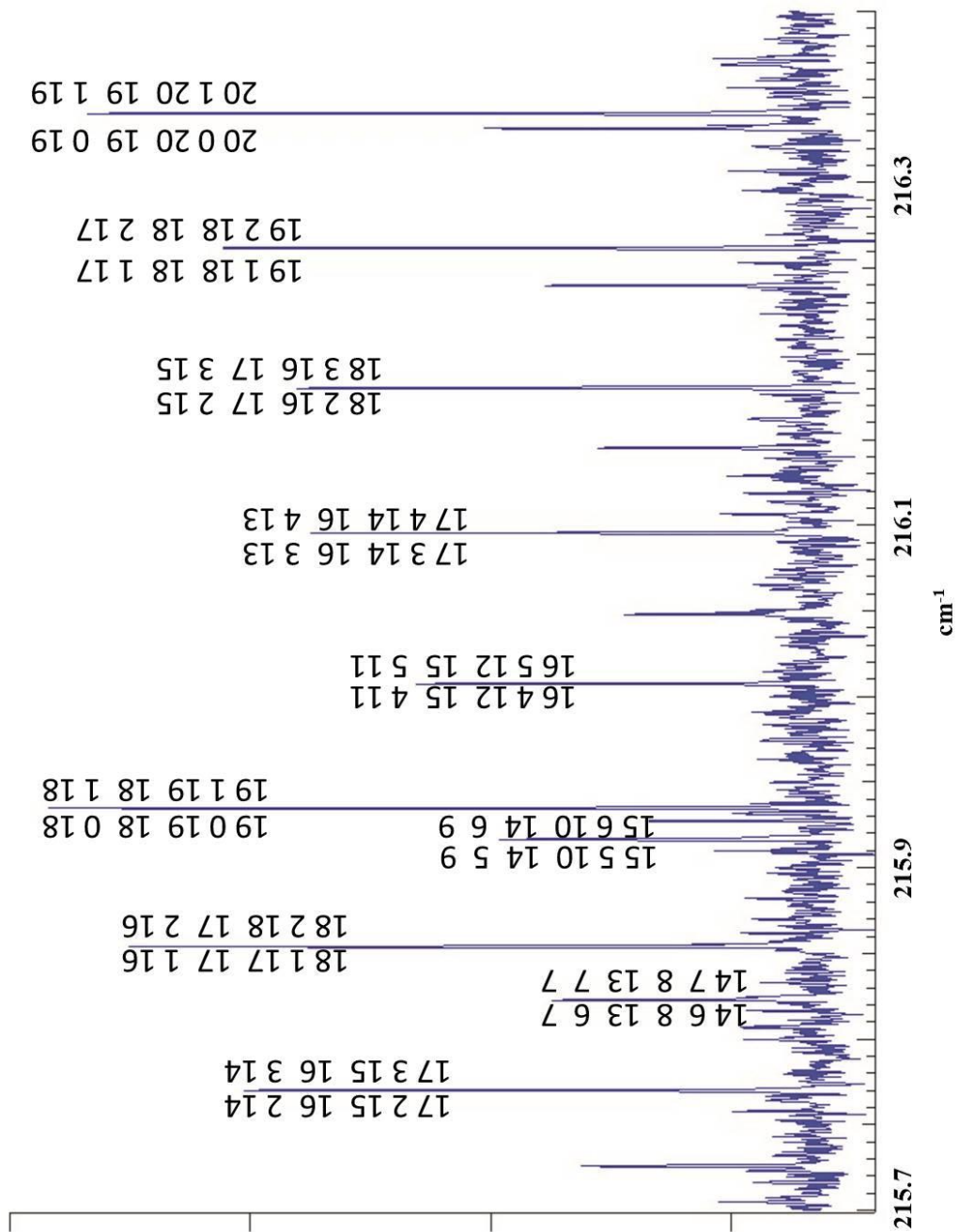
Figure 6.6: An overview spectrum showing the *a*-type band contours of the v_{14} and v_{15} bands of azetidine at ~648 and ~737 cm^{-1}, respectively.
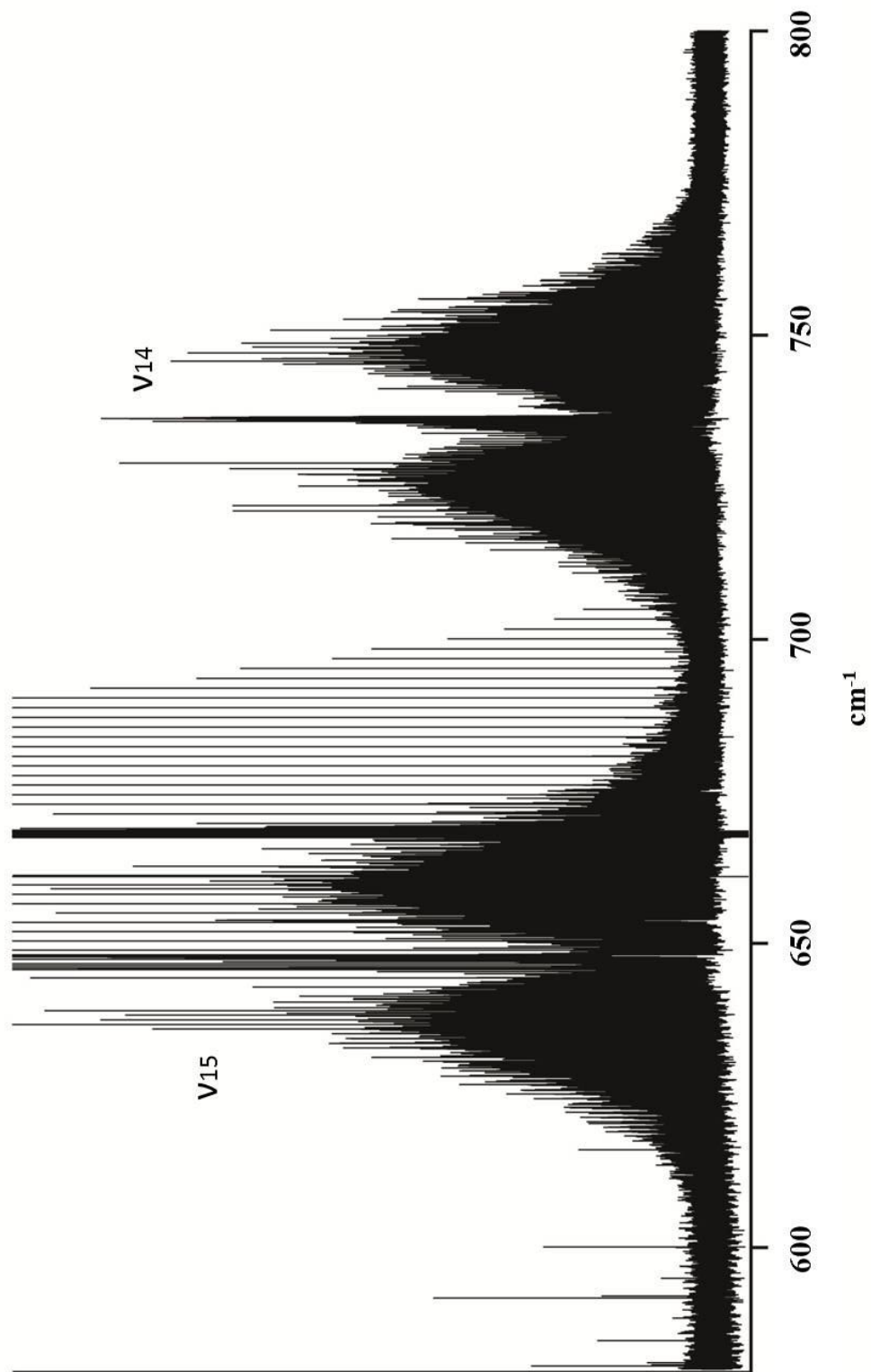
exhibit characteristic *a*-type band contours. A similar assignment scheme as described previously was applied to the observed transitions of the ν_{14} band. A total of 3333 *a*-type rovibrational transitions were assigned including 902 from the Q branch. The spanned quantum numbers of assigned transitions include those in the P and R branch from J=5 through 55. For the Q branch, transitions were assigned with K_a between 5 and 33 and J up to 46. The resulting spectroscopic constants from fitting the *a*-type transitions allowed the assignment of clusters of lower intensity spectral lines which turned out to be *c*-type progressions of this mode. An additional 3071 *c*-type transitions (2565 P/R and 506 Q) were assigned and added to the *a*-type line list to yield a set of constants that have taken both *a*-and *c*- type transitions into account. This provides a broad coverage of energy levels and hence the spectroscopic parameters are better determined.

6.3.3 Infrared spectrum of the ν_{15} band

The ν_{15} ring deformation mode at ~648 cm^{-1} has B$_1$ symmetry, giving rise to transitions following the same selection rules as the two bands discussed previously. Using the above mentioned assignment method, a total of 2130 *a*-type transitions were assigned including 250 from the Q branch. In the end, P and R branch energy levels ranging from J=6 to 47 were covered while transitions from $K_c = 4$ to 25 with J (max) = 40 in the Q branch were assigned. Compared to the other two bands, fewer transitions were assigned in the Q branch. Most of unassigned transitions are those of selection rules $\Delta J = 0$, $\Delta K_a = 0$, $\Delta K_c = \pm 1$ and their spectra were not resolved in some spectral regions as shown in Figure 6.7, which is not the case for the other two bands. Similar to the ν_{14} mode, lower intensity *c*-type transitions were identified using the predictions based on the

Figure 6.7: A detailed section of the Q branch of the ν_{15} band of azetidine. On top, the

transitions are assigned readily for a range of J levels; at the bottom, the transitions are

not resolved while the dotted lines indicate their predicated frequencies.
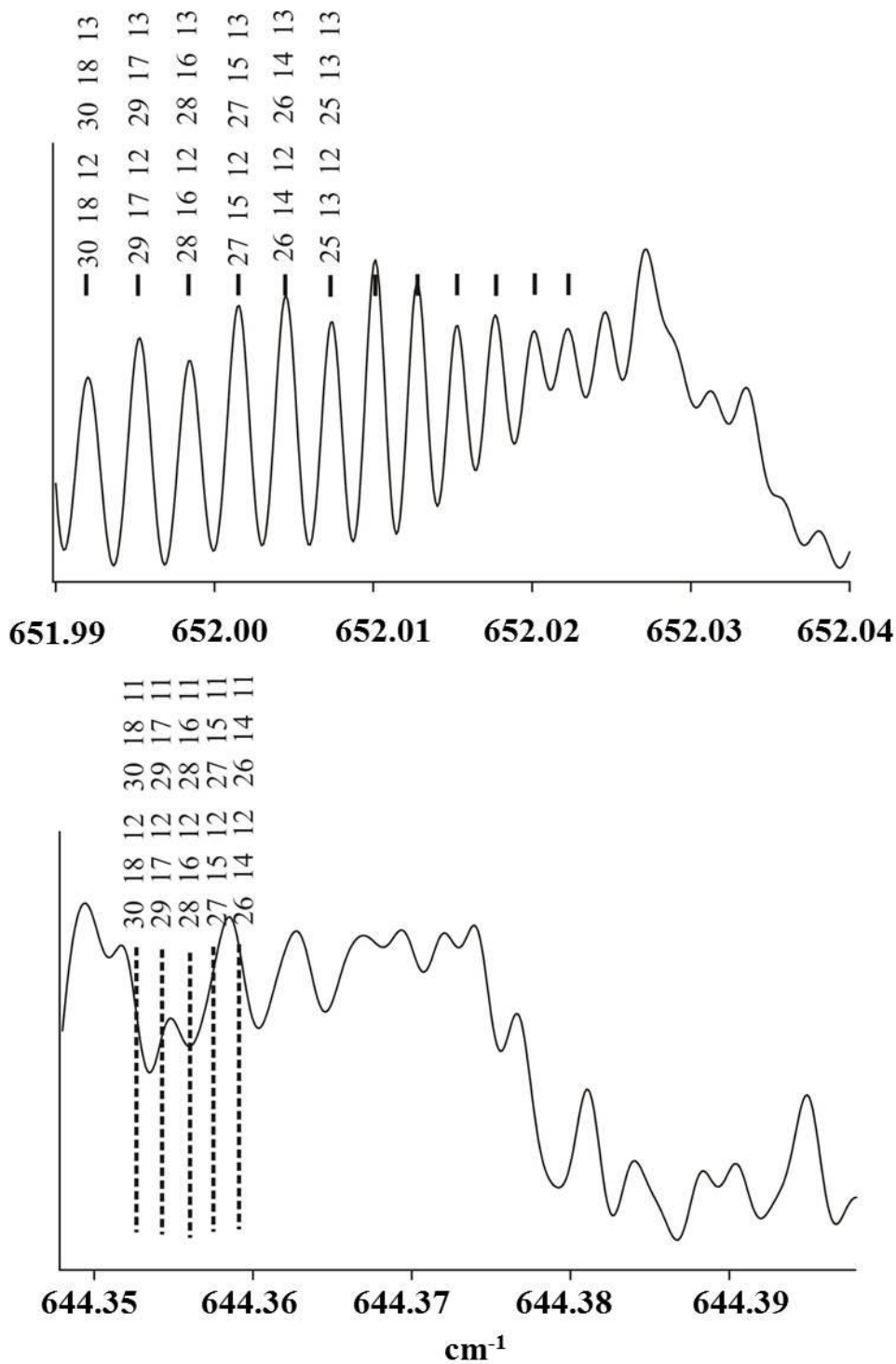
assignment of *a*-type transitions. As a result, 2464 *c*-type transitions (2060 P/R and 404 Q) were added to the fit and ultimately a set of constants for the ν_{14} mode were determined from both *a*- and *c*-type transitions.

6.3.4 Global analysis

A global fit which incorporated a total of 14276 rovibrational transitions from the ν_{14}, ν_{15} and ν_{16} bands of azetidine was performed in Pickett's SPFIT program using Watson's A-reduced Hamiltonian, I^r-representation[15] and the resulting spectroscopic constants are listed in Table 6.2. Note that in the absence of any evidence of perturbation, the ground state parameters were not independently determined via ground state combination differences and the overall spectroscopic parameters were consistent in sign and magnitude across the states under study.

Table 6.2: Spectroscopic constants for the ground state, ν_{14}, ν_{15} and ν_{16} states of azetidine.

	Ground state	ν_{14}	ν_{15}	ν_{16}
ν / cm^{-1}		736.701310(7)	648.116041(8)	207.727053(9)
Rotational constants / cm^{-1}				
A	0.3820335(4)	0.38088655(48)	0.3817851(4)	0.3812410(12)
B	0.3782355(4)	0.37845869(46)	0.3783896(4)	0.3776991(11)
C	0.22055364 (10)	0.21967532(10)	0.22007381(10)	0.21967045(10)
Centrifugal distortion constants / 10^{-9} cm^{-1}				
Δ_J	163.4(3)	169.5(5)	156.3(4)	140.6(12)
Δ_{JK}	-164.6(16)	-197 (2)	-145.5(20)	-81.(9)
Δ_K	220.1(19)	239.1(19)	226.6(20)	195.(9)
δ_j	48.32(16)	52.7(3)	45.36(19)	37.6(6)
δ_k	41.2(5)	35.3(6)	41.7(6)	46.6(3)
rms error / cm^{-1}		0.000154		

6.4. Discussion

6.4.1 The ground state of azetidine

In the microwave study of azetidine by López et al.[11], the observed pure rotational transitions were doubled and treated as two separate states within the ground vibrational state. These were labelled as symmetric (+) and antisymmetric (-) tunnelling states corresponding to the interconversion of azetidine between equivalent equatorial structures as shown in Figure 6.2 (c). Their reported spectroscopic constants for the 0^+ and 0^- are essentially the same to within the reported uncertainties (0.4 kHz or 1.3×10^{-9} cm^{-1}) and thus, the same tunnelling splittings (i.e. two closely spaced sets of a-type or c-type transitions) were well below the resolution of even the best FTIR instrument. Generally, the ground state rotational constants determined in the present far infrared

study compare well with those from the pure rotational study in Ref. [11]. Only small discrepancies were found when comparing rotational constants for the ν_{16} ring puckering state (~0.00024 cm^{-1} for A and B) and this is likely due to the fact that the two analyses involved different data sets (numbers of transitions, energy level coverage) with different sensitivity to parameters in the Hamiltonian model. Based on the high degree of consistency between the ground state spectroscopic constants with the results in Ref. [11], the same equatorial conformer of azetidine was observed in both studies. Due to the multiplex advantage of FTIR, it can be further confirmed that this equatorial conformer is the only stable geometry as no additional transitions attributable to the axial conformer were observed.

6.4.2 Symmetry considerations in rovibrational analysis

The current work shows that the ν_{14} and ν_{15} bands exhibit both *a*- and *c*-type transitions in their infrared spectra, which is not surprising as both modes have a considerable –NH out-of-plane component according to the *ab initio* force field calculation in Ref. [2] that suggested that the ν_{14} and ν_{15} bands contain 40% and 30% –NH out-of-plane bending character, respectively. This unusual observation of rovibrational transitions with mixed selection rules within the same vibrational band indicates that low frequency modes cannot be adequately described by a single normal mode such as C–H stretching, CH_2-rocking, twisting, etc. as is typical when interpreting higher frequency motions. Instead, vibrational modes in the far infrared region often involve large amplitude motion of multiple nuclei and this requires the use of molecular

symmetry group theory to account for the states observed due to the highly dynamic nature of these molecules.

A similar combined a- and c-type spectrum was not found in the region of the ν_{16} ring puckering mode. The overview of the ν_{16} band as shown in Figure 6.4 is dominated by strong a-type features and so is the detailed spectrum in Figure 6.5. It should be noted that based on the symmetry considerations described in Figure 6.3, the rotationally resolved far infrared data clearly supports the presence of coupling between the ring puckering vibration and –NH inversion motion and the observed a-type transitions are those that cross states of different inversion symmetry. Based on the quality of the microwave investigation in Ref. [11] which provides clear evidence of this coupling, it can be asserted that the absence of c-type transitions in the current infrared work is due to insufficient intensity compared to the dominant a-type features. Although DFT frequency calculations show that the intensity of the ν_{16} mode is 1/7 that of the ν_{15} mode observed here, these calculations are based on C_s symmetry without accounting for the complex – NH inversion tunnelling dynamics. In other words, standard computational predictions do not provide information pertaining to the nature of the band intensity in such fluxional molecules, i.e. how the intensity differs for vibration-rotation versus vibration-rotation-inversion transitions. If the molecular geometry is constrained to be C_{2v} symmetry to include the –NH inversion tunnelling nature, the frequency calculations lose meaning as this is not a stable structure but rather corresponds to a saddle point on the potential energy surface.

6.4.3 Band origins of the v_{14}, v_{15} and v_{16} bands

The band centers of the v_{14} (736.701310(7) cm^{-1}), v_{15} (648.116041(8) cm^{-1}) and v_{16} (207.727053(9) cm^{-1}) bands were accurately determined for the first time in the current study and compare well with previously reported values from low resolution infrared studies.[1, 2, 6, 10] These experimental values may also be compared with *ab initio* calculations of the vibrational frequencies of azetidine. Surprisingly, the predicted frequencies of the band origins using the scaled *ab initio* force field calculations of Dutler *et al.*[2] (739.4, 636.6 and 198.7 cm^{-1}, respectively) seem to be fairly close to experimental results. However, the authors themselves admitted that this agreement, especially for the ring puckering mode, was likely fortuitous as such anharmonic modes cannot be modelled realistically with harmonic force field calculations. Thompson *et al.* reported the calculated frequencies at the level of DFT (B3LYP (6–31G**)) which are 748.7, 657.1 and 212 cm^{-1}, respectively.[4] Palafox *et al.* predicted the vibrational frequencies using B3LYP (6–311++G(2d,p)) calculations and showed that the estimate of the ring puckering mode improves (206 cm^{-1}) with the use of a larger basis set, but the agreement for the v_{14} mode actually worsens with the expanded basis (and the authors have not reported the v_{15} frequency).[16] It can be seen from the above comparison between experimental and theoretical values that there is no systematic way to gauge the accuracy of predicting vibrational frequencies in this four-membered heterocycle. As in Chapters 4 and 5, this highlights the importance of obtaining high quality data in the far infrared region from high resolution spectroscopy to test and improve theoretical models.

6.5 Summary

The vibrational spectra of the ν_{14} (β-CH_2 rocking), ν_{15} (ring deformation) and ν_{16} (ring puckering) modes of azetidine were studied at high resolution for the first time. A total of 14276 rovibrational transitions corresponding to these three modes were analyzed using a Hamiltonian model and a set of spectroscopic constants were precisely determined. This investigation confirms an asymmetric single well potential for azetidine as no evidence of an axial conformer was observed. Both *a*- and *c*-type transitions in the ν_{14} and ν_{15} bands were observed and analyzed using the C_{2v} molecular symmetry group. The analysis confirms that these vibrations couple to the –NH inversion motion. The scheme described in this chapter illustrates an example of using bright synchrotron light to resolve the fine spectral details of low frequency vibrations that involve the presence of a large amplitude motion (–NH inversion). A similar scheme was employed in the rovibrational analysis of silacyclobutane (with an observed quantum mechanical tunnelling splitting within the resolution limits of the FTIR instrument) and will be detailed in the next chapter.

References

[1] H. Günther, G. Schrem and H. Oberhammer, *J. Mol. Spectrosc.* 104 (1984) 152-164.

[2] R. Dutler, A. Rauk and R. A. Shaw, *J. Phys. Chem.* 94 (1990) 118-124.

[3] M. A. Palafox, N. Iza, M. Gil and J. L. Núñez, *Int. J. Quantum Chem.* 89 (2002) 25-47.

[4] C. A. Thompson, R. C. Mowrey and T. P. Russel, *J. Mol. Struct.* (THEOCHEM) 491 (1999) 67-80.

[5] L. A. Carreira and R. C. Lord, *J. Chem.Phys.* 51 (1969) 2735-2744.

[6] A. G. Robiette, T. R. Borgers and H. L. Strauss, *Mol. Phys.* 42 (1981) 1519-1524.

[7] D. Cremer, O. V. Dorofeeva and V. S. Mastryukov, *J. Mol. Struct.* 75 (1981) 225-240.

[8] R. N. Skancke, G. Fogarasi and J. E. Boggs, *J. Mol. Struct.* 62 (1980) 259-273.

[9] D. F. Bocian, G. A. Schick and R. R. Birge, *J. Chem.Phys.* 75 (1981) 2626-2634.

[10] T. Egawa and K. Kuchitsu, *J. Mol. Spectrosc.* 128 (1988) 469-477.

[11] J. C. López, S. Blanco, A. Lessari and J. L. Alonso, *J. Chem. Phys.* 114 (2001) 2237-2350.

[12] M. A. Harthcock and J. Laane, *J. Chem. Phys*, 79 (1983) 2103-2113.

[13] L. S. Rothman, I. E. Gordon, A. Barbe, D. Chris Benner, P. F. Bernath, M. Birk, V. Boudon, L. R. Brown, A. Campargue, J. -P. Champion, K. Chance, L. H. Coudert, V. Danaj, V. M. Devi, S. Fally, J. -M. Flaud, R. R. Gamache, A. Goldmanm, D. Jacquemart, I. Kleiner, N. Lacome, W. J. Lafferty, J. -Y. Mandin, S. T. Massie, S. N. Mikhailenko, C.

E. Miller, N. Moazzen-Ahmadi, O. V. Naumenko, A. V. Nikitin, J. Orphal, V. I. Perevalov, A. Perrin, A. Predoi-Cross, C. P. Rinsland, M. Rotger, M. Šimečková, M. A. H. Smith, K. Sung, S. A. Tashkun, J. Tennyson, R. A. Toth, A. C. Vandaele and J. Vander Auwera, *J. Quant. Spectrosc. Radiat. Transfer*. 110 (2009) 533-572.

[14] P. R. Bunker and P. Jensen, *Molecular Symmetry and Spectroscopy. 2nd edition.* NRC Research Press, Ottawa, Ontario, Canada (2006).

[15] H. M. Pickett, *J. Mol. Spectrosc*. 148, (1991) 371-377.

[16] M. A. Palafox, N. Iza, M. Gil and J .L. Núñez, *Int. J. Quantum Chem.* 89 (2002) 25–47.

Chapter 7

A high resolution study of the pure rotational and rovibrational spectra of silacyclobutane[a]

7.1 Introduction

The high resolution infrared study of azetidine presented in Chapter 6 described a unique far infrared signature arising from the coupling of –NH inversion to vibrational potential functions. In this chapter, the spectroscopic characterization of potential energy profiles of four-membered heterocycles is extended to a second puckered ring: silacyclobutane (c-C_3H_8Si, SCB). In azetidine, the –NH group and consequently the ring backbone move between axial and equatorial positions during ring puckering, has an asymmetric single well ring puckering potential profile as the axial configuration is not a minimum. In SCB, the –NH group is replaced by a –SiH_2 group. As a result, the ring backbone of SCB is described by a symmetric double well potential energy function and the two equivalent puckered configurations, which correspond to the two minima on the potential energy curve, can interconvert via tunnelling. Therefore, the molecular motions in SCB require a quantum mechanical description and high resolution spectroscopic techniques offer the opportunity to identify and analyze transitions that are sensitive to this complex potential energy profile.

Because SCB is a floppy molecule, the determination of the molecular structure at equilibrium is not straightforward but is essential to establish vibrational coordinates for

any potential functions. For this reason, structural determination of SCB was conducted via *ab initio* and density functional theory (DFT) methods[1, 2] and experimentally via gas phase electron diffraction (ED).[2] The geometry of SCB is that of a puckered ring with a puckering angle of 34.5° (MP2/cc-pVTZ)[1] or 33.5° (ED).[2] More recently, the low resolution infrared and Raman fundamental bands of SCB were revisited without rotational resolution.[1] A comprehensive assignment of all 21 normal modes was performed based on harmonic DFT frequency calculations at the B3LYP/cc-pVTZ level. SCB has been the subject of other spectroscopic investigations, most of which particularly focused on probing energy levels in the ring puckering potential manifold. The far infrared spectra of the ring puckering mode of the isotopic parent and minor isotopologues of SCB were studied and the corresponding potential function was characterized to have a double minimum potential well with a barrier to planarity of 440 cm^{-1}(shown in Figure 7.1).[3, 4] Later, Pringle observed spectra related to ring inversion in the ground and first excited ring puckering vibrational states of SCB via microwave spectroscopy.[5] This is a result of the fact that the lowest three vibrational states of the ring puckering mode fall below the barrier to planarity. Pringle's microwave investigation estimated an energy splitting of ~75 MHz between the two ring inversion tunnelling states in the ground vibrational state (0^+ and 0^-) whereas the value of this splitting increases to ~7800 MHz in the first excited ring puckering vibrational state. It is important to note, however, due to the limited resolution of microwave instruments at the time (0.2 MHz), this was not directly observed as a tunnelling splitting of the *a*-type transitions within each tunnelling state ($0^+ \rightarrow 0^+$, $0^- \rightarrow 0^-$ in Figure 7.1) as the two states (0^+ and 0^-) are so close in energy that their spectroscopic constants are very similar. The

evidence of ring inversion tunnelling was instead shown by the presence of transitions crossing between tunnelling states $(0^+ \leftrightarrow 0^-)$ which are allowed under molecular symmetry group theory.

Figure 7.1: Potential energy function along the ring puckering coordinate (θ) of silacyclobutane. The barrier to planarity is taken from Ref. [5]. The splitting of levels 0^+ and 0^- was determined in this work, and the ground state ring puckering angle was derived: 31.1(4)°. The energy level splittings are not to scale.
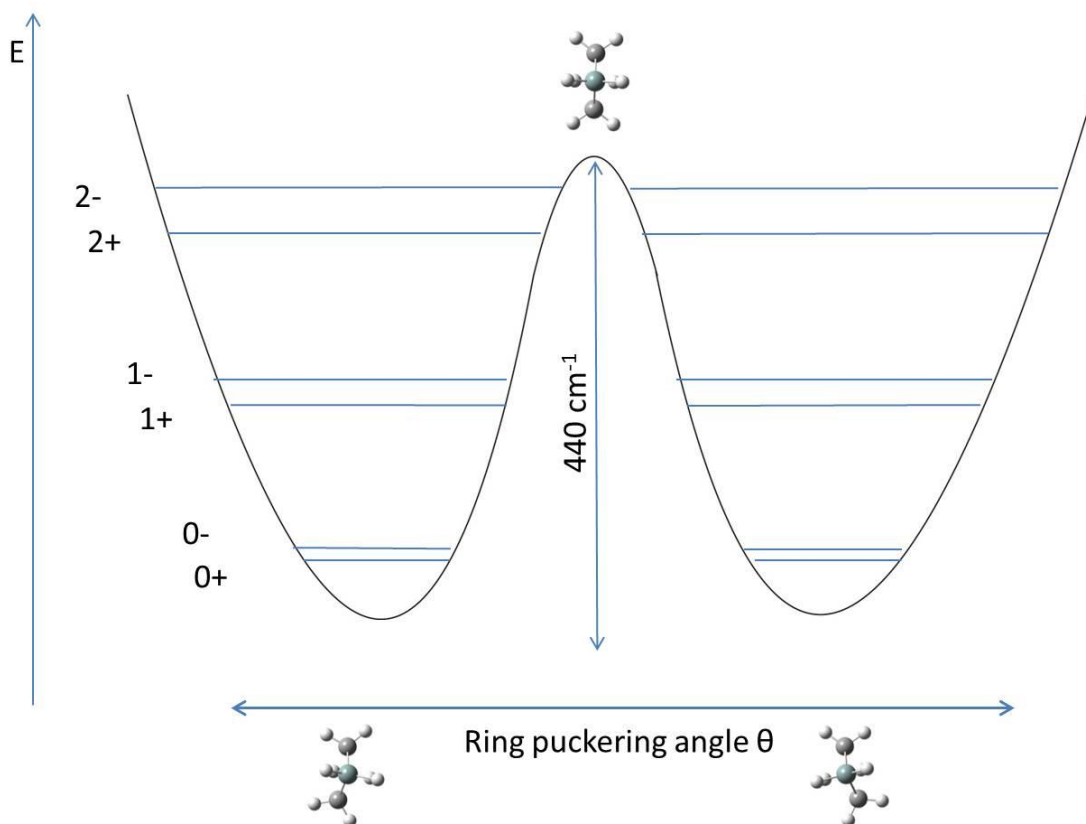
This chapter describes the first high resolution microwave and far infrared spectroscopic investigation of SCB. The high resolution Fourier transform microwave spectrometer employed in this study enabled the direct observation of the ground state ring inversion tunnelling splitting of the 0^+ and 0^- states for the first time. The observation and analysis of pure rotational transitions of the isotopic parent SCB and four mono-substituted isotopologues in natural abundance (^{29}Si-4.7%, ^{30}Si-3.1%, ^{13}C-1.1%) allowed the accurate experimental determination of the structural parameters of the SCB ring skeleton. In the far infrared region, the assignment of rotationally resolved vibrational spectra for the parent species revealed the presence of ring inversion tunnelling doubling in the first excited state of the ν_{29} SiH$_2$ rocking and the ν_{30} ring puckering vibrational modes. The successful analyses of these two lowest frequency vibrational bands not only provided a set of accurately determined spectroscopic constants for the excited states, but also made possible a comprehensive understanding of the ground state of SCB when combined with the observed pure rotational transitions. The direct observation of quantum mechanical tunnelling in both the microwave and far infrared spectra provide incredibly detailed information about the potential energy landscape of SCB. To the best of our knowledge, no other heterocyclic molecule has been probed in such detail in this spectral range.

7.2 Experimental details

As SCB is not commercially available, the sample was prepared by a one-step reduction[6] of 1,1-dichlorosilacyclobutane (GELEST, 97%). This precursor was mixed with $LiAlH_4$ in a 2:1 ratio in *n*-butyl ether for 24 h. The final product was distilled from the mixture at 110 °C using a dry ice/acetone-cooled receiving flask and verified by GC/MS.

The pure rotational spectrum of SCB was recorded using the Balle-Flygare type pulsed-jet Fourier transform microwave (FTMW) spectrometer that was described in Chapter 2. The gaseous sample for the pure rotational study was prepared as a mixture of 1% SCB in neon. The total backing pressure was maintained at ~5 atm. The spectra of all isotopologues were observed in natural abundance.

The rovibrational spectra of SCB were collected at the Canadian Light Source (CLS) using a synchrotron based Fourier transform infrared (FTIR) spectrometer as described in Chapter 3. The low pressure gas sample was prepared by introducing vapour pressure into a multipass gas cell from the synthesized liquid sample. The spectra of the ν_{29} and ν_{30} bands were recorded in two separate spectral windows as the required optical components have different operating ranges. For the ν_{29} band, the spectrometer was outfitted with a 6 μm Mylar beamsplitter and a GeCu detector. A total of 528 interferograms were recorded at a sample pressure of 448 mTorr with a resolution of 0.000959 cm^{-1}. The spectrum of the ν_{30} band was collected at a pressure of 1060 mTorr with a 75 μm Mylar beamsplitter and a helium-cooled Si bolometer detector attached to the spectrometer. As the ring puckering transitions had low intensity and lots of sample was needed to see infrared absorption, the resolution of the spectrum was pressure limited

(rather than Doppler) and thus resolution was sacrificed to record lines of sufficient intensity for analysis. The instrumental resolution was set at 0.001918 cm^{-1} to reflect the expected pressure broadening and this allowed faster data collection. Key experimental parameters are summarized in Table 7.1.

Calibration of the recorded transitions was performed using lines due to residual water vapour in the two regions: transitions from 135 to 183 cm^{-1} for the ν_{30} band and lines from 340-447 cm^{-1} for the ν_{29} band. These were compared to those found in the HITRAN database.[7] Generally, the recorded frequencies in both spectral regions were found to be accurate within 0.0003 cm^{-1}.

Table 7.1: Experimental parameters of recorded bands of silacyclobutane.

	ν_{29}	ν_{30}
Band origin (cm^{-1})	158	410
Pressure (mTorr)	448	1060
No. of interferograms collected	528	844
Time spent to record interferograms (h)	53	42
Resolution (cm^{-1})	0.000959	0.001918[a]
Lines used in calibration	H$_2$O 340-450 cm^{-1}	H$_2$O 130-190 cm^{-1}

7.3 Spectral assignment and analysis

Initially, the observed pure rotational spectra as well as the rovibrational transitions in the ν_{29} and ν_{30} bands of silacyclobutane were assigned and fit separately

[a] Resolution was reduced for the ν_{30} band as at 1060 mTorr the line width is pressure broadened.

using Watson's A-reduced Hamiltonian in I^r representation in Pickett's SPFIT program.[8] Eventually, rovibrational transitions from both bands were merged simultaneously in a global analysis to obtain the final set of spectroscopic constants. The assignment and analysis of the pure rotational and rovibrational spectra and the observed inversion tunnelling splittings are detailed below.

7.3.1 Pure rotational spectrum

Although the ground state structure of SCB (shown in Figure 7.2) belongs to the C_s point group, the molecular symmetry group of C_{2v} is used to account for the ring inversion tunnelling between the two equivalent minima of its symmetric double well potential. This potential function has a barrier to planarity of 440 cm^{-1} and consequently the ground state vibrational state is split into two components (labelled as 0^+ and 0^- in Figure 7.1) where the superscript describes the symmetry of the inversion part of the wavefunction (B_1). This means that the two ring inversion tunnelling components have inversion symmetries that are A_1 (symmetric, +) and B_1 (antisymmetric, -). As for azetidine, the rotational part of the wavefunction (Γ_{rot}) has the following symmetries: $A_1(ee)$, $A_2(eo)$, $B_1(oo)$ and $B_2(oe)$ for various combinations of (K_aK_c). For a transition to occur, the symmetry product of the wavefuction ($\Gamma_{rot} \times \Gamma_{inv}$) for each state must contain the totally symmetric (A_1) representation when combined with the symmetry of the space-fixed molecular dipole moment (A_2). As a result, the allowed microwave transitions follow a-type selection rules ($eo \leftrightarrow ee$ and $oe \leftrightarrow oo$) within each tunnelling state and c-type selection rules ($ee \leftrightarrow oe$ and $oo \leftrightarrow eo$) that cross between inversion states as shown in Figure 7.3.

Figure 7.2: Structure of silacyclobutane in its principal axis system.
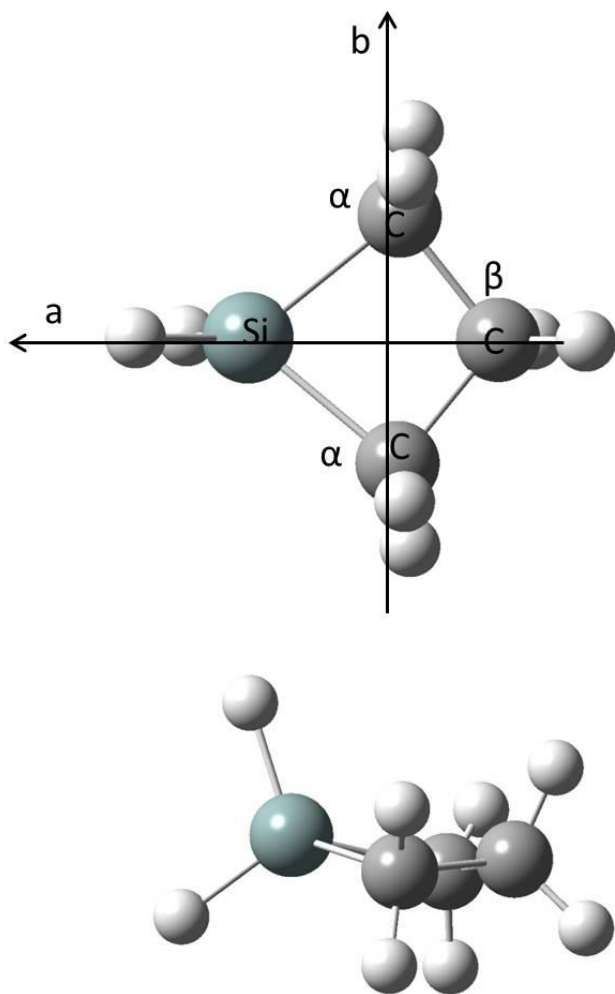
Figure 7.3: A schematic of transitions observed in the spectra of the ground state of silacyclobutane. Rotational levels of both the 0^+ and 0^- state are labelled to reflect the rotation-inversion symmetry. Solid and dashed lines indicate examples of allowed a-type and c-type transitions, respectively. e (o) indicates even (odd) of K_a or K_c values.
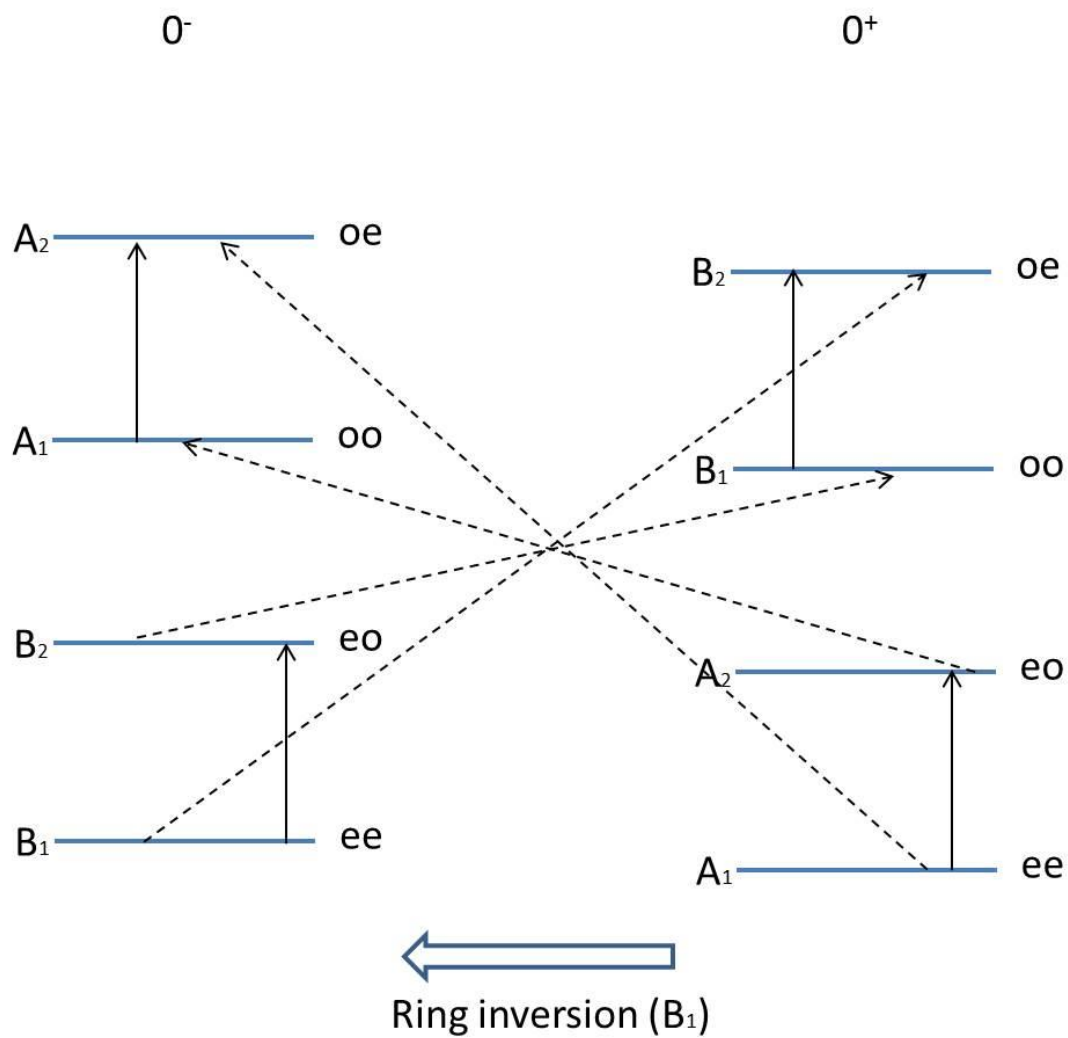
7.3.1.1 Normal isotopologue

The search for pure rotational transitions of the parent isotopic species was assisted by using the previously reported rotational constants from Pringle's low resolution microwave study.[5] A total of 26 transitions were observed between 6 and 24 GHz including eight pairs of tunnelling doubled a-type transitions and 10 weak c-type transitions that cross ring inversion states (0^+ to 0^-, 0^- to 0^+). Figure 7.4 shows the observed 10 kHz splitting of the 1_{01}-0_{00} (J $K_a K_c$) a-type transitions of states 0^+ and 0^-. All observed transitions were assigned to the correct tunnelling state 0^+ and 0^- unambiguously by completing two closed loops of transitions as depicted in the energy level diagram shown in Figure 7.5. The assigned transitions of normal SCB are listed in Table 7.2. The observation of c-type transitions allowed the determination of the energy difference between the two tunnelling states 0^+ and 0^- ($\Delta E_{v=0}$). The ground state constants including the rotational and centrifugal distortion constants for each state plus the $\Delta E_{v=0}$ energy gap were are summarized in Table 7.3.

7.3.1.2 Minor isotopologues

In order to determine geometrical parameters via microwave spectroscopy, the pure rotational transitions of additional isotopologues were sought. Spectra due to the presence of less abundant isotopic species of SCB were observed for the ^{29}Si (4.7%), ^{30}Si (3.1%), α-^{13}C (2.2%) and β-^{13}C (1.1%) mono-substituted versions. Considering the lower abundances compared to that of the parent species, transitions due to these minor isotopologues were much more difficult to observe. As a result, fewer transitions were recorded. For the ^{29}Si species, 10 transitions were identified including two c-type

Figure 7.4: FTMW spectrum of the Doppler-doubled 1_{01}-0_{00} ($J'_{K'_a K'_c} \rightarrow J''_{K''_a K''_c}$) transition of the parent isotopologue of silacyclobutane after 200 averaging cycles. The additional 10 kHz splitting of this transition is due to ring inversion tunnelling. The lower frequency transition corresponds to the symmetric inversion tunnelling component (state 0^+), and the higher corresponds to the antisymmetric component (state 0^-).
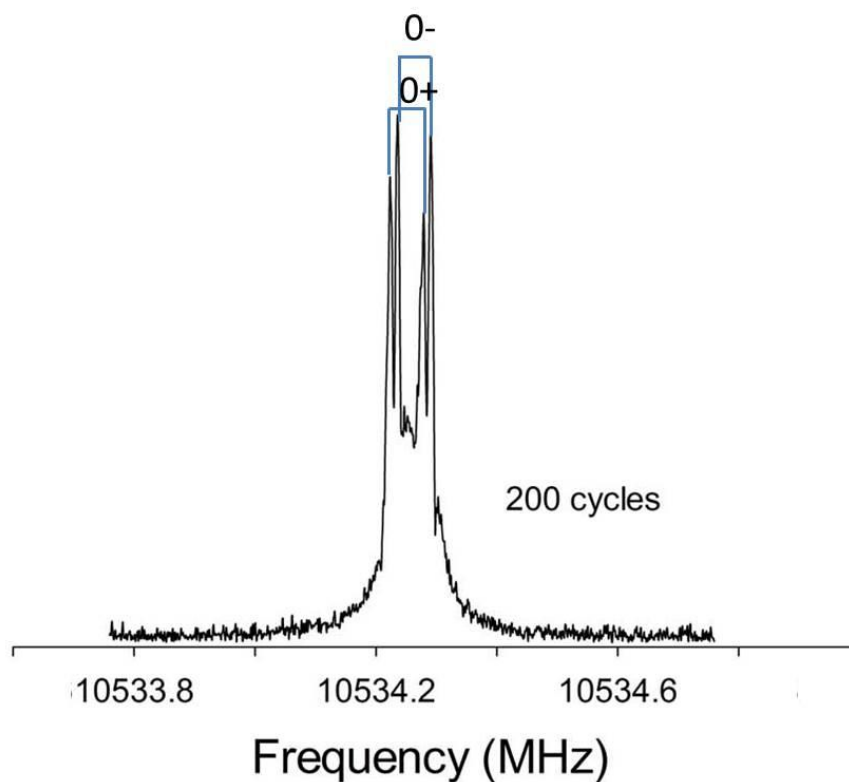
Figure 7.5: Energy level diagram of some of the observed microwave transitions of normal silacyclobutane. The observed *a*-type (vertical lines) and *c*-type (diagonal lines) transitions form closed loops, which were used to unambiguously assign transitions to the ring inversion tunnelling states 0^+ and 0^-.
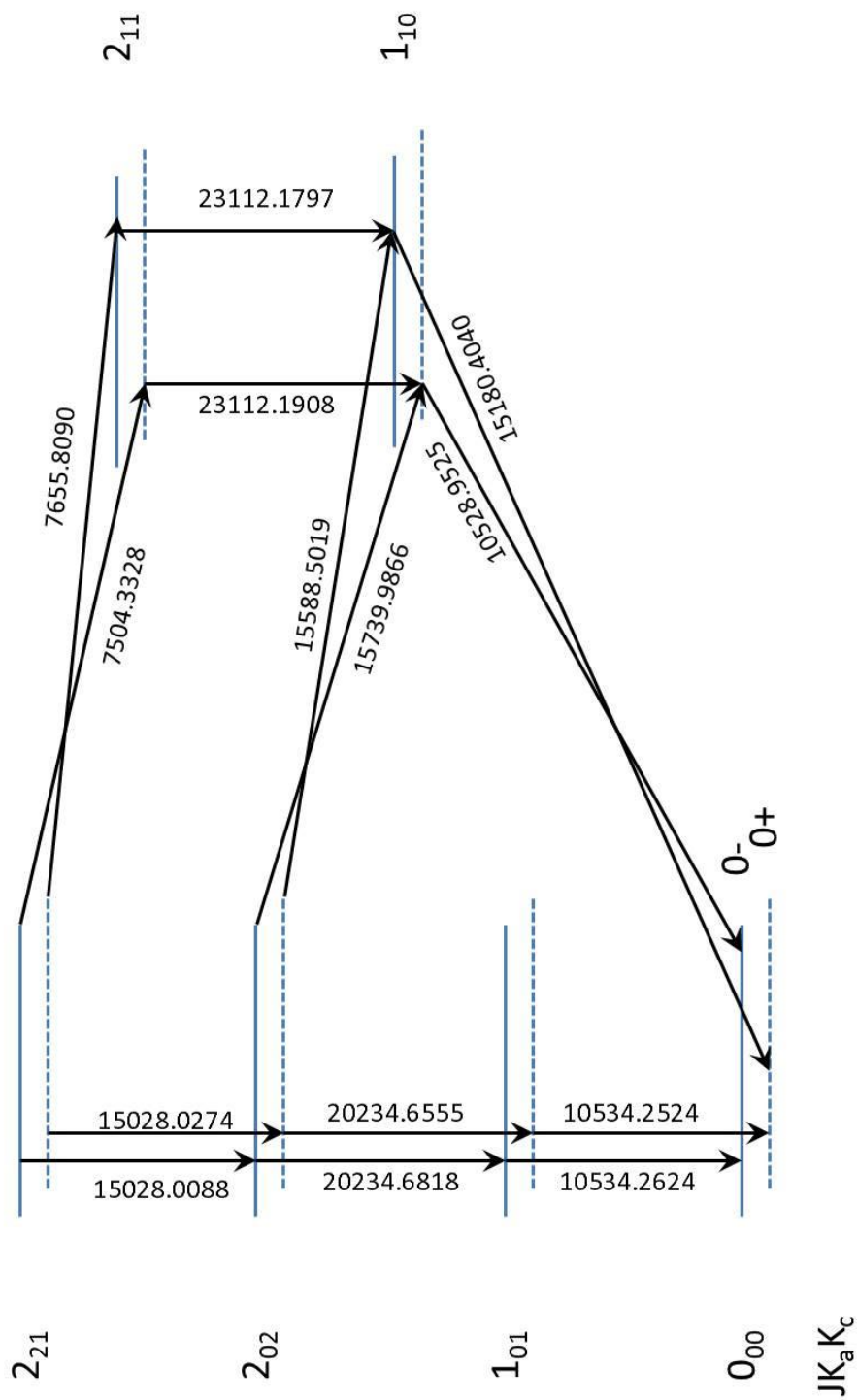
Table 7.2: Observed pure rotational transitions of silacyclobutane in MHz.

a-type $J'_{K'_a K'_c} \rightarrow J''_{K''_a K''_c}$	0^+ ν_{obs}	$\nu_{obs} - \nu_{cal}$	0^- ν_{obs}	$\nu_{obs} - \nu_{cal}$	c-type $J'_{K'_a K'_c v'} \rightarrow J''_{K''_a K''_c v''}$	ν_{obs}	$\nu_{obs} - \nu_{cal}$
$1_{01} \rightarrow 0_{00}$	10534.2524	-0.0020	10534.2624	0.0000	$1_{10(0+)} \rightarrow 0_{00(0-)}$	15028.9525	-0.0008
$2_{02} \rightarrow 1_{01}$	20234.6555	0.0067	20234.6818	-0.0003	$1_{10(0-)} \rightarrow 0_{00(0+)}$	15180.4040	0.0028
$2_{12} \rightarrow 1_{11}$	19024.7465	-0.0042	19024.7771	0.0037	$2_{02(0+)} \rightarrow 1_{10(0-)}$	15588.5019	0.0000
$2_{11} \rightarrow 1_{10}$	23112.1797	-0.0016	23112.1908	0.0002	$2_{02(0-)} \rightarrow 1_{10(0+)}$	15739.9866	-0.0046
$2_{11} \rightarrow 2_{12}$	6131.1597	-0.0013	6131.1314	0.0057	$2_{21(0+)} \rightarrow 2_{11(0-)}$	7504.3328	-0.0047
$2_{21} \rightarrow 2_{02}$	15028.0274	0.0013	15028.0088	0.0047	$2_{21(0-)} \rightarrow 2_{11(0+)}$	7655.8097	-0.0043
$3_{12} \rightarrow 3_{13}$	12027.3755	-0.0007	12027.4009	-0.0031	$2_{20(0+)} \rightarrow 2_{12(0-)}$	14469.2710	-0.0017
$3_{22} \rightarrow 3_{03}$	17728.2627	0.0022	17728.2321	-0.0025	$2_{20(0-)} \rightarrow 2_{12(0+)}$	14620.7660	-0.0013
					$3_{31(0+)} \rightarrow 3_{21(0-)}$	14580.8274	0.0006
					$3_{31(0-)} \rightarrow 3_{21(0+)}$	14732.3218	0.0008

Table 7.3: Ground state spectroscopic constants for both tunnelling inversion states (0^+ and 0^-) of normal silacyclobutane determined by FTMW spectroscopy.

	0^+	0^-
Rotational constants / MHz		
A	8815.6917(12)	8815.6945(12)
B	6288.9936(15)	6288.9897(11)
C	4245.2692(17)	4245.2811(11)
Centrifugal distortion constants / 10^{-3} MHz[a]		
Δ_J	2.10(14)	2.10
Δ_{JK}	4.41(16)	4.41
Δ_K	-1.91(16)	-1.91
δ_J	0.313(19)	0.313
δ_K	-1.36(21)	-1.36
$\Delta E_{v=0}$ /MHz		75.7260(19)
rms error /kHz		3.0
No. of transitions		26

transitions and four tunnelling split *a*-type transitions while one *c*-type transition and four tunnelling split *a*-type transitions were obtained for the ^{30}Si species. Assigned transitions are listed in Table 7.4. Only the rotational constants were allowed to vary in the fitting of the two silicon isotopic species with the distortion constants held fixed to the values of the ground state as fewer transitions were recorded. Spectroscopic constants determined for these two silicon species are summarized in Table 7.5.

The transitions due to the two ^{13}C species had considerably lower intensity than those of the silicon isotopologues. As a consequence, only *a*-type tunnelling split transitions (four for α-^{13}C and three for β-^{13}C) were observed. The absence of *c*-type transitions made it impossible to determine the $\Delta E_{v=0}$ term for these two carbon isotopologues. Thus, the energy gap determined from the ^{29}Si species was used in the fitting of these spectra as the isotopologues have nearly the same mass and the distortion constants were again held fixed to the values from the parent species. The spectra observed for the β-^{13}C species included only three transitions (as shown in Table 7.6) and thus the reported root-mean-square (rms) error of the fit is zero. The rotational and centrifugal distortion constants determined for the ^{13}C isotopologues are summarized in Table 7.5.

7.3.2 Rovibrational spectra of the ν_{29} and ν_{30} bands

7.3.2.1 Infrared spectra of the ν_{29} band

The ν_{29} band centered at ~410 cm^{-1}, attributed to SiH$_2$ rocking in the previous low resolution infrared study,[1] has B$_1$ symmetry and corresponds to *c*-type rovibrational selection rules *oe↔ee* and *eo↔oo*. However, the overview of this band reveals a typical

Table 7.4: Observed pure rotational transitions of the ^{29}Si and ^{30}Si isotopologues of silacyclobutane in MHz.

a-type

$J'_{K'_a K'_c} \rightarrow J''_{K''_a K''_c}$	^{29}Si 0^+ ν_{obs}	$\nu_{obs}-\nu_{cal}$	^{29}Si 0^- ν_{obs}	$\nu_{obs}-\nu_{cal}$	^{30}Si 0^+ ν_{obs}	$\nu_{obs}-\nu_{cal}$	^{30}Si 0^- ν_{obs}	$\nu_{obs}-\nu_{cal}$
$1_{01}\rightarrow0_{00}$	10149.4088	-0.005	10419.4225	-0.0024	10310.3711	-0.0043	10310.3843	-0.0015
$2_{02}\rightarrow1_{01}$	20049.2484	0.0029	20049.2758	0.0029	19871.2627	0.0000	19871.3889	0.0000
$2_{12}\rightarrow1_{11}$	18837.9585	-0.0013	18837.9899	-0.0019	18660.2092	0.0011	18660.2510	0.0004
$2_{11}\rightarrow1_{10}$	22839.6112	0.0012	22839.6225	0.0005	22581.1958	0.0011	22581.2058	0.0000

c-type

$J'_{K'_a K'_c v'} \rightarrow J''_{K''_a K''_c v''}$	^{29}Si ν_{obs}	$\nu_{obs}-\nu_{cal}$	^{30}Si ν_{obs}	$\nu_{obs}-\nu_{cal}$
$1_{10(0+)}\rightarrow0_{00(0-)}$	14950.1750	-0.0006		
$1_{10(0-)}\rightarrow0_{00(0+)}$	15100.4981	-0.0006	15024.8449	0.0000

Table 7.5: Ground state spectroscopic constants for both tunnelling inversion states (0[+] and 0[-]) of minor isotopologues of silacyclobutane determined by FTMW spectroscopy in MHz.[a]

	^{29}Si		^{30}Si		α-^{13}C		β-^{13}C	
	0[+]	0[-]	0[+]	0[-]	0[+]	0[-]	0[+ b]	0[- b]
A	8815.251(11)	8815.186(11)	8814.294(11)	8814.771(11)	8599.3515(25)	8599.2956(25)	8810.3526(25)	8810.3256(25)
B	6210.1282(9)	6210.124(9)	6135.4392(6)	6135.4358(6)	6272.92537(18)	6272.92542(17)	6148.10728(18)	6148.10903(18)
C	4209.2940(8)	4209.3091(8)	4174.94476(6)	4174.9585(6)	4189.15183(18)	4189.16427(17)	4182.15429(18)	4182.16678(18)
$\Delta E_{v=0}$	75.198(11)		74.647(11)		75.198[c]		75.198	
Rms error /kHz	2.4		1.6		0.5		0.5	
No. of transitions	10		9		8		6	

[a] The centrifugal distortion constants for the isotopologues shown here were held fixed to those of the normal species in Table 7.3.
[b] The uncertainties reported here are those obtained for the equivalent parameter in the α-^{13}C species as the fit of the β-^{13}C isotopologue has only six transitions and six constants.
[c] The $\Delta E_{v=0}$ values were held fixed to the value reported for the ^{29}Si species.

Table 7.6: Observed pure rotational transitions of the ^{13}C isotopologues of silacyclobutane in MHz.

$J'_{K'_a K'_c} \rightarrow J''_{K''_a K''_c}$	α-^{13}C				β-^{13}C			
	0^+		0^-		0^+		0^-	
a-type	ν_{obs}	ν_{obs}-ν_{cal}	ν_{obs}	ν_{obs}-ν_{cal}	ν_{obs}	ν_{obs}-ν_{cal} [a]	ν_{obs}	ν_{obs}-ν_{cal} [a]
$1_{01} \rightarrow 0_{00}$	10462.0680	-0.007	10462.0822	0.0010	10330.2530	0.0000	10330.2628	0.0000
$2_{02} \rightarrow 1_{01}$	20018.1617	0.000	20018.1881	0.0000	19904.4344	0.0000	19904.4626	0.0000
$2_{12} \rightarrow 1_{11}$	18840.3275	0.0002	18840.3574	-0.0003	18694.5167	0.0000	18694.5488	0.0000
$2_{11} \rightarrow 1_{10}$	23007.8605	0.0002	23301.8797	-0.0003				

[a] Only three transitions were observed and fit to three rotational constants

a-type band contour as shown in Figure 7.6. With the knowledge of the tunnelling splitting observed in the ground vibrational state from the microwave work in the present study, a dense rovibrational spectrum due to ring inversion doubling was anticipated in the far infrared region. Furthermore, consideration of the ring inversion symmetry (B_1) allows for transitions that cross inversion states ($0^+ \rightarrow \nu_{29}^-$ and $0^- \rightarrow \nu_{29}^+$) as seen in the microwave study.

No obvious patterns were observed in the initial visual inspection of the rotational structure of this band. To identify regularly spaced progressions, the most intense transitions between 390 and 430 cm^{-1} were represented in the format of a Loomis-Wood plot in the Igor Pro software package.[9,10] As shown in Figure 7.7, peaks in the P branch of this band are grouped in such a way that those sharing common K_a quantum numbers but having different J values are arranged in a vertical series of K_a on the Loomis-Wood plot. Two parallel sets of strong progressions were recognized in this plot, suggesting that the excited vibrational state of the ν_{29} band is split into two components (which are ~0.17 cm^{-1} apart). The observed spectral pattern was then compared with the simulated spectrum based on the estimated band origins and the ground state constants determined from the microwave analysis, leading to the tentative assignment of a few of the strongest infrared transitions. Information about the ground state energy levels obtained from the microwave experiment confirmed that these transitions obey *a*-type selection rules *eo↔ee* and *oe↔oo*. The simulated spectrum was then refined by fitting the newly assigned lines and the assignment process continued in an iterative manner until the strong progressions were included.

Figure 7.6: An overview spectrum showing the band structure of the v_{29} band of silacyclobutane at $\sim$410 cm^{-1}.

Figure 7.7: A portion of the Loomis-Wood plot of the ν_{29} band of silacyclobutane between ~395 and ~402 cm^{-1} showing a-type progressions used to aid in its assignment. Red (polygon) and blue (star) labels indicate transitions sharing common K$_a$ but having different J values with $0^+ \rightarrow \nu_{29}^-$ and $0^- \rightarrow \nu_{29}^+$, respectively.

171
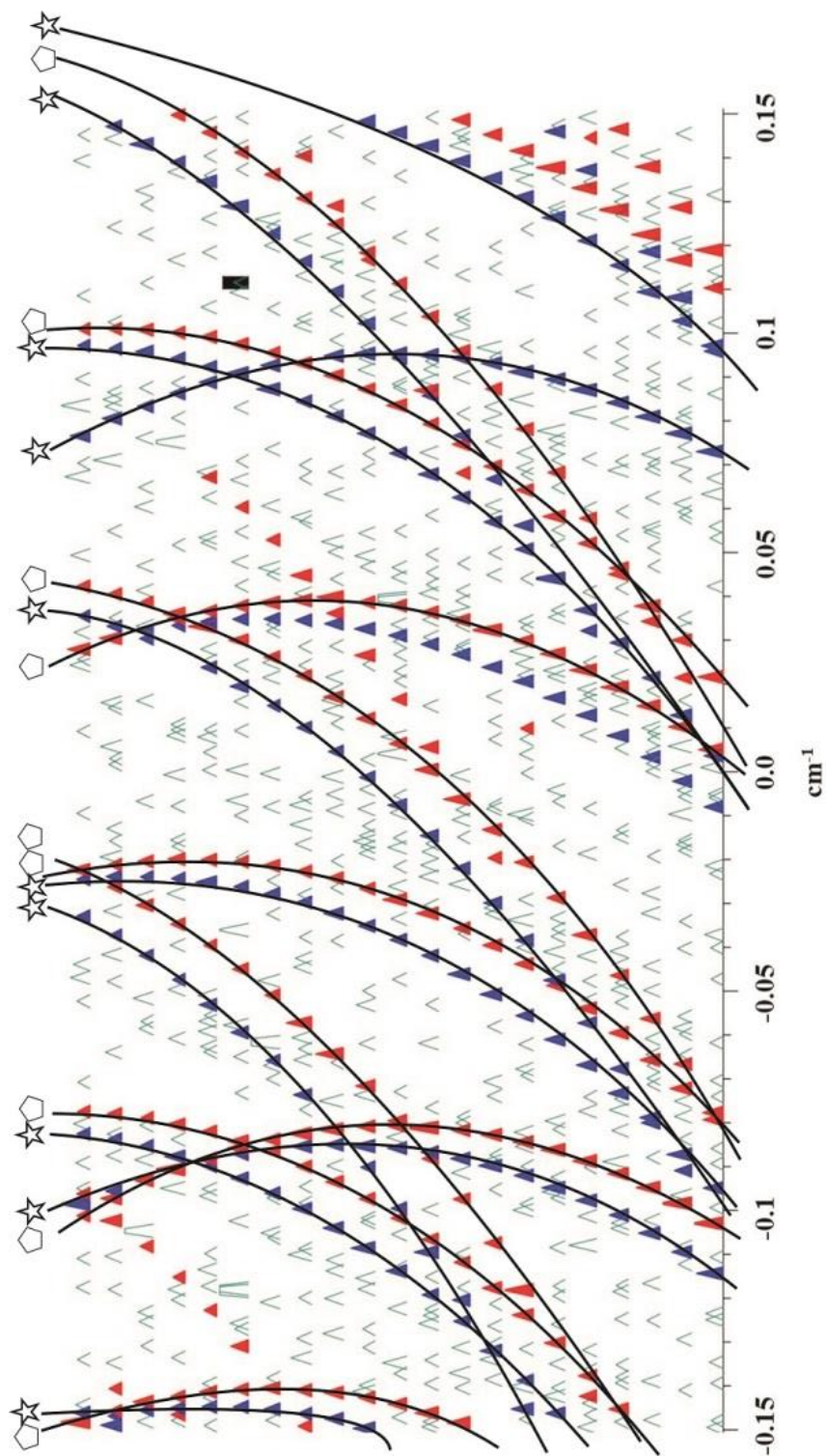
Overall, 3085 a-type transitions from the P and R branches were assigned for the tunneling doubled ν_{29} band. The Q branch assignment was attempted but abandoned in the end as the spectrum was so dense that the transitions were not resolved. After the assignment of the a-type lines, a few unassigned features remained in the spectrum as seen in Figure 7.7. A second Loomis-Wood plot (Figure 7.8) shows that these transitions actually form a series of tunnelling doubled progressions too! Note that the spacing (x-axis) of the pattern on this plot was adjusted so that it was about twice that in Figure 7.7 (which shows the a-type pattern). The new series identified in Figure 7.8 were later confirmed to be c-type progressions with each progression corresponding to transitions having common K_c but different J values. These progressions are due to c-type transitions connecting vibrational levels of the same inversion symmetry ($0^+ \rightarrow \nu_{29}^+$ and $0^- \rightarrow \nu_{29}^-$). The assignment procedure was similar to that previously described for the two parallel sets of a-type transitions and an additional 3392 transitions were added to the fit. In the end, 6477 a-/c-type transitions from the ν_{29} band were assigned and fit using the Hamiltonian model described previously. The number of transitions and the quantum number coverage corresponding to each vibrational level pair are listed in Table 7.7.

7.3.2.2 Infrared spectra of the ν_{30} band

The ν_{30} band at ~158 cm^{-1} was attributed to the ring puckering motion of silacyclobutane in Ref. [1]. As in the case of the ν_{29} band, this vibration has B$_1$ symmetry and gives rise to c-type selection rules $oe\leftrightarrow ee$ and $eo\leftrightarrow oo$. Initial inspection of the band contour shows a typical c-type envelope in which the Q branch has much higher intensity compared to the P and R branches as shown in Figure 7.9. A closer look reveals that

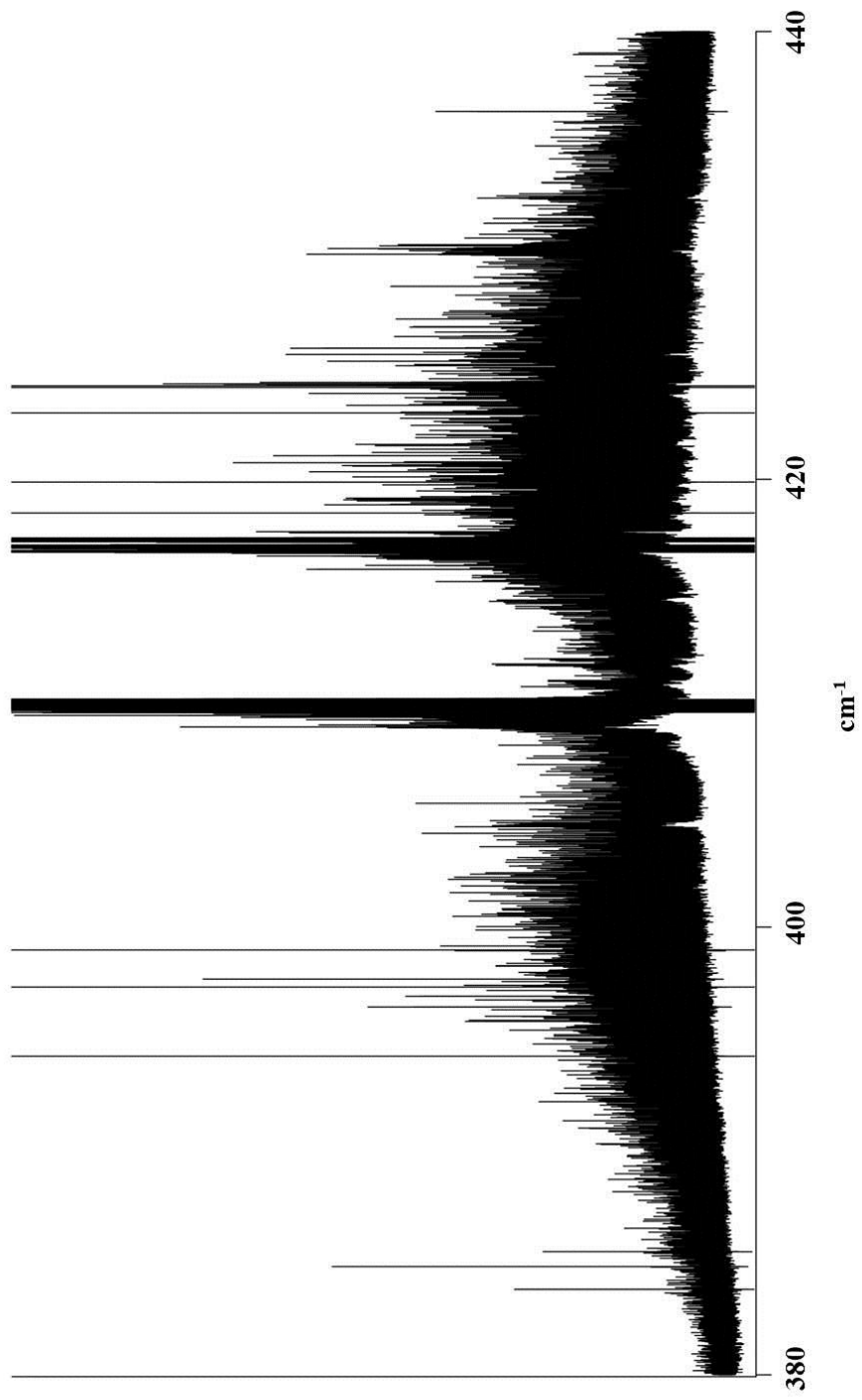Figure 7.8: A portion of the Loomis-Wood plot of the v_{29} band of silacyclobutane between ~388 and ~402 cm^{-1} showing c-type progressions used to aid in its assignment. Black (polygon) and green (star) labels indicate transitions sharing common K_c but having different J values with $0^+ \rightarrow v_{29}^+$ and $0^- \rightarrow v_{29}^-$, respectively.
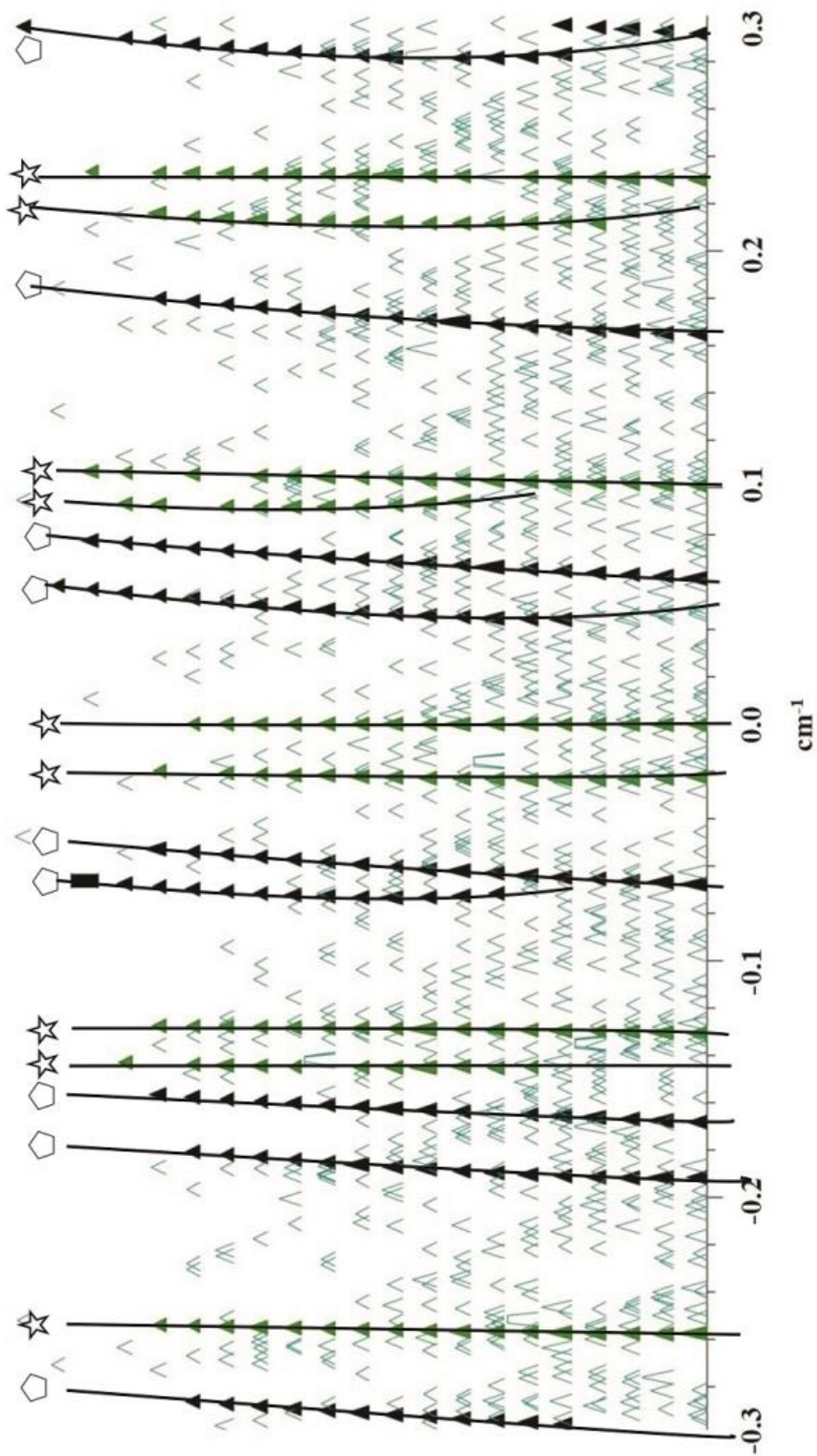
Table 7.7: Rotational energy levels covered in the rovibrational spectral analysis of the ground state, v_{29} and v_{30} states of silacyclobutane.

type	0^a	$0^+ \to v_{30}^{+b}$	$0^- \to v_{30}^-$	$0^+ \to v_{29}^+$	$0^- \to v_{29}^-$	$0^+ \to v_{29}^-$	$0^- \to v_{29}^+$
	GSCD	c-type IR	c-type IR	c-type IR	c-type IR	a-type IR	a-type IR
J(min)	5	8	5	4	4	5	4
J(max)	52	35	40	40	40	50	52
K_a(min)	0	6	0	0	0	0	0
K_a(max)	40	35	40	40	40	25	19
K_c(min)	0	0	0	0	0	0	0
K_c(max)	52	13	30	39	37	50	52
No. of transitions	1108	584	1215	1685	1707	1513	1572

[a] From ground state combination differences.
[b] The vibrational labels refer to the energy states defined in Figure 7.12.

Figure 7.9: An overview spectrum showing the *c*-type band structure of the ν_{30} band of silacyclobutane at $\sim$158 cm^{-1}
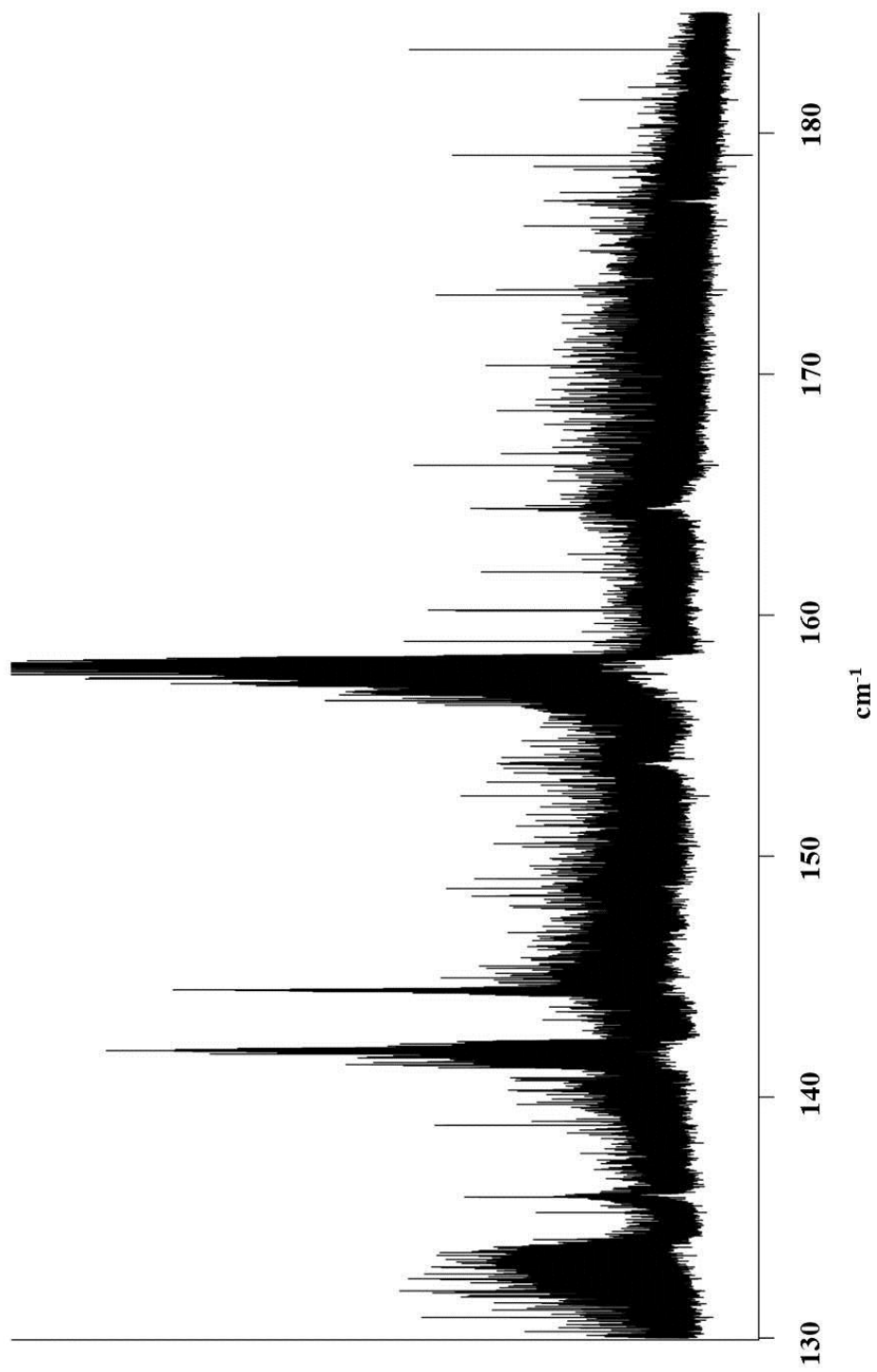
transitions in the P and R branches are of such low intensity that even the strongest ones are barely above the noise level. This, together with possible spectral congestion as a result of inversion tunnelling doubling, made the preliminary assignment of the ν_{30} band very difficult. A Loomis-Wood plot was constructed to aid in the initial stages of the assignment of the ring puckering mode. Shown in Figure 7.10 is a section of the R branch progressions on this plot. Two sets of regularly occurring progressions in the P and R branches were identified as transitions within symmetric ($0^+ \rightarrow \nu_{30}^+$) and antisymmetric ($0^- \rightarrow \nu_{30}^-$) inversion states of the molecule. The assignment scheme described above was implemented to assign rovibrational transitions in the ν_{30} band. Overall, 1799 c-type transitions were assigned between ~135 and ~181 cm^{-1}. The coverage of rotational levels is shown in Table 7.7. Given that a-type transitions were observed in the c-type ν_{29} band with the same symmetry, considerable effort was spent to look for similar transitions in this region. Unfortunately, such a-type progressions were not found here. As most of the triangles (peaks) shown on the Loomis-Wood plot were assigned to the c-type transitions, the absence of visible a-type ones is believed to be as a result of their low intensities.

7.3.2.3 Global analysis

The ground state spectroscopic constants were determined by fitting 1108 ground state combination differences (GSCDs) calculated from the assigned rovibrational transitions in the ν_{29} and ν_{30} bands. As the resultant spectroscopic parameters of the two tunnelling components of the ground state (0^+ and 0^-) are the same within experimental uncertainties, the values of state 0^+ were subsequently held fixed to those of state 0^- in the fitting routine. All 8276 assigned rovibrational transitions from both bands were

Figure 7.10: A portion of the Loomis-Wood plot of the v_{30} band of silacyclobutane between ~165 and ~176 cm^{-1} showing c-type progressions used to aid in its assignment. Red (star) and blue (polygon) labels indicate transitions sharing common K_c but having different J values $0^+ \rightarrow v_{29}^+$ and $0^- \rightarrow v_{29}^-$, respectively.

177
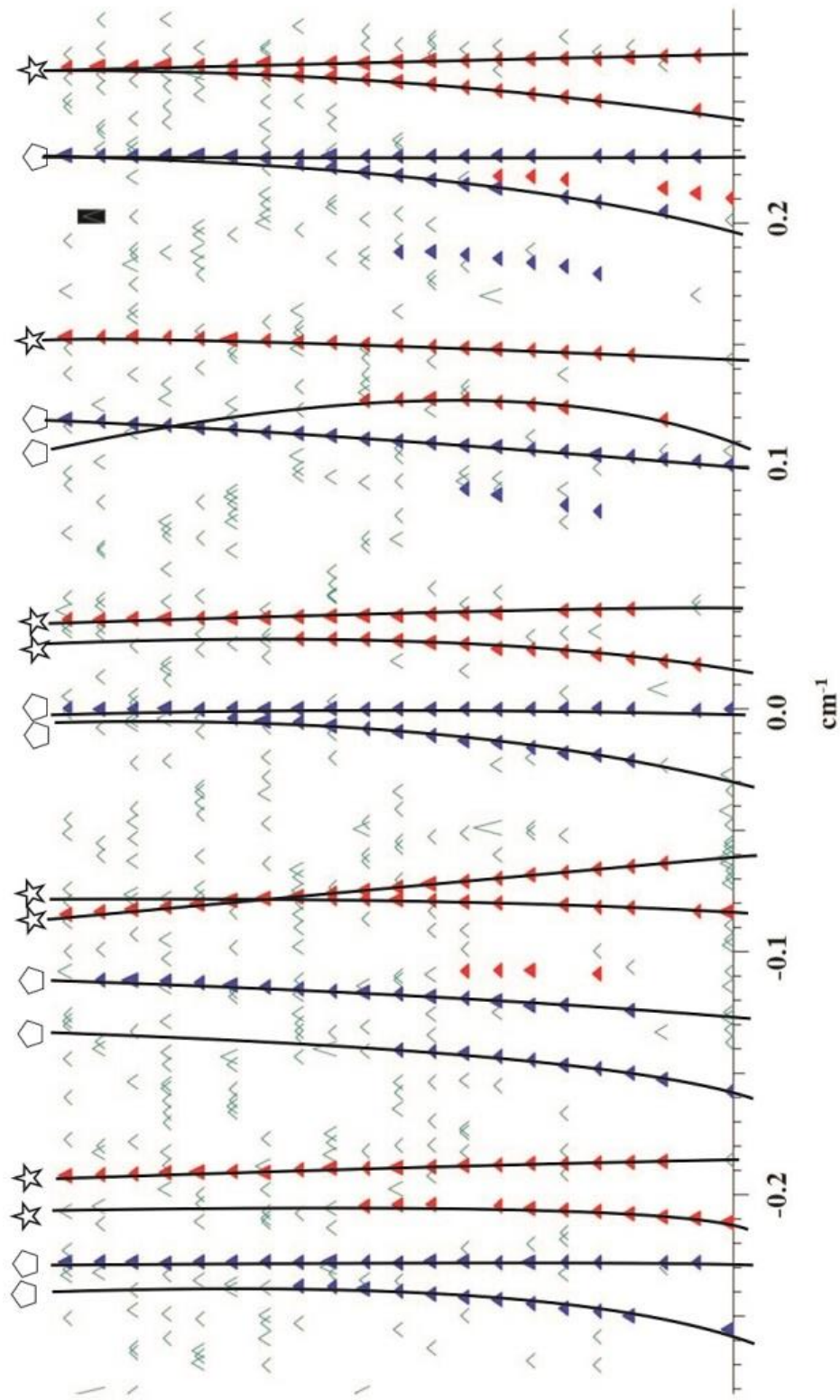
incorporated into a global fit using Watson's A-reduced Hamiltonian, I^r-representation[8] with the ground state spectroscopic constants held fixed to the values determined separately as described above. The rms error of the simultaneous two band fit was 0.000122 cm^{-1} and the resulting spectroscopic constants are listed in Table 7.8.

7.4 Discussion

7.4.1 Structural determination

The observation of pure rotational transitions due to different isotopologues of SCB enabled accurate structural determination. The corresponding selection rules of these transitions (*a*- and *c*- types) are consistent with the puckered ring skeleton as shown in Figure 7.2 as well as with previous *ab initio* and DFT calculations. An approximately 2:1 ratio was observed for the intensities of the analogous transition of the ^{29}Si and α-^{13}C isotopic species, while the natural abundances of ^{29}Si and ^{13}C are 4.7% and 1.1 %, respectively. This is explained by the fact that there are two identical α-^{13}C atoms in SCB so that the effective natural abundance of the α-^{13}C species doubles to 2.2%. The geometric parameters for the ground vibrational state of SCB were derived from the rotational constants of the five isotopologues determined in the current microwave investigation. The rotational constants used for this analysis were from the tunnelling state 0^+ as the constants for both states are so close that they match to within their experimental uncertainties. The structural analysis of SCB is detailed below.

Table 7.8: Spectroscopic constants for the ground state, v_{29} and v_{30} states of silacyclobutane determined from rovibrational analysis.

	Ground state (0^+)	$0^+ \rightarrow v_{30}^{+\ a}$	$0^- \rightarrow v_{30}^-$	$0^+ \rightarrow v_{29}^+$	$0^- \rightarrow v_{29}^-$
ν / cm^{-1}	0	158.1218438(2)	158.38466115(11)	410.03760177(14)	410.20889633(7)
$\Delta E_{v=0}$ / cm^{-1}	0.00254798(7)				
Rotational constants / cm^{-1}					
A	0.2940595(3)	0.2936414313(3)	0.2936465399(2)	0.2939495253(17)	0.2939336426(17)
B	0.2097752(6)	0.2094912516(9)	0.2094603457(4)	0.2099014834(3)	0.2099011834(3)
C	0.1416076(3)	0.140835875(2)	0.1409269238(8)	0.14136842117(14)	0.14136710565(16)
Centrifugal distortion constants / 10^{-9} cm^{-1}					
Δ_J	79.8(4)	76.5027(2)	81.49875 (11)	79.35141(5)	78.74530(6)
Δ_K	208.2(14)	209.2172(4)	216.4456(2)	207.03352(2)	206.6773(2)
Δ_{JK}	-117.0(17)	-116.3024(3)	-128.96475(17)	-115.37413(14)	-115.24683(14)
δ_j	20.55(19)	28.09670(9)	20.0635 (3)	20.89570(4)	21.02654(5)
δ_k	50.4(8)	50.435(2)	68.0900(12)	50.5996(6)	50.4352(6)
rms error / cm^{-1}	0.000198		0.000122		

[a] The vibrational labels refer to the energy states defined in Figure 7.12.

179

7.4.1.1 r_s geometry

The r_s (or substitution) structure of a molecule can be determined by the r_s-method provided that the principal inertial moments of the parent species and singly-substituted isotopologues are known. The application of the Kraitchman[11,12] equations yields a set of three coordinates (a, b, c) for each substituted atom that define the absolute value of the distance of the atom to the various axes (*a*, *b*, *c*) of the principal axis system of the parent molecule. If the b Kraitchmann coordinate is zero, it means that the substitution site is in the *ac*-plane (Figure 7.1). The uncertainties of these coordinates are calculated by Costain's rule[13] and are inversely proportional to the distance between the substituted atom and the principal axis. As a result, this error is large when the substitution site is close to a principal axis. The correct sign of the Kraitchman coordinates can only be inferred by inspection of the probable molecular structure and other considerations. In this case, the rotational constants obtained from the pure rotational spectra of four mono-isotopologues including ^{29}Si , ^{30}Si , α-^{13}C and β-^{13}C led to the determination of a set of Kratichman coordinates for each of the atoms in the ring skeleton of SCB.

The r_s coordinates determined for SCB are summarized in Table 7.9 and the principal axis system of SCB is shown in Figure 7.1. The nonzero c-coordinates (particularly for the carbon atoms) are clear evidence for a nonplanar SCB ring as the *c*-axis is perpendicular to the ring backbone. A small imaginary number for the b-coordinate of the β-C atom was calculated by the Kraitchman equations, which often indicates that the atom is very near the *b*-axis and this coordinate was set to zero in the subsequent structural analysis. For the Si atom, small real numbers were observed for the b-coordinate but the Costain uncertainties were larger than the coordinates themselves.

The examination of the A rotational constants among the three Si isotopologues, which differ by less than 1 MHz, suggests that the Si atom in fact lies very close to the *a*-axis and the b-coordinates were also set to zero for the subsequent analysis. As the results of a Kraitchman analysis are all absolute values, appropriate signs were added on the basis of the *ab initio* geometry as listed in Table 7.9. For instance, the α-C lies on the opposite side of the *ab*-plane relative to the β-C and Si atoms. Using the substitution coordinates, bond lengths and angles on the SCB ring skeleton were calculated using trigonometric relationships. These are summarized in Table 7.10.

7.4.1.2 r_0 geometry

The r_0 geometry corresponds to the zero point energy structure. As the moments of inertia of a molecule depend on the positions of the atoms, the (partial) molecular structure can be solved by fitting selected internal coordinates (key bond lengths and angles that define a structure) to the sets of rotational constants of the various isotopologues using a non-linear least squares method. The r_0 geometry of the SCB ring was obtained by fitting five structural parameters that describe the ring skeleton geometry to the 15 experimentally determined rotational constants using Kisiel's STRFIT program.[12] The internal coordinate parameters of the hydrogen atoms were fixed at the *ab initio* values reported in Ref. [1]. The five directly fit parameters in the analysis are in bold in Table 7.10 and include two bond length values of Si-$^{\alpha}$C (1.8848 (8) Å) and $^{\alpha}$C-$^{\beta}$C (1.5646 (21) Å), two bond angles values of $^{\alpha}$C-Si -$^{\alpha}$C (79.10 (4) °) and Si- $^{\alpha}$C- $^{\beta}$C (86.28 (6) °), and the dihedral angle of $^{\beta}$C- $^{\alpha}$C-Si- $^{\alpha}$C (-19.891 (23) °). The maximum discrepancy

Table 7.9: Substitution coordinates (Å) from the Kraitchman analysis for silacyclobutane.[a]

	^{29}Si	^{30}Si	α-^{13}C	β-^{13}C
a	1.0160(15)	1.0154(15)	-0.4121(36)	-1.3490(11)
b	0[b]	0[b]	±1.2003(13)	0[c]
c	0.053(28)	0.063(24)	-0.167(9)	0.204(7)

[a] Kraitchman analysis only provides absolute values of the coordinates. Signs are inferred based on the the *ab initio* calculations and the type of selection rules observed.
[b] Small number as the Si atom is on the *a*-axis. The Costain error is larger than the coordinate.
[c] Small imaginary number as the β-C atom lies on the *a*-axis.

Table 7.10: Effective ground state (r_0) and substitution (r_s) structural parameters of silacyclobutane.

	r_e[a]	ED[b]	r_s (this work)	r_0[c] (this work)
R(Si-$^\alpha$C) (Å)	1.893	1.885(2)	1.879(6)	**1.8848(8)**
R($^\alpha$C$^\beta$C) (Å)	1.558	1.5741(3)	1.567(5)	**1.5646(21)**
$<^\alpha$CSi$^\alpha$C (°)	78.2	77.2(9)	79.4(5)	**79.10(4)**
$<$Si$^\alpha$C$^\beta$C (°)	85.9	87.9(12)	86.4(9)	**86.28(6)**
τ_{CCSiC}				**-19.891(23)**
$<^\alpha$C$^\beta$C$^\alpha$C (°)	100.0	97.0(15)	100.0(5)	100.18(18)
θ(°)[d]	34.5	33.5(27)	30.5(36)	31.1(4)

[a] *Ab initio* values (MP2/cc-pVTZ) from Ref.[1]
[b] Electron diffraction results from Ref.[2]
[c] The parameters in bold were directly fit to reproduce the rotational constants. Other parameters were calculated from these using trigonometric relationships with their uncertainties estimated from propagation of error.
[d] Ring puckering angle as defined in Chapter 1.

between the observed and calculated rotational constants from the structural fit was better than 0.01%. Other angles in Table 7.10 were calculated from these parameters using trigonometric relationships.

The r_0 structural parameters determined in the current study are compared with the equilibrium values from *ab initio* calculations[1] and electron diffraction experiments[2] in Table 7.10. For the bond angles and lengths, results from the present microwave work match previous studies to within 3% and 0.5%, respectively. The ring puckering angle of 31.1 (4)° (the angle between the planes containing $^{\alpha}CSi^{\alpha}C$ and $^{\alpha}C^{\beta}C^{\alpha}C$) has the largest discrepancy of 7% when compared to the previous values. However, it is important to note that the electron diffraction results provide an average value over multiple energy states and this creates an interpretation challenge for such a fluxional molecule. In contrast, in this study, the ring puckering angle derived from the observed pure rotational spectra is only sensitive to the ground vibrational state. Recently, a dynamic model was applied in analyzing the electron diffraction data to account for the large amplitude motions such as ring puckering. The use of this dynamic model led to considerable changes in the estimated geometry of SCB compared to the estimates from earlier electron diffraction investigations;[14] particularly for the $^{\alpha}C$- $^{\beta}C$ bond length, which is shorter by 0.04 Å in the newer model.

The uncertainty of the ring puckering angle calculated via propagation of errors from the least squares fit (r_0 method) is only 0.4° while the Costain error is considerably larger (3.6 °) (r_s method). This reflects the fact that the Costain error is meant to reflect the effects of vibrational averaging in the ground state while the former is simply a mathematical uncertainty with no direct physical interpretation. The ring puckering angle

derived from the Kraitchman analysis (30.5(36)°) matches that obtained from the electron diffraction data (33.5(27)°) within their uncertainties. Such comparison of results from different techniques based on *ab initio*, electron diffraction and microwave studies illustrates the importance of a multifaceted methodology for verifying the structure and dynamics of flexible molecules such as SCB.

7.4.2 Determination of ground state spectroscopic constants

The observation of pure rotational transitions measured in this microwave study provided direct evidence of tunnelling in the vibrational ground state of SCB for the first time. As shown in Figure 7.4, the high resolution (~ 7 kHz) of modern microwave spectrometers was the key to resolving the tunnelling components of the *a*-type pure rotational transitions of SCB as this splitting is only on the order of 10-30 kHz for the transitions in the spectral range of this investigation. In fact, the 0^+ and 0^- states are so close in energy that their spectroscopic constants are essentially identical within 1σ uncertainties. Both *a*- and *c*-type transitions were observed in the microwave spectra and attributed to transitions occurring within the same tunnelling state ($0^+ \rightarrow 0^+$, $0^- \rightarrow 0^-$) and crossing the different tunnelling states ($0^+ \rightarrow 0^-$, $0^- \rightarrow 0^+$), respectively. This observation is consistent with the symmetry of the rotation inversion levels of the ground vibrational states of SCB as described earlier.

In addition to the pure rotational data, ground state combination differences (GSCD) calculated from the assigned rovibrational transition pairs in the far infrared spectra were used to derive ground state spectroscopic parameters. The resultant constants are compared in Table 7.11. While the rotational constants determined from the

microwave work agree with those from the far infrared study, the centrifugal distortion constants (most noticeably the K dependent ones such as Δ_{JK} and Δ_K) are somewhat inconsistent with each other. This is likely due to the fact that the microwave data set includes only 26 transitions with J (max) =3 and K_a (max) = 3, whereas the GSCDs covered rotational states up to J = 52 with K_a (max) = 40 and these high J and K_a levels are particularly sensitive to these centrifugal distortion terms.

Accurate characterization of the ground vibrational state played a very important role in the rovibrational analyses of the ν_{29} and ν_{30} bands. The preliminary assignment of the ν_{29} and ν_{30} bands was very challenging as both spectral regions are crowded with double the number of transitions due to tunnelling splittings. The spectrum was especially dense for the former where both *a*- and *c*-type rovibrational transitions are observed. Data from the high precision microwave experiment were used to confirm the leading transitions from the Loomis-Wood plots in the preliminary stages of the assignment. The GSCDs were the key to confirming the correct assignments of the strongest progressions in the congested spectra. Once the preliminary assignment was complete, the GSCDs collected throughout the remaining assignment process added higher energy level information to the data set which provided a comprehensive description of the ground state in the end. Thus, both high precision (from pure rotational measurement) and broad coverage (from GSCDs in rovibrational analyses) contributed to the characterization of the ground vibrational state of SCB in this study.

Table 7.11: Comparison of ground state spectroscopic constants of silacyclobutane determined by pure rotational and rovibrational studies.

	Microwave (this work)	Infrared (this work)
Rotational constants / cm^{-1}		
A	0.2940598 (4)	0.2940595(3)
B	0.2097782 (6)	0.2097752(6)
C	0.1416069 (6)	0.1416076(3)
Centrifugal distortion constants / 10^{-9} cm^{-1}		
Δ_J	70(5)	79.8(4)
Δ_{JK}	147(5)	208.2(14)
Δ_K	-63(5)	-117.0(17)
δ_J	10.4(6)	20.55(19)
δ_K	-45(7)	50.4(8)
ΔE_{01} / cm^{-1}	0.0025259(6)	0.00254798(7)
No. of transitions	26	1108

7.4.3 Infrared spectra of the ν_{29} band

Although the ν_{29} mode was predicted to have rovibrational transitions with c-type selection rules based on B_1 symmetry, both a- and c-type transitions were observed and assigned for this band. The appearance of both types of rotational structures can be rationalized by symmetry considerations from molecular symmetry group theory. Figure 7.11 lists all four vibration-inversion states involved in the ν_{29} band labelled with the symmetries of their rotation-vibration-inversion energy levels. These include the two ring inversion tunnelling states of the ground vibrational state (0^+ and 0^-) and two analogous components of the ν_{29} state (ν_{29}^+ and ν_{29}^-) with their rotational sublevels (labelled with K_aK_c even/odd). By symmetry, allowed transitions are those such that the product of the

symmetries of the wavefuction ($\Gamma_{rot} \times \Gamma_{vib} \times \Gamma_{inv}$) for each state must contain the totally symmetric (A_1) representation when combined with the symmetry of the space-fixed molecular dipole moment (A_2). This means that transitions occur between levels of A_1 and A_2 symmetry or B_1 and B_2 symmetry in Figure 7.11. Examination of the symmetry of the levels shows that there are four sets of allowed transitions: two sets of c-type transitions ($0^+ \rightarrow v_{29}^+$, $0^- \rightarrow v_{29}^-$) (connecting states of the same inversion symmetry) and two sets of a-type transitions ($0^- \rightarrow v_{29}^+$, $0^+ \rightarrow v_{29}^-$) (connecting states of opposite inversion symmetry). The assignment of the cross-state ($+ \rightarrow -$, $- \rightarrow +$) a-type transitions allowed the unambiguous assignment of the inversion state labels which allowed the determination of the relative energies between the 0^+ and 0^- as well as the v_{29}^+ and v_{29}^- states.

All 6477 assigned transitions were fit using the labels described above and a simultaneous four-state fit was generated with a rms error of only 0.000119 cm^{-1}. The band origins of the v_{29} vibration (v_{29}^+ = 410.03760177(14) cm^{-1} and v_{29}^- = 410.20889633(7) cm^{-1}) were determined accurately for the first time and are consistent with recent low resolution results.[1] When compared with the DFT calculations (B3LYP/cc-pVTZ) of Laane and co-workers (409 cm^{-1}),[1] the observed vibrational band centers fall within 1 cm^{-1}. The energy difference between the two ground state levels $\Delta E_{v=0}$ from the analysis of this tunnelling split band (0.00254798 (7) cm^{-1}) was found to be consistent with that determined via our microwave study (0.00252590 (6)). The energy gap between the v_{29}^+ and v_{29}^- states was calculated as 0.173843(13) cm^{-1} for the first time and demonstrates that even the excited SiH$_2$ rocking vibrational state is split due to ring inversion tunnelling. The energy diagram of the ground state and the v_{29} state is

Figure 7.11: A schematic of transitions observed in the spectra of the v_{29} band of silacyclobutane. Rotational levels of each vibrational state are labelled to reflect rotation-inversion-vibration symmetry. Solid and dashed lines indicate the allowed c-type and a-type transitions, respectively. e (o) indicates even (odd) of K_a or K_c value.
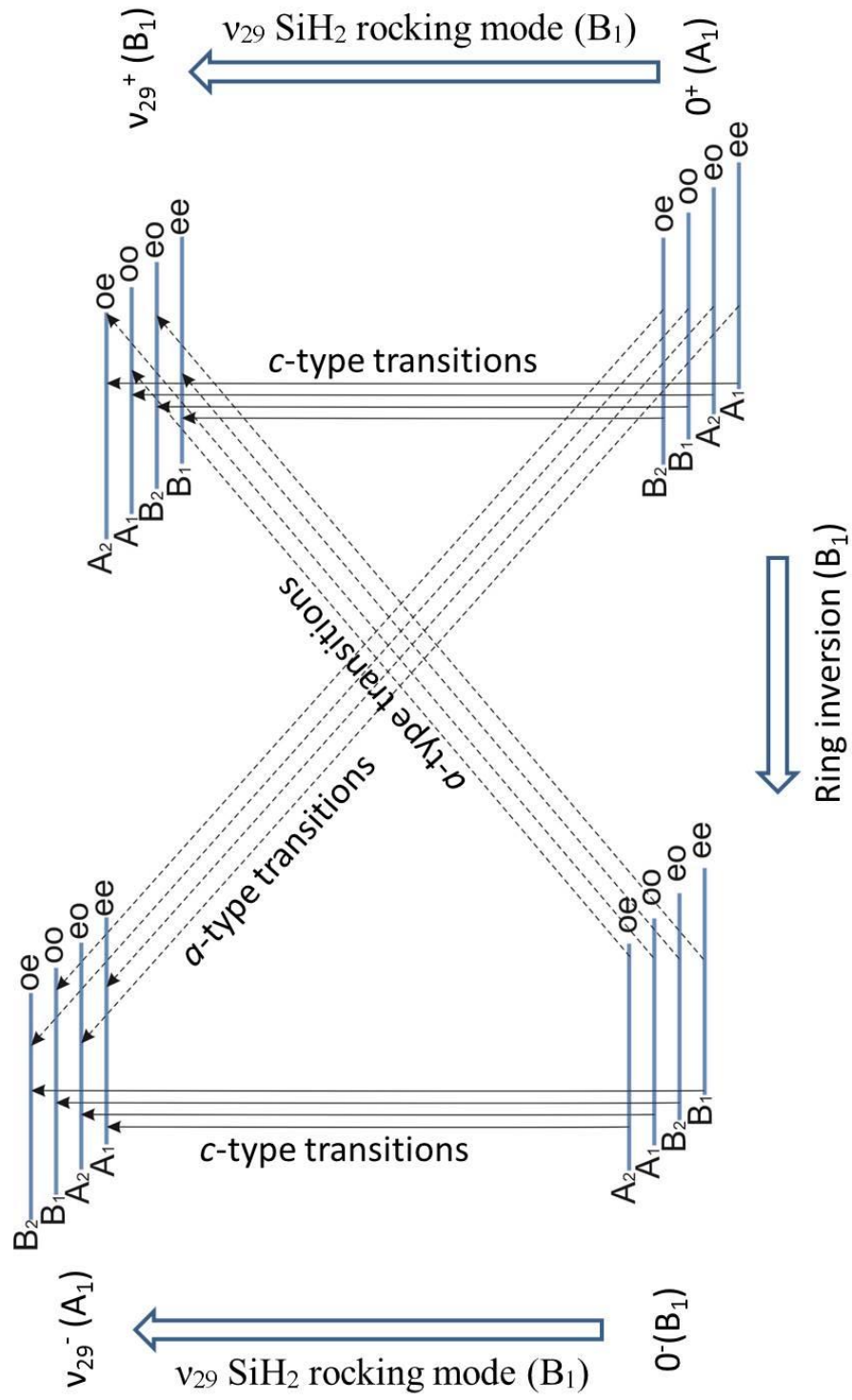
illustrated in Figure 7.12. The combination of the assignment of high J, K_c (typically from *a*-type bands) and high K_a transitions (typically from *c*-type bands) yielded a set of highly accurate spectroscopic constants, particularly the centrifugal distortion constants (shown in Table 7.8, up to 10 significant figures for rotational constants and up to 7 significant figures for centrifugal distortion constants). Together, these provide a detailed description of the excited SiH_2 rocking vibrational state.

7.4.4 Infrared spectra of the ν_{30} band

Based on the symmetry discussion above, the ν_{30} ring puckering mode also has B_1 symmetry and is therefore expected to have both *a*- and *c*-type transitions through the same molecular symmetry group theory considerations. In the far infrared spectra collected in this work, only *c*-type rovibrational transitions were found and this is likely a result of the low intensity of this band (6% that of the neighbouring ν_{29} band). In fact, the low intensities prevented extensive assignment of this *c*-type band and limited the inclusion of the lower K_a lines. As a result, the determined spectroscopic constants in Table 7.8 are less well-determined when compared to those of the ν_{29} band. The band centers of the ring puckering mode for both tunnelling states ($\nu_{30}^+ = 158.1218438(2)$ cm^{-1} and $\nu_{30}^- = 158.38466115(11)$ cm^{-1}) were accurately determined for the first time in this study. These compare well with the early low resolution infrared study (157.8 cm^{-1}) by Laane *et.al.*[3], in which the bands were not resolved. The experimental results differ by more than 10 cm^{-1} when compared to the calculated frequencies of the ring puckering mode at the B3LYP/cc-pVTZ level in Ref. [1] (147 cm^{-1} when using C_s symmetry), which are said to be accurate for predicting other vibrational modes of SCB. This study

Figure 7.12: An energy diagram illustrating relative energy levels of vibrational states in the ground state, ν_{29} and ν_{30} states of silacyclobutane in cm^{-1}. Note that the energy levels are drawn not to scale.
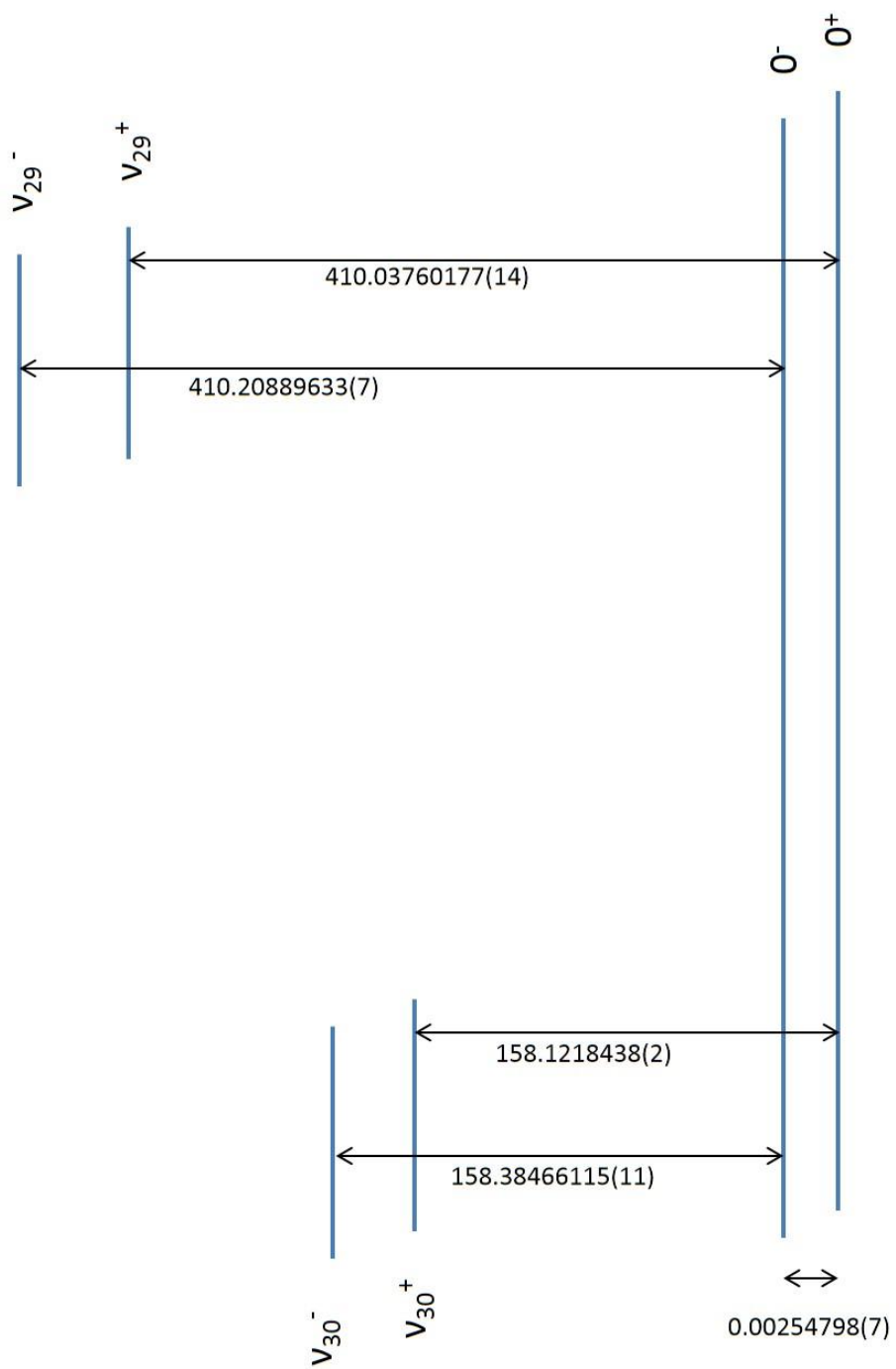
also computed the energy barrier to planarity in SCB using several methods/basis sets and the results range from 113-786 cm^{-1} with the experimental value being 448 cm^{-1}. This suggests that their relatively close estimate of the ring puckering frequency may be coincidental. Furthermore, Laane and coworkers calculated these vibrational frequencies based on a geometry optimization of a planar SCB ring (C$_{2v}$) in an effort to correlate these modes with those predicted for the puckered structure (C$_s$) to aid in the assignment of the spectrum at low resolution. It should pointed out that the molecular symmetry group C$_{2v}$ is necessary to account for the ring inversion tunnelling that interchanges the puckered SCB molecule between its two equivalent equilibrium structures but the planar C$_{2v}$ structure does not correspond to a minimum but a saddle point on the potential energy surface. This is evident from the fact that the calculated ring puckering mode frequency based on the C$_{2v}$ symmetry is an imaginary number in Ref. [1]. Additionally, predictions of other higher frequency modes became worse when the planar structure was forced. This underlines the challenge of modelling low frequency modes of fluxional molecules and in particular, the importance of using appropriate symmetry groups for different purposes in the analysis.

When comparing the resultant spectroscopic parameters of state ν_{30}^+ and ν_{30}^- with Pringle's microwave work,[5] where the direct observation of pure rotational transitions in the vibrationally excited states was made at room temperature, the upper state energy difference $\Delta E_{v=1,\nu_{30}}$ (0.26536 (2) cm^{-1}) differed by about 2% from that determined in this work (0.2599 (2) cm^{-1}). Pringle attempted to calculate the $\Delta E_{v=1,\nu_{30}}$ value by least squares fitting of far infrared[3] and microwave data to a quartic one-dimensional ring puckering potential function[3] and there was inconsistency with experimental results at that time. In

order to obtain a better prediction of the energy difference between the two inversion states of the excited ring puckering vibrational level, a modified potential function which includes a Gaussian term was proposed by Pringle to decrease the least squares error. Although this modified $\Delta E_{v=1,v_{30}}$ value was not consistent with the experimental microwave data in Ref. [5], it is almost identical to the value determined in the present high resolution for infrared study. Neither this study nor the prior microwave work in Ref. [5] successfully observed transitions that cross tunneling states (between v_{30}^+ and v_{30}^-), which would improve the determination of $\Delta E_{v=1,v_{30}}$.

7.5 Summary

This chapter reports the first high resolution microwave and infrared spectroscopic investigation of silacyclobutane. The pure rotational measurements provided direct evidence of the splitting of the ground vibrational state due to ring inversion tunnelling. Based on the rotational constants determined for the four isotopically substituted species, an accurate set of structural parameters of SCB was derived. The rotationally resolved vibrational spectra of the v_{30} ring puckering mode contained two separate sets of c-type transitions connecting states with the same inversion symmetry. In the analysis of the v_{29} SiH$_2$ rocking mode, a-type spectra crossing states of different inversion symmetry were also observed in addition to the c-type transitions within the states of common inversion symmetry.

The research presented in this chapter demonstrated the use of high resolution spectroscopy to characterize quantum mechanical tunnelling dynamics in a fluxional molecule. The availability of high resolution FTMW and FTIR spectroscopies allowed

the complex spectrum arising from SCB's unique potential energy profile to be observed and described with unprecedented detail. Through analysis of the extremely spectrally congested spectrum, new assignment protocols were developed. The accurately determined spectroscopic constants describe a broad range of rotational and rovibrational energy levels and provided a rare opportunity to probe a substantial portion of the potential energy landscape of this highly non-rigid molecule.

References

[1] A. A. Al-Saadi and J. Laane, *J. Organometallics*. 27 (2008) 3435-3443.

[2] V. P. Novikov, M. Dakkouri and L. V. Vilkov, *J. Mol. Struct*. 800 (2006) 146-153.

[3] J. Laane and R. C. Lord, *J. Chem. Phys.* 48 (1968) 1508-1513.

[4] J. Laane, *J. Spectrochim. Acta*. 26A (1970) 517-540.

[5] W. C. Pringle, *J .Chem. Phys*. 54 (1971) 4979-4988.

[6] J. Laane, *J. Am. Chem. Soc*. 89 (1967) 1144-1147.

[7] L. S. Rothman, I. E. Gordon, A. Barbe, D. Chris Benner, P. F. Bernath, M. Birk, V. Boudon, L. R. Brown, A. Campargue, J. -P. Champion, K. Chance, L. H. Coudert, V. Danaj, V. M. Devi, S. Fally, J. -M. Flaud, R. R. Gamache, A. Goldmanm, D. Jacquemart, I. Kleiner, N. Lacome, W. J. Lafferty, J. -Y. Mandin, S. T. Massie, S. N. Mikhailenko, C. E. Miller, N. Moazzen-Ahmadi, O. V. Naumenko, A. V. Nikitin, J. Orphal, V. I. Perevalov, A. Perrin, A. Predoi-Cross, C. P. Rinsland, M. Rotger, M. Šimečková, M. A. H. Smith, K. Sung, S. A. Tashkun, J. Tennyson, R. A. Toth, A. C. Vandaele and J. Vander Auwera, *J. Quant. Spectrosc. Radiat. Transfer*. 110 (2009) 533-572.

[8] H. M. Pickett, *J. Mol. Spectrosc*. 148 (1991) 371-337.

[9] Neese, C. F. Loomis-Wood Add-In (LWA) for Igor Pro, Version 2.0; 56th Ohio State University International Symposium on Molecular Spectroscopy, Columbus, OH,June,20−24,2005,http://fermi.uchicago.edu/freeware/LoomisWood.shtml.

[10] IGOR Pro Manual, WaveMetric Inc., Lake Oswego, OR USA (2008)

[11] J. Kraitchman, *J. Am. J. Phys.* 21 (1953) 17-24.

[12] Z. Kisiel, PROSPE-Programs for Rotational SPEctroscopy <http://info.ifpan.edu.pl/~kisiel/prospe.htm>.

[13] C. C. Costain, *Trans. Am. Crystallogr. Assoc.* 2 (1966) 157-164.

[14] V. S. Mastryukov, O. V. Dorofeeva, L. V. Vilkov, B. Cyvin and S. Cyvin. *Zh. Struckt. Khim.* 16 (1975) 438-440.

Chapter 8: Conclusions and future work

In the work presented in this thesis, the rotationally-resolved spectra of low frequency vibrational modes and pure rotational spectra in the ground vibrational states of prototypical four-membered heterocycles were recorded using synchrotron based Fourier transform infrared spectroscopy (FTIR) and Fourier transform microwave spectroscopy (FTMW), respectively. In general, spectral features that can only be observed with high resolution were analyzed using quantum mechanical models. The resultant sets of spectroscopic parameters derived from a vast number of assigned transitions provided accurate descriptions of rotation-vibration (and in some instances inversion) energy levels of each molecule investigated. This allowed the characterization of their respective potential energy functions at a much more detailed level compared to previous low resolution studies. The molecule-dependent spectroscopic signatures arising from unique potential energy surfaces were observed including Coriolis interactions, tunnelling doublings and hotbands, all of which contributed to the complexity of the spectra at high resolution.

It was realized that energy level perturbation is one of the main hindrances in the assignment of rovibrational spectra of small molecules and hence in the determination of accurate spectroscopic parameters. This was determined via analysis of the Coriolis interactions between two perpendicular C=O deformations that were observed in β-propiolactone and 3-oxetanone in Chapters 4 and 5. The number of affected transitions in these two molecules was found to be related to the extent of the overlapping range of

the two bands involved in the coupling. This provides future guidance in anticipating and treating potential perturbations of this type in the spectral analyses of other molecules. The determination of the Coriolis interaction parameters also allowed the determination of precise, physically meaningful values of other constants such as the rotational and centrifugal distortion constants, all of which are essential to construct potential energy profiles that characterize the vibrational motions.

It was shown that rotational resolution of the closely spaced fundamental and multiple hot bands corresponding to the ring puckering motion of a heterocycle, as in the case of 3-oxetanone, can be achieved. This is owing to the high quality spectra enabled by combining bright synchrotron light in the far infrared region with a FTIR instrument with high resolving power. The assignment and analysis of the dense spectrum enabled the accurate modelling of this characteristic lowest frequency vibrational mode of this four-membered heterocycle using a one-dimensional potential function in the form of V = $a\text{x}^4 + b\text{x}^2$ which reflects the internal dynamics along the ring puckering coordinate. In this case, the high resolution of the technique was the key to the precise determination of this quartic function as the constants a and b are susceptible to errors in the vibrational band centers in the ring puckering manifold.

The pure rotational and rovibrational spectra of the prototypical non-rigid molecules, azetidine and silacyclobutane, revealed distinctive spectral features as a result of particularly complex potential energy functions in the region of their equilibrium geometries. For example, the presence of both *rotation-vibration-inversion* and *rotation-vibration* transitions in some low frequency vibrational bands of azetidine indicates that these modes, rather than being defined by simple localized motions such as C-H

stretching, CH₂ bending, etc. that are described by normal coordinate analysis, are instead coupled with large amplitude motions such as –NH inversion. These coupled motions involve the movement of multiple nuclei simultaneously over greater distances. Both infrared and microwave spectra of silacyclobutane exhibited tunnelling-doubled transitions due to the presence of ring inversion as a result of the double-well potential energy function along the ring puckering coordinate. Chapters 6 and 7 detailed the treatment of these highly dynamic spectral signatures and showed how useful information can be derived to improve our understanding of the energy landscape of such highly non-rigid molecules. This study highlights the importance of using molecular symmetry groups to describe fluxional molecules as the spectral selection rules must account for transitions that cross tunnelling states.

For the prototypical rings studied, the experimentally determined band origins were compared with *ab initio* and Density Functional Theory (DFT) results to gauge the validity of calculations in providing accurate estimates of the infrared spectra of small molecules. In general, these comparisons indicated that the modelling of low frequency modes, in particular, is still challenging and there appears to be no systematically reliable computational method that is widely available. In some instances, unambiguous assignment of bands was only possible using selection rules of identified rovibrational transitions. This is of particular concern as the low energy dynamics of molecules are particularly important in comparison to other modes as they contribute to room temperature properties of these compounds.

Although not trivial to implement, the schemes developed during the assignment of the various congested and sometimes perturbed spectra in this work were essential for

extracting accurate information about the lowest energy states and underlying potential energy functions of these prototype rings. Successful understanding of these spectral nuances may allow such analyses to become more routine in the future. For example, recently there have been efforts to implement automated spectral assignment methods to rotationally-resolved spectra.[1,2] A so-called Genetic Algorithm (GA) has successfully been used to analyze the rovibronic spectra of a series of aromatic molecules, however, good predictions of the rotational constants, line shapes and intensities were needed before attempting to assign the experimental data. A serious limitation so far is that only rigid rotor-type Hamiltonians depending on A, B, C have been used in such automated analyses with line widths (FWHM) of 10 cm^{-1} or more in the electronic spectrum. When applied to FTIR spectra, the algorithms have been used only to model band contours but not individual transitions.[3] As there are not many references available in the field of high resolution, far infrared spectroscopy, the identification and modelling of complex spectral features discussed in this thesis provide a starting point for development of GA codes that may allow the automated assignment of complex rovibrational spectra. This requires the addition of terms to the current GA models to account for non-rigidity and other molecule-specific features as outlined in this thesis.

Successful interpretation of the complex spectra of the rings presented in this thesis has also laid important ground work to begin studies of more complex molecules in the future. Five-membered heterocyclic compounds such as furanones, hydrofurans and their derivatives are good candidates as an extension of the current work on the four-membered analogues. Aromatic five-membered heterocycles are of particular interest due to their important role in heterocyclic chemistry, however, their reactivity is complex as it

is controlled by a combination of both the aromatic ring and hetero atom properties.[4] Molecules such as 2-hydroxyfuran (which is the less stable tautomer of 2-oxo-2,3-dihydrofuran and 2-oxo-2,5-dihydrofuran as shown in Figure 8.1) have the possibility of undergoing tautomerization which further complicates their reaction mechanisms as the stable structures of the tautomers and their relative energies must be known to adequately describe their chemistry.[5,6] High resolution rotational and rovibrational techniques are capable of resolving tautomer-specific spectroscopic signatures that can shed light on the interconversion dynamics between different tautomers at equilibrium. Fundamentally, five-membered rings have two out-of-plane coordinates as discussed in Chapter 1 due to pseudo-rotation. This will result in extra complexity in the spectra. On the other hand, the successful analysis of such features would extend the current understanding of one-dimensional potential (ring puckering) functions in four-membered rings to the next level (two-dimensional pseudo-rotation potential functions). In this regard, the effective spectral analysis schemes that were successfully applied to the ring inversion in silacyclobutane and the –NH inversion in azetidine in the current study can be used to interpret the more complex spectra of five-membered heterocycles where low frequency modes are likely to couple with the pseudo-rotation motion.
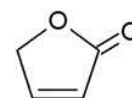
Figure 8.1: Structures of tautomers of 2-hydroxyfuran: 2-oxo-2,3-dihydrofuran and 2-oxo-2,5-dihydrofuran.
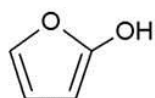
2-hydroxyfuran   2-oxo-2,3-dihydrofuran   2-oxo-2,5-dihydrofuran

The four-membered heterocycles chosen as subjects of investigation in this thesis have one thing in common: there are no free rotors (-CH_3, -NH_2, -OH, etc.) which would give rise to further complications in the spectra due to internal rotation tunnelling. However, based on the successful spectral analyses on the prototype molecules presented here, an interesting extension would be to undertake the high resolution spectroscopic investigation of molecules that involve internal rotors. These molecules are of keen astronomical interest because of their important role in atmospheric chemistry in a range of planetary systems. Theoretical models based on qualitative and quantitative characterization of these molecules show how these species may have evolved under astrophysical conditions and could reveal key information regarding how life was evolved.[7, 8] Some good candidates for these next studies are methane, ethane, and their deuterated versions. On the surface, one would consider such molecules simple and well-characterized as they have been studied for many years. The fact, however, is that their high resolution spectra are plagued by a combination of factors that have prevented the complete quantum mechanical analysis up until now. With the increased availability of ground-, aircraft- and spacecraft- based high resolution infrared instruments for space exploration now being realized (such as the Composite Infrared Spectrometer (**CIRS**) on-board NASA's **Cassini** spacecraft, the Stratospheric Observatory for Infrared Astronomy (**SOFIA**), the Texas Echelon-cross-Echelle Spectrograph (**TEXES**) and the Very Large Telescope-Cryogenic High-resolution infrared Echelle Spectrograph (**VLT-CRIRES**) located at the European Southern Observatory (**ESO**) in Chili),[9, 10, 11, 12] the molecular signals from such small molecules of interest may in fact already be present in earlier astronomical observations. The assignment of these features, however, is hindered due to the lack of complete and accurate information about the rovibrational spectra of such

simple molecules particularly in the far infrared and THz regions. Hence, a precise understanding of the spectra of these key molecules from laboratory-based studies is vital for future remote sensing purposes. The valuable schemes developed in the course of this work can be applied to such new challenges.

References

[1] J. A. Hageman, R. Wehrens, R. de Gelder, W. L. Meerts and L. M. C. Buydens, *J. Chem. Phys*. 113 (2000) 7955–7962.

[2] W. L. Meerts, M. Schmitt and G. Groenenboom, *Can. J. Chem*. 82 (2004) 804–819.

[3] W. L. Meerts and M. Schmitt, *Int. Rev. Phys. Chem*, 25(2006) 353-406.

[4] J. Alvárez-Builla and J. Barluenga, *Morden Heterocyclic Chemistry,* Wiley-VCH Verlag, Weinheim, Vol 4 (2011).

[5] J. Elguero, A. R. Katritzky and O. V. Denisko, *Adv. Heterocycl. Chem,* 76 (2000) 1-84.

[6] W. Friedrichsen, T. Traulsen, J. Elguero and A. R. Katritzky, *Adv. Heterocycl. Chem,* 76 (2000) 85-156.

[7] P. Ehrenfreund, W. Irvine, L. Becker, J. Blank, J. R. Brucato, L. Colangeli, S. Derenne, D. Despois, A. Dutrey, H. Fraaije, A. Lazcano, T. Owen, F. Robert and an International Space Science Institute ISSI-Team, *Rep. Prog. Phys,* 65 (2002) 1427-1487.

[8] P. Ehrenfreund, M. Spaansm and N. G. Holm, *Phil. Trans. R. Soc. A*, 1936 (2011) 538-554.

[9] C. A. Nixon, N. A. Teanby, C. M. Anderson and S. Vinatier, *Astrophysics and Space Science Proceedings*, Vol 35 (2013) 123-143.

[10] T. K. Greathouse , M. Richter, J. Lacy, J. Moses, G. Orton, T. Encrenaz, H.B. Hammel and D. Jaffe, *Icarus*, 214 (2011) 606-621.

[11] R. D. Gehrz, E. E. Becklin, J. de Buizer, T. Herter, L. D. Keller, A. Krabbe, P. M. Marcum, T. L. Roellig, G. H. L. Sandell, P. Temi, W. D. Vacca, E. T. Young and H.

Zinnecker, *Adv. Space Res*., 48 (2011)1004-1016.

[12] H. U. Käufl, P. Ballester, P. Biereichel, B. Delabre, R. Donaldson, R. Dorn, E. Fedrigo, G. Finger, G. Fischer, F. Franza, D. Gojak, G. Huster, Y. Jung, J.-L. Lizon, L. Mehrgan, M. Meyer, A. Moorwood, J.-F. Pirard, J. Paufique, E. Pozna, R. Siebenmorgen, A. Silber, J. Stegmeier and S. Wegerer, *SPIE*, 5492 (2004) 1218 .